공학박사학위논문

Engineering of cellular behaviors with multiscale surface patterns

멀티스케일 표면 패턴을 이용한 세포의 거동 조절

2014 년 2 월

서울대학교 대학원

기계항공공학부

김 홍 남

Engineering of cellular behaviors with multiscale surface patterns

멀티스케일 표면 패턴을 이용한 세포의 거동 조절

지도교수 전 누 리

이 논문을 공학박사 학위논문으로 제출함
2014 년 2 월

서울대학교 대학원
기계항공공학부
김 홍 남

김홍남의 공학박사 학위논문을 인준함
2014 년 2 월

위 원 장 : _____ (인)

부위원장 : _____ (인)

위 원 : _____ (인)

위 원 : _____ (인)

위 원 : _____ (인)

Abstract

In this thesis, we study the effect of multiscale topographies with various density, size, spring constant, and slanted angle on the cellular behaviors. For this purpose, the multiscale polymeric patterns were fabricated by UV-assisted capillary force lithography (CFL) technique. Through the coating with extracellular matrix (ECM) proteins such as fibronectin and collagen, the multiscale topography can present physically bio-mimetic microenvironment to the cells.

First, we report on the effect of synthetic extracellular matrix (ECM) scaffold in the form of uniformly-spaced nanogrooved surfaces in dermal wound healing. The rate of wound coverage was measured on various nanotopographical densities with vertical or parallel orientation using nanogrooves of 550-nm width with three different gaps of 550, 1100, and 2750 nm (spacing ratio: 1:1, 1:2 and 1:5). Guided by the nanotopographical cues in the absence of growth factors in wound healing process, the cultured NIH-3T3 cells demonstrated distinctly different migration speed, cell division, and ECM production as dictated by the topographical density and orientation, whereas the proliferation rate turned out to be nearly the same. Based on our experimental results, the nanopattern of 1:2 spacing ratio yielded the

best would healing performance in terms of migration speed, which seems similar to the natural organization of collagen fibers.

Next, we report the effect of feature size and orientation of multiscale topography on the migration of cancer cells. It is well known that tumor migration occurs *in vivo* following the basement membrane, microtracks, and lymphatic vasculature, showing predominant guidance by physical cues. Inspired by the nanoscale and microscale topographic guidance, we prepared flat, nano groove, and micro groove patterns. Furthermore, to emulate the reorganization of ECM by cancer cells and subsequent guided migration through reorganized ECM, the topographical orientation was also considered, by preparing groove, concentric, and radial patterns. When comparing the spreading of cell island, both collectively and individually migrating cells showed guided spreading in response to topographical orientation. However, the sensitivity to topography was more sensitive in the case of individually migrating cells. Microscopically, the topography not only induced polarization of intracellular elements such as f-actin and vinculin, but also modulated protein levels such as E-cadherin, ROCK2, and vinculin in response to the topographical size and orientation.

Finally, we study how sensitively cells can recognize underlying surface topography in the case of varying spring constants and varying slanted angles. To

this end, nanopost arrays (diameter of 400 nm) having various stiffness (spring constant: 9.33, 345.58, and 5585.05) were fabricated with various height (2000 and 600 nm) and mechanical properties (19.8 and 320 MPa). On the vertical nanopillars with various spring constants, NIH-3T3 cells showed bi-axial alignment following the array, but the degree of alignment was decreased as the spring constant increases, demonstrating correlation with the bending of nanopillars. Furthermore, to understand underlying mechanism of mechanosensing in the case of nanopillars, slanted nanopillars with various angles (90, 75, 60, 45 and 30˚) with same diameter (400 nm) were prepared. On the relatively vertical nanopillars (such as 90 and 75˚), cells showed bi-axial alignment, but as the leaning angle increases (such as 30 and 45˚) cells showed uni-directional alignment along to the slanted orientation. According to the signaling inhibition, the alignment on the relatively vertical pillars was affected by Rac signaling pathways. However, the effect of Rac signaling inhibition decreases as the leaning angle increases.

Key Words : Multiscale surface pattern, extracellular matrix, biomimetic, wound healing, cancer invasion, anisotropy, cell migration

Student Number: 2010-30186

Contents

List of Tables

List of Figures

Figure 4-12. Apparent cellular morphologies with respect to the slanted angle. (A) projected area, (B) perimeter, (C) major axis, (D) minor axis, (E) circularity, and (F) aspect ratio.

Nomenclature

k_{bend}	Spring constant
F	Traction force
D	Diameter
H	Height
W	Width
S	Spacing
θ	Slanted angle
E	Elastic modulus

Subscripts

x	x component
y	y component

Chapter 1. Introduction

In regenerative medicine, therapies generally focus on a specific organ to meet the heterogeneity and demands of the individual organs. Therefore, regenerative medicine has to start from the understanding of underlying cellular behaviors, tissue specific environment, and cause of tissue degradation and injury. In terms of cellular behavior, for example, cells in various tissues respond differently according to diverse factors such as physical topography or rigidity (durotaxis) [1], gradient of cellular adhesion sites (haptotaxis) [2], electric fields (electrotaxis) [3], and chemical factors (chemotaxis) [4, 5]. Importantly, different cells may behave oppositely even under identical stimuli: fibroblasts migrate towards the more rigid region while neurons stretch neurites to the direction of softer site. Furthermore, the environmental effects originated from the organ-specific functions such as protection (skin), mechanical maintenance (bone), transmission of force (ligament and tendons), conduction of electrical signal (neuron), blood circulation (heart and vessels), and force generation (skeletal muscle) have strong correlation with the multiscale structures *in vivo* (Fig. 1-1).

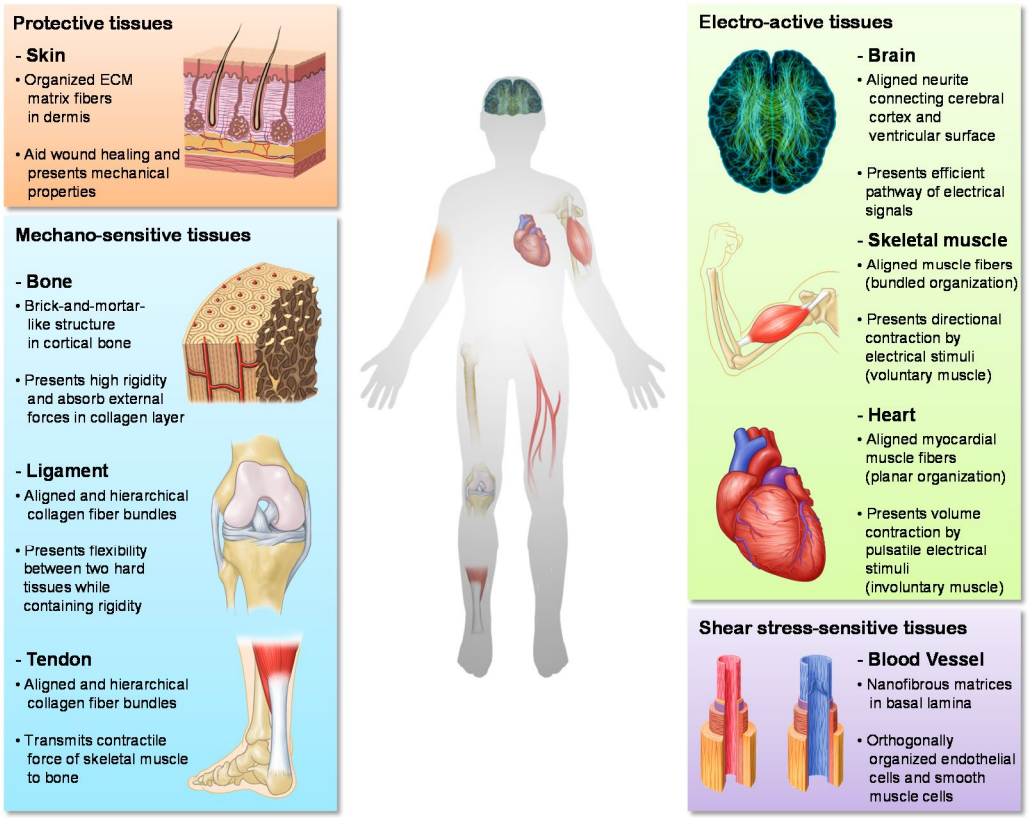

Figure 1-1. Various multiscale structures in the human body. The tissues are classified into four categories including protective, mechano-sensitive, electro-active and shear stress-sensitive tissues with respect to the tissue specific environment and functions.

Among the various factors described above, physical cues are of great importance since cells reside in a physical microenvironment with tissue specific topography and rigidity. Such physical structures are widely observed in human body such as the neuronal network in the brain, aligned myofibrils in the heart and skeletal muscle, and collagen fibers in the skin (Fig. 1-1). Since these structures are intended for the tissue specific functions, pathology may change the physical nanostructures in these organs, which results in the malfunction or disconnection of signal or force transfer. For example, it is well known that neurons in human brain have a radially spreading morphology connecting the cerebral cortex and white matter. In the case of physiological malfunctions such as Alzheimer's or Parkinson's diseases, neuronal interconnections are severely damaged, thus losing informational pathways [6]. The goals of regenerative medicine with the aid of nanostructures lies in facilitating guided cell migration and proliferation to restore physiological structures and functions and minimizing possible side effects. To fabricate the observed natural structures with distinct physical properties, various materials and fabrication methods have been used over time.

The rapid evolution of cell and tissue engineering has necessitated the use of various materials such as ceramics, metals and polymers as tissue engineering scaffolds for specific cell types. It has been widely recognized that polymers possess a number of advantages as tissue engineering scaffolds in terms of

biocompatibility, transparency, and processability. For example, ceramics (e.g., oxides and nitrides) are bioinert with high elastic modulus but their use is limited due to inherent brittleness and opaqueness. Metals also present high stiffness and resilience, but some are susceptible to corrosion. Moreover, both materials lack bioactivity and thus researchers have increasingly employed polymers as materials which can suitably reproduce the physiological extracellular matrix (ECM) environment with the added benefit of increased cell adhesion and biocompatibility.

The design and preparation of biomimetic polymer scaffold in terms of physical, chemical and biological similarity to native ECM plays a critical role in constructing optimal microenvironments for cells and tissues. For the last few decades, many characteristics of ECM microenvironments have been replicated by using various methods in terms of rigidity [7] [8], chemical concentration [9], shear stress [10], and micro/nanotopography [11, 12]. Among these characteristics, the rigidity and topography of biomaterials has been of major interest for mechanotransduction of cell responses [13, 14].

The physical geometry of substrates and its importance in the biomedical science has long been of interest to researchers [15, 16]. Since surface patterns can mediate development of focal adhesion complex and subsequent signaling pathways, controlled multiscale topography can modulate various cell behaviors

such as migration, proliferation and differentiation [17, 18]. One of the notable demonstrations was reported by Dalby et al., showing controlled osteogenic differentiation of mesenchymal stem cells (MSC) with disorderedness of nanopit arrays. In this work, the differentiation of stem cells were sophisticatedly controlled by the slight misalignment (~25 nm), showing maximum differentiation in the disordered nanotopography, not in the ordered arrays [19]. Another example reported by Levchenko et al. have demonstrated that the nanogrooves (width: 150 nm, spacing 50 nm, and height: 200 nm) not only induce the alignment of neonatal rat ventricular myocardial cells, but also induced anisotropic mechanical contraction and action potential propagation [20]. These seminal works, together with a series of following studies, reveals that topography could be a key factor in controlling various responses of cells.

Despite the potential of the findings, the materials used in the cell engineering studies were too soft to emulate the full spectrum of material rigidity found in the human tissue. Furthermore, the integration of micro- and nanostructures for tissue engineering scaffolds has been a challenge due to poor processability of the polymer materials, limiting the widespread fabrication of well-organized *in vivo* like structures for tendons, ligaments, collagen fibers in brain and muscle fibers [21]. Thus, the requirements for high resolution patterning have been continuously arisen for last decades. In this thesis, to overcome such limitation induced by mechanical properties and processability, we utilized UV

curable polyurethane (PU)-based polymers, which enables reproducible and rapid patterning.

In *Chapter 2*, we report on the effect of synthetic extracellular matrix (ECM) scaffold in the form of uniformly-spaced nanogrooved surfaces in dermal wound healing. The rate of wound coverage was measured on various nanotopographical densities with vertical or parallel orientation using nanogrooves of 550-nm width with three different gaps of 550, 1100, and 2750 nm (spacing ratio: 1:1, 1:2 and 1:5). Guided by the nanotopographical cues in the absence of growth factors in wound healing process, the cultured NIH-3T3 cells demonstrated distinctly different migration speed, cell division, and ECM production as dictated by the topographical density and orientation, whereas the proliferation rate turned out to be nearly the same. Based on our experimental results, the nanopattern of 1:2 spacing ratio yielded the best would healing performance in terms of migration speed, which seems similar to the natural organization of collagen fibers.

In *Chapter 3*, we report the effect of feature size and orientation of multiscale topography on the migratory behaviors of cancer cells. It is well known that tumor invasion occurs *in vivo* following the physical guidance such as

basement membrane, microtracks, and lymphatic vasculature. Inspired by the nanoscale and microscale topographic guidance, we prepared flat, nano groove, and micro groove patterns. Furthermore, to emulate the reorganization of ECM by cancer cells, the topographical orientation was also considered, by preparing groove, concentric, and radial patterns. When comparing the spreading of cell island, both collectively and individually migrating cells showed guided spreading in response to topographical orientation. However, the sensitivity to topography was more sensitive in the case of individually migrating cells, due to the limited cell-cell interactions. Microscopically, the topography not only induced polarization of intracellular elements such as f-actin and vinculin, but also modulated protein levels such as E-cadherin, ROCK2, and vinculin in response to the topographical size and orientation.

In *Chapter 4*, we study how cells can sensitively recognize underlying surface topography in the case of varying spring constants and varying slanted angles. To this end, nanopost arrays (diameter of 400 nm) having various stiffness (i.e. spring constant) were fabricated by modulating height (2000 and 600 nm) and mechanical properties (19.8 and 320 MPa). On the vertical nanopillars with various spring constants, NIH-3T3 cells showed bi-axial alignment following the array, but the degree of alignment was decreased as the spring constant increases. This result showed correlation with the degree of bending of nanopillars.

Furthermore, to understand underlying mechanism of mechanosensing in the case of slanted nanopillars, slanted nanopillars with various angles (90, 75, 60, 45 and 30˚) with same diameter (400 nm) were prepared. On the relatively vertical nanopillars (such as 90 and 75˚), cells showed bi-axial alignment, but as the leaning angle increases (such as 30 and 45˚) cells showed uni-directional alignment along to the slanted orientation, demonstrating gradual transition from bi- to uni-axial alignment. According to the signaling inhibition, the initial alignment on the relatively vertical pillars was governed by Rac signaling pathways. However, the effect of Rac signaling inhibition decreases as the leaning angle increases.

Chapter 2. Effect of Orientation and Density of Nanotopography in Dermal Wound Healing

2-1. Introduction

The skin is a representative protective tissue and acts as a barrier preventing invasion of various pathogens or as a mechanical damper absorbing mechanical impact. In the multiple layers of skin, the dermis presents distinctive regenerative functions upon trauma through hemostasis, inflammation, deposition of connective tissues, neovascularization, wound contraction and scar maturation [22]. For dermal wound healing, two factors are mainly involved for the guidance of fibroblasts: growth factors and extracellular matrix (ECM). When a deep scratch such as incisional wound is generated, platelets, neutrophils and macrophages release growth factors and form a concentration gradient of growth factors around the wound site, leading to the recruitment of neighboring fibroblasts. As the fibroblasts migrate across the concentration gradient of growth factors, their migration pathways are guided by the topography of ECM which is composed of various fibers such as multiple collagens and fibronectin. Here, the recruitment of fibroblasts by the concentration gradient of growth factors is

termed ‘chemotaxis’ [4], while the guided migration following the topographical cue ‘contact guidance’ [23].

The ultimate goal of dermal wound healing is to cure the damaged skin tissue effectively without scar formation. In dermal wound healing, various growth factors participate including platelet-derived growth factors (PDGF), transforming growth factors-β (TGF-β) and basic fibroblast growth factor (bFGF) [22]. These growth factors play crucial roles in wound healing by rapidly recruiting fibroblasts to the wound site as well as stimulating the fibroblasts to secret neoconnective tissues such as collagen and fibronectin. During the wound healing, an unavoidable problem is ‘scar formation’. Except one isoform of TGF-βs (TGF-β_3), it is known that other growth factors such as PDGF, bFGF, TGF-β_1 and TGF-β_2 induce scar since they stimulate fibroblasts to excessively produce ECMs [24]. Interestingly, unlike neonatal and adult wound healing, it has been revealed that fetal wound healing has amazing characteristics of no scar formation due to the absence or very small amount of growth factors in the initial wound healing stage [25]. Inspired from such scar-free nature of fetal wound healing, Ferguson and coworkers have neutralized growth factors immunologically, demonstrating scarless dermal wound healing [24]. This work suggests that the utilization of growth factors may not be desirable in preserving the aesthetic nature of the regenerated skin tissue.

Although the immunological neutralization of growth factors may present minimized scar formation, the absence of growth factors, in turn, would retard the rate of wound healing due to delayed infiltration of the fibroblasts in the wound bed. Instead of the growth factors, the topography of ECM can also promote dermal wound healing *via* guided cell migration and proliferation at the wound site. For many decades, in an effort to engineer dermal wound dressing scaffolds, the basket weave structure of ECM toward the depth direction in dermis has particularly drawn much interest. For example, transplantation of randomly electrospun polymer matrices with embedded growth factors showed better initial wound healing in terms of vascularization and morphology of epidermis [26, 27, 28, 29]. It is noted that ECMs in dermis have unidirectionally aligned morphology when viewed parallel to the skin surface, which is called tension line [30, 31]. Due to such anisotropic nature of dermis morphology, the incision direction comes into play while presenting smaller scar formation and better healing. For example, in the case of cesarean section, the transverse incision has been preferred recently due to the inherent transverse tension line in abdomen [32, 33]. In this study, inspired from the above inherent tension line in dermis, we present the crucial role of the topographic orientation and density of synthetic ECM scaffold in dermal wound healing.

2-2. Materials and methods

2-2-1. Preparation of neonatal rat dermis

The dermis of neonatal rat skin was isolated from 1-day-old Sprague-Dawley rat (Samtako Bio Korea Co., Ltd., South Korea). The removed dermis was immersed in 1mg/ml stock of dispase/HBSS (Hanks' Balanced Salt solution) with 1% antibiotics for ~10 h at 4℃. The incubated tissue was transferred to a new Petri dish containing DPBS (Dulbecco's Phosphate Buffered Saline), and gently separated with epidermis and dermis.

2-2-2. Scanning electron microscopy (SEM)

Preparation steps of cells and tissues for SEM imaging were identical. For SEM imaging, cells or tissues were washed 3 times with DPBS and fixed with 0.1 M sodium cacodylate and 0.1 M sucrose for 30 min at 4℃. After washing with distilled water for 5 min, cells or tissues were dehydrated by serial additions of 50 %, 75 %, 90 % and 100 % ethanol solutions for 5 min each. Then cells or tissues were immersed in hexamethyl disilazane (HMDS) for 15 min at room temperature inside the hood. After drying the samples, the substrates were sputter-coated with Pt to the thickness of 3 nm prior to measurements. SEM images were

obtained using a HITACHI S-4800 microscope (Hitachi, Japan).

2-2-3. Fabrication of nanopatterned surfaces

The nanopatterned surfaces were fabricated by UV-assisted capillary lithography technique [34, 35]. Regularly-spaced nanogrooves with the width of 550 nm and three different gaps of 550, 1100, 2750 nm (spacing ratio: 1:1, 1:2 and 1:5, respectively) were replicated from the pre-fabricated silicon masters with large areas of 25 × 25 mm^2. The silicon masters had been prepared by standard photolithography and dry etching. In the replication step, a UV-curable polyurethane acrylate (PUA) precursor (Minuta Tech., South Korea) was drop-dispensed onto the master and brought into contact with a 100 μm-thick polyethylene terephthalate (PET) film (SKC Inc., South Korea) as a backing plane. After subsequent irradiation of UV for few tens of seconds, a negative PUA replica was formed on the PET film. Then the same replication process was performed onto a cleaned cover slip using the replicated PUA pattern as a mold. The flat and patterned surfaces were generated on the same cover slip in order to maintain the same experimental conditions.

2-2-4.In vitro wound model

Traditionally, wound healing techniques were performed on a flat substrate with scratch method. Since such a method might damage the nanotopography, and induce intracellular proteins, we utilized a thin polydimethyl siloxane (PDMS) slab to generate a cell-free area. Specifically, a 200 μm-thick PDMS sheet was cut into slabs with width of 500 μm and length of 20 mm using two intact sharp blades. The PDMS slabs were placed onto the patterned cover slips in parallel or vertical orientation with respect to the nanogrooves. Due to conformal sealing of the thin PDMS slab, no cells were shown to grow on the protected area.

2-2-5. Cell culture

NIH-3T3 cells (purchased from American Tissue Culture Collection) were cultured in Dulbecco's modified Eagle's medium (DMEM) (Invitrogen, USA) supplemented with 10% fetal bovine serum and 1% penicillin/streptomycin at 37°C and 5% CO_2. The patterned substrates were sterilized in UV chamber for 1 h and then coated with 5 μg/ml fibronectin (from bovine plasma) for 1 h. Cells were seeded with concentration of 7×10^5 ml^{-1}, and cultured until confluency. Then, PDMS slabs were removed manually with a sharp tweezer and cells were imaged under an inverted microscope (IX71, Olympus Inc., Japan) in the time course of 12, 24, 36 and 48 hours.

2-2-6. Immunostaining

For immunofluorescence staining, cells were washed with DPBS and fixed with 3.7% formaldehyde in PBS for 15 min at room temperature. Then cells were permeabilized in 1% BSA and 0.3% Triton X-100 in PBS for 15 min, incubated with target-specific antibodies at room temperature, and washed with PBS 3 times. Detailed information of antibodies used in this study follows: FITC anti-α-tubulin (Sigma, St Louis, MO, F1268, 1:100 dilution), f-actin (Sigma, St Louis, MO, P1951, 1:200 dilution), DAPI (Sigma, St Louis, MO, D9564, 1:5000 dilution), goat anti-human anti-fibronectin (primary: Sigma, St Louis, MO, F3648, 1:400 dilution, FITC anti-goat from rabbit: Sigma, St Louis, MO, F0382, 1:50 dilution).

2-2-7. EdU Assay

For the proliferation assay, the Click-iT® EdU Alexa Fluor® 594 Imaging Kit (Invitrogen, USA) was used following the protocols proposed by the provider. The incubation time for proliferation was fixed at 4 h.

2-2-8. Data analysis

The data presented in this study such as covered-area, migration speed, cell

spreading area, orientation and length of fibronectin and axial ratio were analyzed with ImageJ (NIH, Bethesda, MD, USA).

2-3. Results

2-3-1. *Ex-vivo* study of neonatal rat dermis

In mammalian skin, various ECM fibers exist in well-organized forms. From an anatomical aspect, the collagen fibers in dermis exhibit a basket-weave-like arrangement to the 'depth' direction. In the parallel plane to the skin surface, on the other hand, skin has anisotropic topographical lines called tension lines (also called cleavage or Langer's lines), which are naturally oriented collagen fibers. In order to verify the existence of these well-aligned fibers in the skin tissue, an *ex-vivo* study was carried out using a neonatal rat dermis tissue (see the experimental details). As shown in Figure 2-1(A-B), unidirectionally aligned collagen fibers of neonatal rat dermis are clearly shown. Guided by such inherent alignment of collagen fibers, fibroblasts in neonatal rat dermis are also aligned along the fiber orientation (Figure 2-1C).

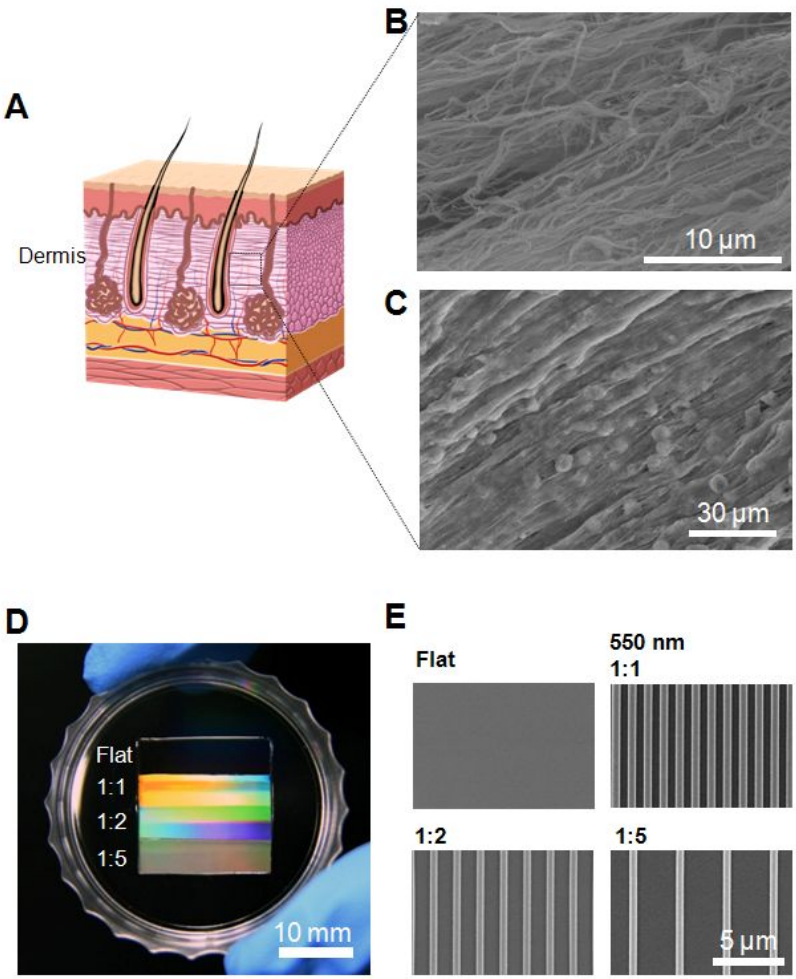

Figure 2-1. (A) A graphical illustration of dermis in skin. (B) SEM image of aligned collagen fiber bundles observed in the dermis of neonatal rat skin. The orientation of bundles agrees with the tension line in skin. (C) SEM image of aligned dermal fibroblasts in the same tissue. (D) Skin-inspired synthetic nanotopography with various densities along with flat control. (E) SEM image of various nanopatterns used in this study. The spacing ratio represents the ratio of the width to the spacing of nanogrooves.

2-3-2. Experimental design

Inspired from the presence of aligned collagen fibers in dermis, various nanogroove patterns were fabricated through UV-assisted capillary force lithography with UV-curable PUA polymer [34, 35]. To investigate the effect of nanotopographical density, 550 nm-wide nanogrooves (depth of 600 nm) with the inter-groove distances of 550, 1100 and 2750 nm (width to spacing ratio of 1:1, 1:2 and 1:5, respectively) were fabricated onto the same glass cover slip along with the flat control (no patterns on PUA surface). With this design, it was possible to evaluate the cell behaviors under the same experimental conditions. The width of nanogrooves was chosen in such a way that the dimension could be similar to that of the natural collagen fibers [36]. As shown in Figure 2-1(D-E), the fabricated nanogrooves were well-defined over large areas with distinct physical integrity.

For the model cell type, NIH-3T3 fibroblasts were used since the majority of wound healing process in dermis is governed by fibroblasts. Traditionally wound healing studies have utilized a 'scratching method,' in which the monolayer of epithelial cells or fibroblasts cultured on smooth surfaces is removed with a sharp glass pipette tip [37, 38]. However, the scratch method can cause two potential problems: destruction of the as-formed polymeric

nanotopography and damage of the cell membrane. The latter induces secretion of intracellular proteins such as Hmgb1 which act as a growth factor [39]. Thus, instead of the scratching method, a thin PDMS slab was used as a cell migration barrier to create a cell-free area [40, 41]. Figure 2-2A depicts the experimental illustration where a thin PDMS slab was placed first onto the fabricated nanopatterns prior to ECM coating and cell seeding. The orientation of PDMS slab was either vertical or parallel against the direction of nanogrooves. Then, NIH-3T3 fibroblasts were cultured until confluency. When the confluence monolayer was formed, the PDMS slab was removed, letting the cells migrate and proliferate into the empty region. The images were taken every 12 hours (0, 12, 24, 36 and 48 hours) and the occupied areas were analyzed. The optical images in Figure 2-2(B-C) show representative cell morphologies at initial and 48 h time points.

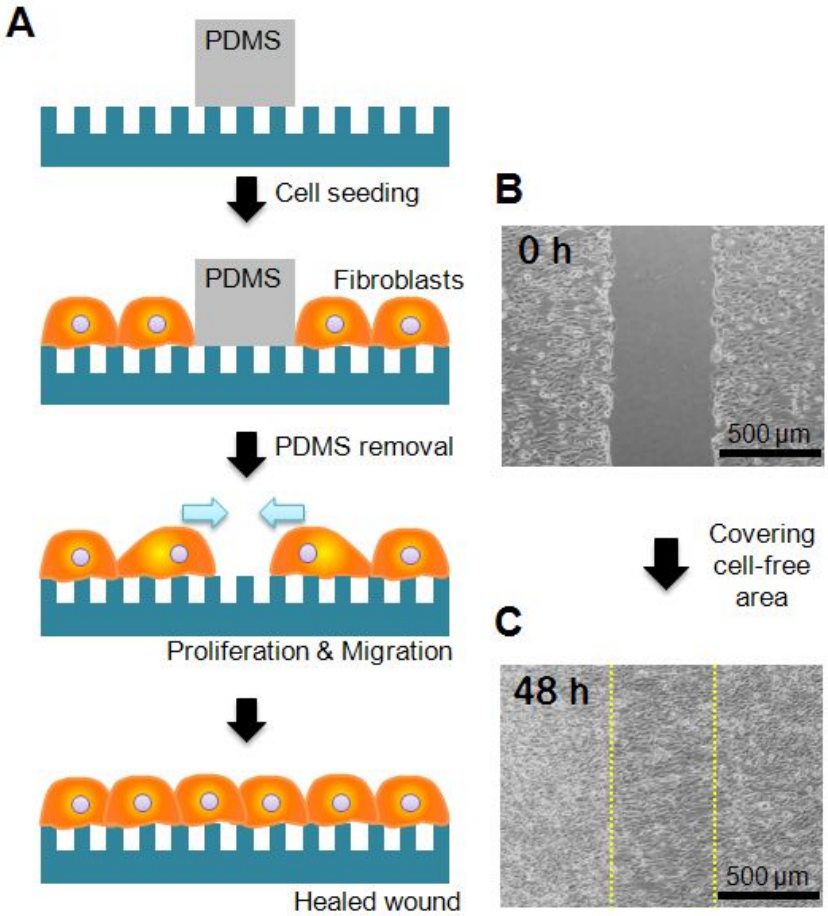

Figure 2-2. Experimental procedure of *in vitro* wound healing study with nanopatterns. (A) A thin PDMS sheet with a controlled width of 500 μm and thickness of 200 μm was placed onto the nanopatterned surface to be used as a barrier for cell migration. After ECM coating, NIH-3T3 fibroblasts were seeded and cultured until reaching confluency. The removal of PDMS sheet allows migration and proliferation of the fibroblasts to fill the cell-free area (B). The cell-free area is continuously covered by the fibroblasts with time for the two different orientations of nanogroove pattern (C).

2-3-3. Time-dependent coverage of cell-free area

In this study two geometrical factors are considered: (i) orientation and (ii) density of nanogrooves. In view of topographical orientation of natural collagen fibers, vertical, parallel and flat cases would show different wound healing behaviors in terms of the coverage rate of cell-free area. The representative SEM images of the three cases are shown in Figure 2-3(A-C) (spacing ratio of 1:1). It is well known that the cell migration is guided by the direction of nanotopography, which is called contact guidance [4, 42]. For quantitative evaluation of contact guidance, the rate of filling into the initially cell-free area was analyzed by measuring the occupied area by the fibroblasts. According to the time-lapse observation for 48 hrs shown in Figure 2-3(D-F), the vertical cases displayed much faster covering rate compared to the vertical and flat cases (Figure 2-3G). For the parallel patterns, the covering rate was even lower than that on the flat surface. The maximum covering rate was observed on the vertical 1:2 nanogroove pattern, which showed approximately 2-fold increase compared to the lowest speed on the 1:1 parallel pattern.

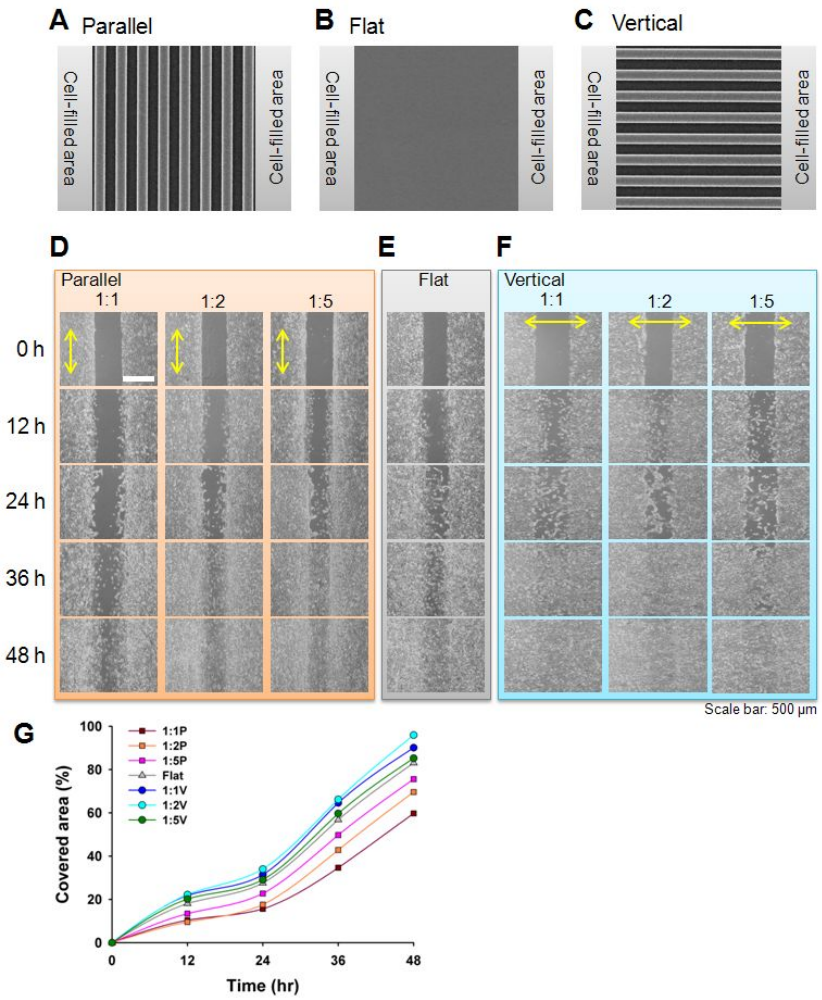

Figure 2-3. The effects of topographic orientation and pattern density in covering cell-free area. (A-C) Representative parallel and vertical patterns together with the flat control (no pattern on PUA surface). (D-F) Time-lapse microscopic images of *in vitro* wound healing with respect to the orientation and densities of nanogrooves. (G) Quantification of covered area by fibroblasts for each orientation and density. As shown, the vertical patterns demonstrated much faster covering rates compared to the flat control and parallel patterns.

2-3-4. Migration assay

In general, the wound healing is governed by two distinct cell behaviors of migration and proliferation. Since the wound repair process is orchestrated by these two in a combined fashion, it may be desirable to decouple the combined effect of migration and proliferation. In Figure 2-4A, we first analyzed the migration speed of fibroblasts with different topographical orientation. Several notable findings are derived as summarized below:

(i) The orientation of nanogrooves significantly affected the cell migration speed. In particular, the vertical orientation (noted as V with cyan color) gave rise to a much faster migration speed as compared to the parallel orientation (noted as P with orange color) and flat surface. Such difference is a direct consequence of cell polarization guided by the direction of nanopatterns, as schematically illustrated in Figure 2-4(B-D). For convenience, each migration characteristic can be termed “limited” (Figure 2-4B), “random” (Figure 2-4C) and “guided” migration (Figure 2-4D).

(ii) The density of nanopatterns also affected the cell migration speed. In the vertical cases, the cell migration pattern demonstrated a typical biphasic behavior, increasing from the 1:1 pattern (35.44 μm/hr) to the 1:2 pattern (37.77 μm/hr) and then decreasing to the 1:5 pattern (32.91 μm/hr). In contrast, the cell migration speed was monotonically decreased with the increase of spacing ratio

for the parallel patterns; the lowest speed was observed on the 1:5 pattern (0.83 μm/hr). Interestingly, the maximum migration speed on the vertical 1:2 pattern was approximately 45 times faster than the slowest on the parallel 1:5 pattern, seemingly indicating a mismatch with the findings of the covering rate (merely 2-fold difference between the fastest and the slowest covering rates). This discrepancy implies that the wound healing process may be governed not only by migration, but also by other factors such as proliferation.

These orientation- and density-dependent migration behaviors are associated with various cellular or sub-cellular activities at the interface such as cell polarization, focal adhesions, proliferation, and cell division, which are described below.

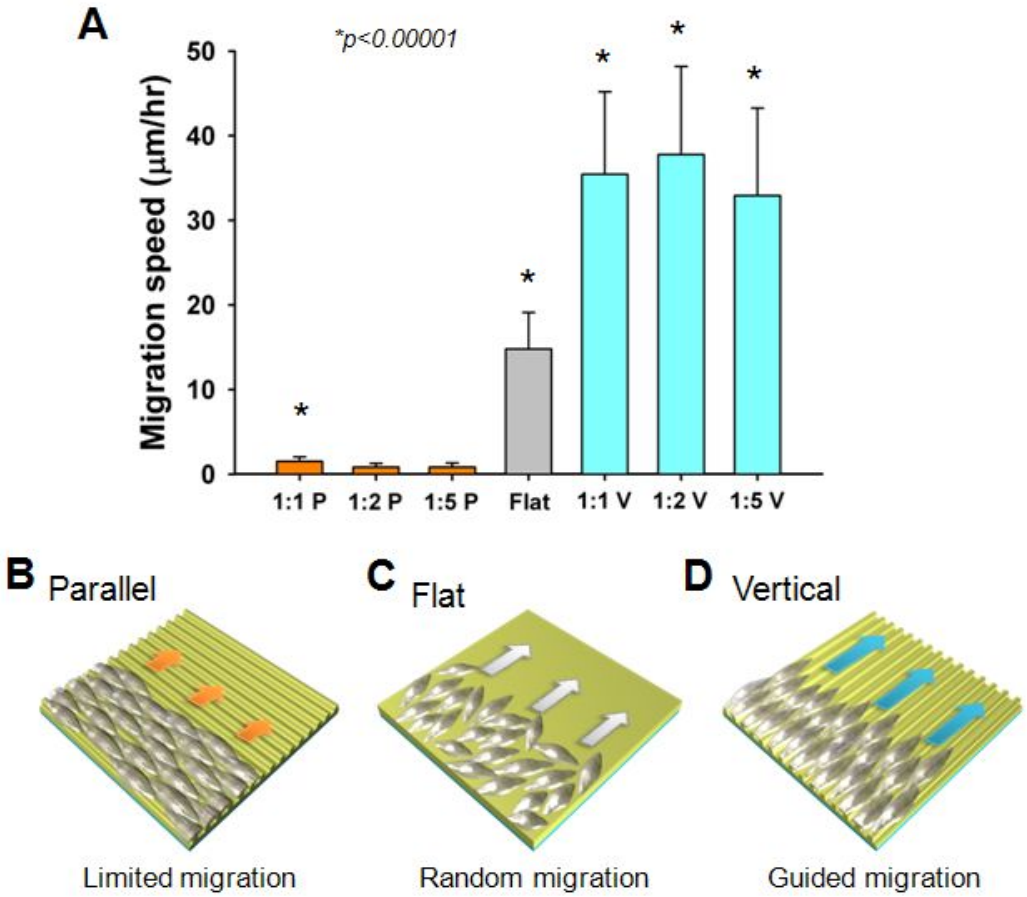

Figure 2-4. (A) Plot of migration speeds depending on the topographical orientation and density (*$p<0.0001$). (B-D) Schematics of cell migration behaviors with respect to the orientation of nanogrooves. Depending on the orientation, each cell migration may be termed "limited", "random" and "guided cell migration."

2-3-5. Analysis of focal adhesions

In cell migration, the number and polarization of focal adhesions play important roles along with penetration of cell membrane into the cavities [20]. To investigate detailed focal adhesions, the cells were immunostained for vinculin and the fluorescent images were obtained with the patterns of different orientations and topographical densities. In general, the focal adhesions were classified into two categories: dot and dash [43]. In the dash-shaped focal adhesions f-actin fibers were attached on them, and enable cell contraction through the transfer of forces. For these reasons, the orientation of focal adhesions agrees with the orientation of f-actin fibers [44].

In the vertical patterns, as shown in Figure 2-5(A-B) (24 hrs after PDMS removal), focal adhesions were polarized along the nanogroove direction, in sharp contrast to random and uniform distribution on flat substrate. In particular, focal adhesions were more polarized on the 1:2 pattern as compared to the 1:1 and 1:5 patterns. Interestingly, some un-polarized FA points were observed on the 1:1 and 1:5 patterns, which were marked with a red (1:1 pattern) and a white dotted circle (1:5 pattern), respectively. The number of focal adhesions turned out to be monotonically decreasing with the increase of spacing ratio while the flat surface showed the highest number. A notable feature with the 1:5 pattern is that the cells were deeply penetrated into the interstitial regions (see cross-sectional SEM

images in Figure 2-5D), generating additional adhesion sites and focal adhesions at the bottom of grooves (white dotted circle in Figure 2-5A). In comparison, such penetrations were hardly observed in the 1:1 and 1:2 patterns. These observations partly account for the relatively slow cell migration speeds on the 1:1 and 1:5 patterns as compared to the 1:2 pattern in two aspects. For one, the poorly-aligned actin fibers would affect the net contractile force and thus the overall cell migration speed (Figure 2-5E). For the other, too much expression of focal adhesion may retard cell migration as reported previously [45].

Unlike the vertical patterns, cells could not effectively migrate across the ridges of nanogrooves in the parallel patterns since the initial focal adhesions are polarized along the groove direction [4]. Nonetheless, the distributed focal adhesions allow for the ability to laterally migrate across the ridges. As shown in Figure 2-5A, the 1:1 pattern shows relatively uniformly distributed focal adhesions compared to the 1:2 pattern, resulting in a certain extent of lateral retarded migration (Figure 2-5E). Although the 1:5 pattern also showed similar uniform distribution of focal adhesions, the migration speed would be even lower due to some penetration into the cavities, which agrees well with the cell migration speeds shown in Figure 2-4A.

As a result of limited cell migration and continuous proliferation in the parallel patterns, a gradient in the cell spreading area was observed from the wound boundary to the center (Figure 2-6). Such a gradual increase of cell

covering area was hardly observed with the flat and the vertical patterns only except around the wound border.

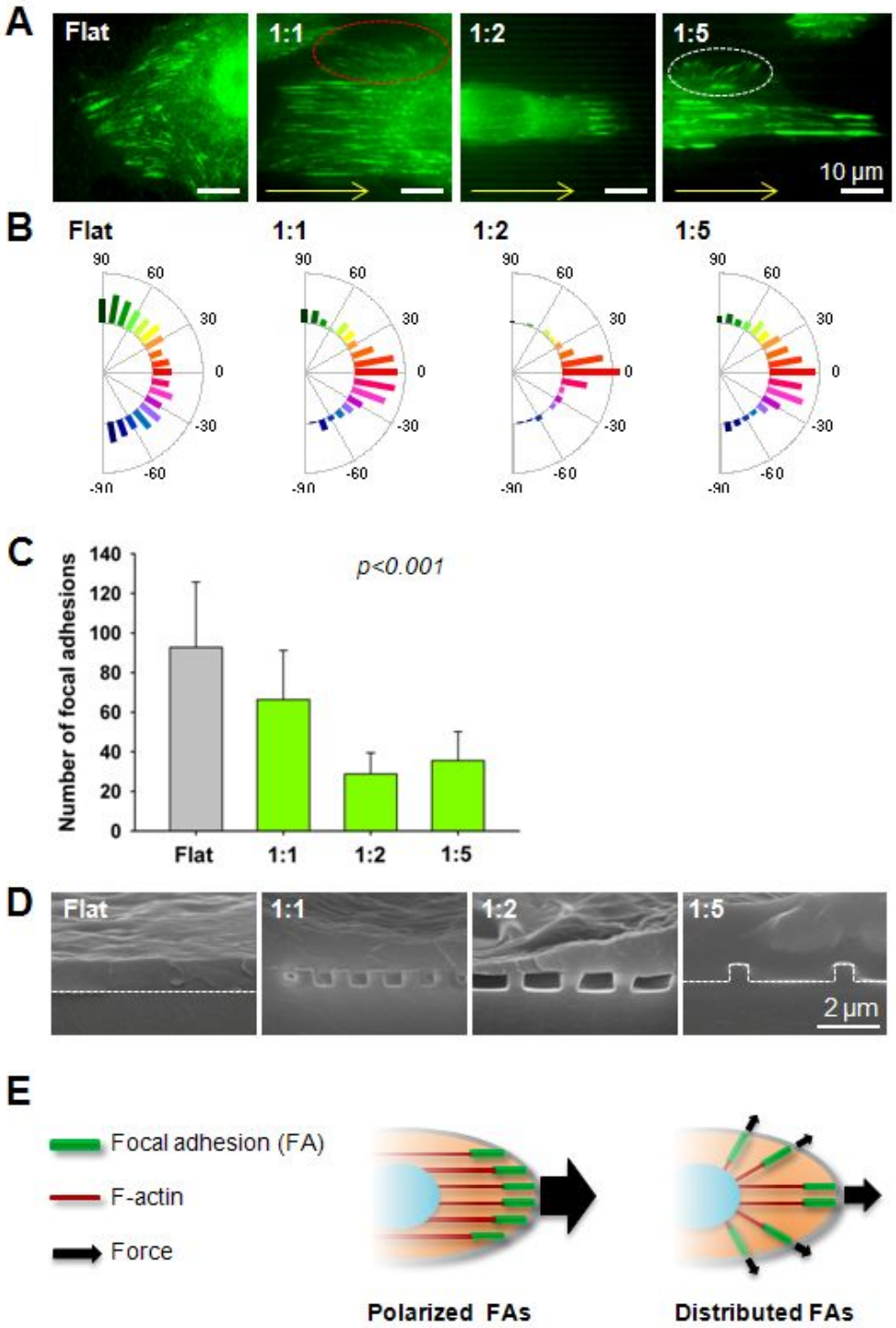
A
Flat
1:1
1:2
1:5
10 µm
B
Flat
1:1
1:2
1:5
90
60
30
0
-30
-60
-90
C
Number of focal adhesions
140
120
100
80
60
40
20
0
p<0.001
Flat
1:1
1:2
1:5
D
Flat
1:1
1:2
1:5
2 µm
E
Focal adhesion (FA)
F-actin
Force
Polarized FAs
Distributed FAs

Figure 2-5. (A-C) Analysis of focal adhesions at 24h culture. (A) Immunostaining images of focal adhesions (green: vinculin). (B) The polarization graph of focal adhesions on various nanotopographic densities. (C) The number of focal adhesions on various nanopatterns. (D) The cross-sectional SEM images of fibroblasts on various nanopatterns at 24h culture. White-dotted lines denote the surface topography of nanopatterns. (E) A proposed model for the cell migration on nanopatterns with respect to the polarization of focal adhesions.

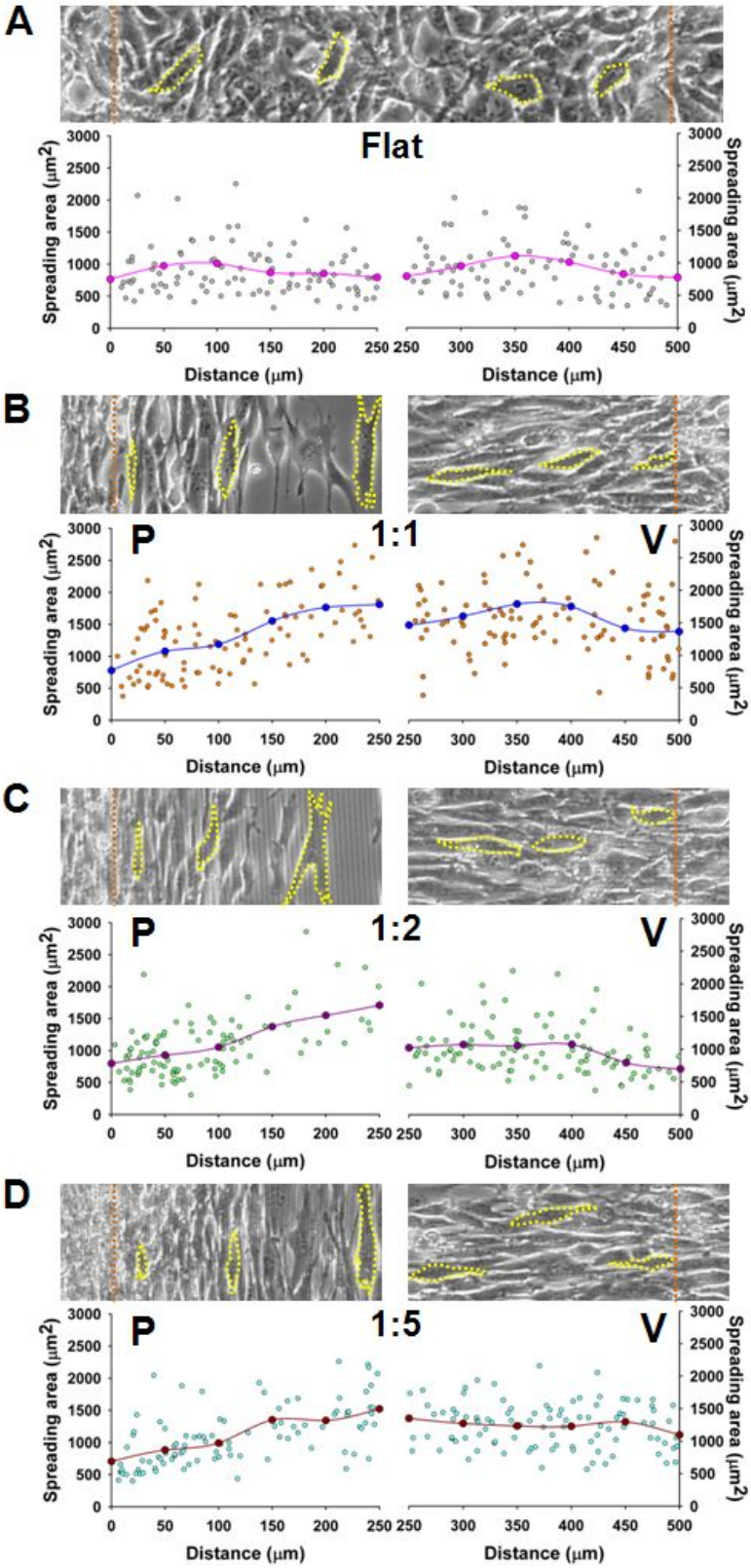
A
Flat
B
P
1:1
V
C
P
1:2
V
D
P
1:5
V
Spreading area (μm2)
Distance (μm)
0
500
1000
1500
2000
2500
3000
0
50
100
150
200
250
300
350
400
450
500

Figure 2-6. Change of the cell spreading area over the full width (500 μm) of *in vitro* wound site at 48h culture. Due to symmetry, half (0-250 or 250-500 μm) of the area were displayed for each parallel and vertical pattern. As shown the parallel cases (left column of B-D, denoted as P) show increasing trends of cell spreading area from the wound edge to wound center due to limited migration and continuous proliferation. However, such trends were hardly seen in the vertical cases only except around the wound border (right column of B-D, denoted as V).

2-3-6. Proliferation rate

Proliferation rate is also important for dermal wound healing since an increased proliferation can increase ECM production. To compare relative proliferation rate, EdU assay was employed. Since cell-cell interactions through cell-cell junctions or cell-cell communication through paracrine signaling would be effective within a distance of 300 ~ 400 μm [46, 47], the proliferation was observed up to ~300 μm from the wound edge. EdU assay in the wound edges showed no significant difference among the various patterns even in triplicates (Figure 2-7). Such topography-independent proliferation of fibroblasts was in accordance with previous studies [48].

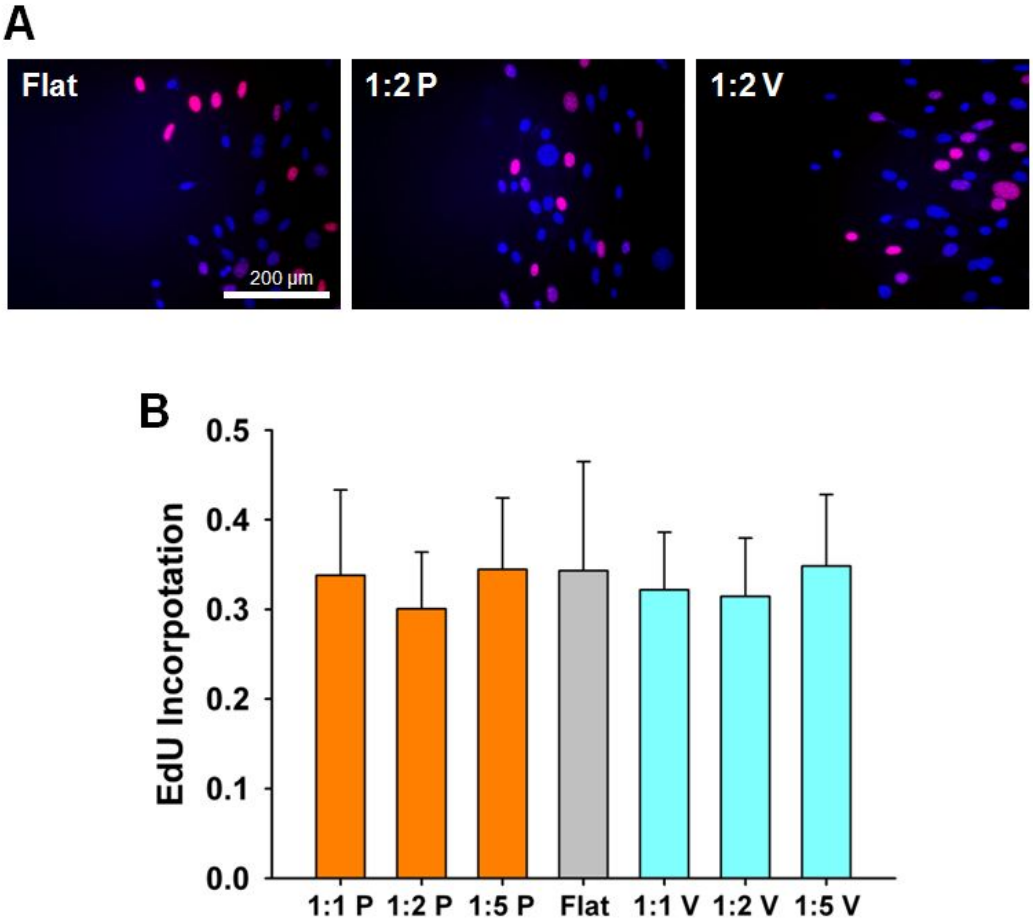

Figure 2-7. Proliferation assay on each nanotopographic orientation and density. (A) EdU analysis of fibroblasts after 4 h incubation. Only flat, 1:2 parallel and 1:2 vertical patterns were shown. (B) Quantification of EdU incorporation (EdU/nucleus ratio). No significant difference was observed even in triplicates.

2-3-7. Angle of cell division

The orientation of proliferation (i.e. cell division) needs to be assessed in filling a cell-free area (i.e., a slit-like wound) since directional cell division can promote the covering rate. In this context, the structural orientation can be a possible cue for the controlled cell division. Among the mechanisms of cell division, the division of many cell types was known to be dictated by the polarization [49, 50]. As shown in Figure 2-8A, the pattern of cell cleavage was different in three locations: (i) cell-filled area (ii) wound edge and (iii) wound area. Here, the cell division axis was determined through the immunostaining of α-tubulin. In the cell-filled area, cell division was largely governed by topographic anisotropy, following the orientation of nanogrooves, and random orientation on flat substrate. In the wound edge (the border of cell-filled area and wound zone), the flat and vertical cases showed similar cell division pattern to that of the cell-filled region. In contrast, in the wound edge of the parallel case, the cell division was not well correlated with the direction of topographical guidance (see the red dotted circle in Figure 2-8A). These cell division behaviors agree with a previous study which demonstrated the orientation of microtubule organizing center (MTOC) at the border of *in vitro* wound [51].

Since the cell division in the wound area (i.e. cell-free area) is of particular interest, we further investigated the effect of pattern orientation and

density at the wound site. In the vertical case, the cells showed aligned axis of cell division regardless of pattern density. In the parallel case, however, the cells showed some deviation from the axis of topographical guidance, especially for a large spacing pattern. For example, the maximum probability moved from 90° to 80° for the 1:5 pattern, suggesting reduced topographic anisotropy and guidance ($p<0.0001$). Although the underlying mechanism is not clear, it is believed that the increased pattern spacing allows for a more flat substrate-like environment for the cells in views of elevated penetration into the cavities (see Figure 2-5G) and randomly distributed focal adhesions (Figure 2-5D and 2-5E). It seems that the off-the-axis cell division for the parallel 1:5 pattern further assists faster coverage of cell-free area compared to the parallel 1:1 and 1:2 patterns (see Figure 2-4).

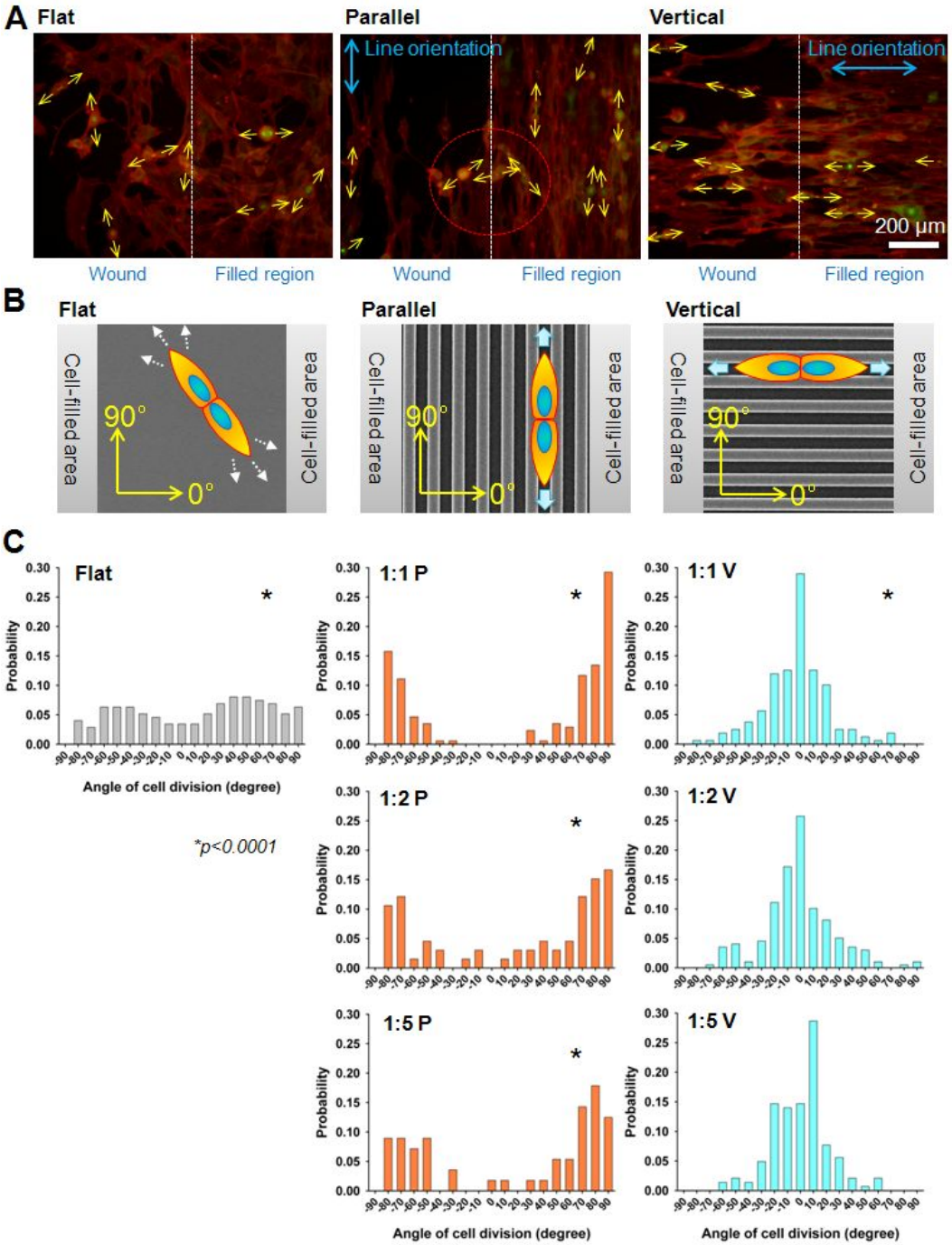
A
Flat
Parallel
Vertical
Line orientation
Line orientation
200 μm
Wound
Filled region
Wound
Filled region
Wound
Filled region
B
Flat
Parallel
Vertical
Cell-filled area
Cell-filled area
90°
0°
C
Flat
1:1 P
1:1 V
1:2 P
1:2 V
1:5 P
1:5 V
Probability
Angle of cell division (degree)
*p<0.0001

Figure 2-8. Orientation of cell division with respect to the orientation and densities of nanotopography at 24h culture. (A) Immunostaining images of α-tubulin (green) and f-actin (red). The orientation of cell division was denoted with yellow arrows in both cell-filled area and wound site. (B) Schematic illustration of cell division in wound site. (C) Graphs of cell division axis on various nanopatterns.

2-3-8. Organization of produced ECM

In dermal wound healing process, the essential role of fibroblasts is the production of new ECM proteins for the well-organized matrix similar to native dermis. In the fibroblast infiltration process, the fibroblasts secret various ECMs including fibronectin and several types of collagens. Although the majority of ECMs recovering the site is collagen type I, it was observed in a spherical form (procollagen), not a fibrous form under an *in vitro* environment due to the lack of decapping enzyme [52, 53]. For this reason, fibronectin was visualized for the ECM organization analysis.

To examine the effect of nanopattern density the angular distribution of fibronectin fiber bundles was analyzed. Similar to *in vivo*, the fibroblasts cultured on synthetic nanopatterns also showed aligned fiber orientation along the nanogrooves (Figure 2-9A). In particular, the fibroblasts cultured on nanogrooves showed relatively polarized fiber bundles than those on the flat control (Figure 2-9B). Furthermore, the alignment of bundles was also different depending on the density of nanopatterns. Interestingly the maximum probability of fibers was not observed at 0° (i.e., perfect alignment with nanogrooves). For example, on the 1:1 pattern the maximum probability was observed at ± 10 ° (1:1 pattern), ± 7.5 ° (1:2) and ± 5 ° on (1:5), respectively ($p<0.0001$).

In addition, the density of nanotopography affected the length of

fibronectin fiber bundles. As shown in Figure 2-9C, the average length of fiber bundles increased as the density decreased from 1:1 to 1:5 at the expense of large scattering of the data. Such increases of polarization and length of fiber bundles are in excellent correlation with the increase of axial ratio of the cell body (Figure 2-9D), implying that the morphology of cells (especially the shape of periphery) may be associated with the reorganization of the ECM fibers. Based on these results it can be said that the angular distribution and length of ECM fibers secreted from the fibroblasts can be guided through a synthetic nanopatterned ECM scaffold.

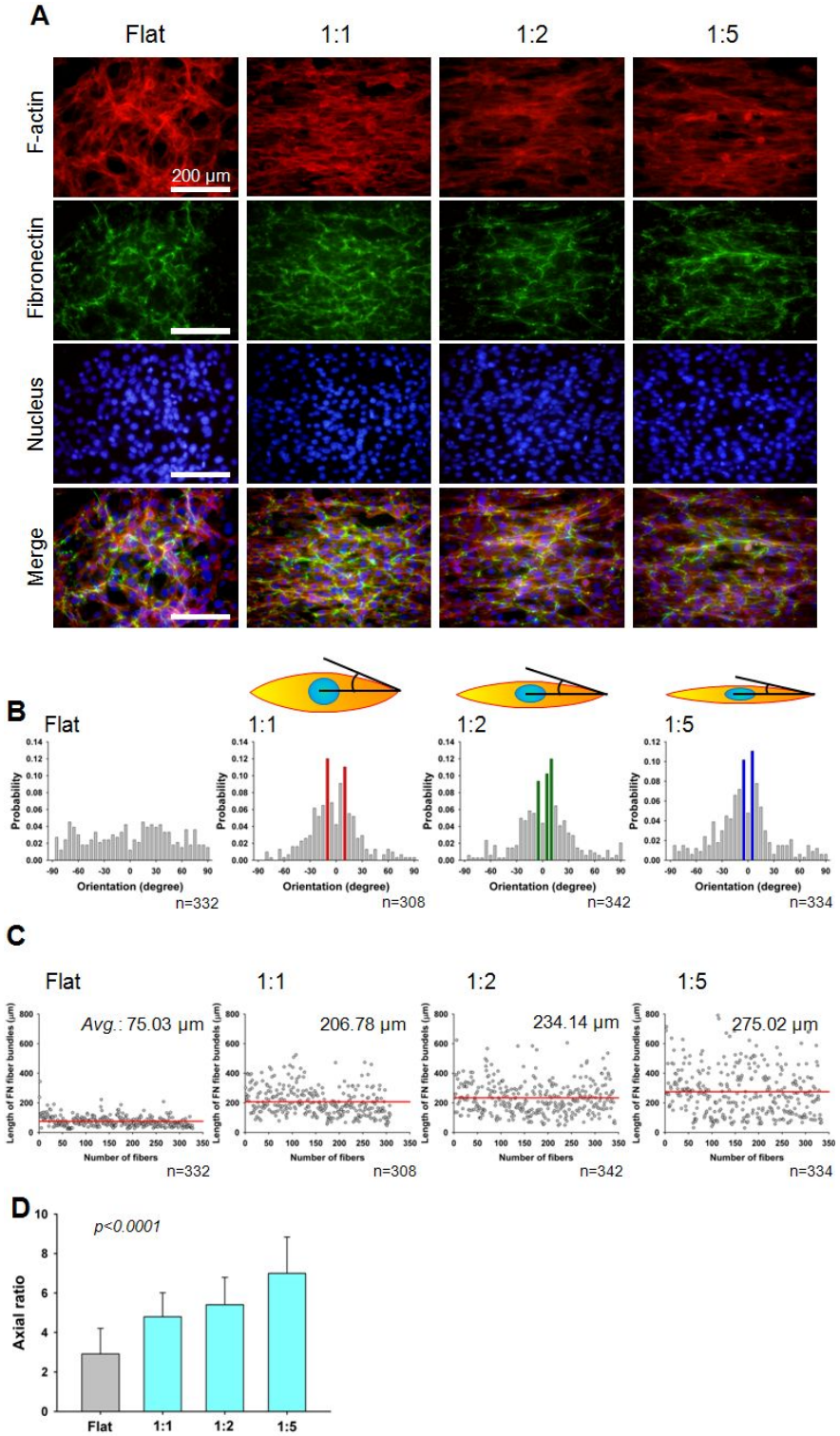
A
Flat
1:1
1:2
1:5
F-actin
200 μm
Fibronectin
Nucleus
Merge
B
Flat
1:1
1:2
1:5
Probability
Orientation (degree)
n=332
n=308
n=342
n=334
C
Flat
1:1
1:2
1:5
Avg.: 75.03 μm
206.78 μm
234.14 μm
275.02 μm
Length of FN fiber bundles (μm)
Number of fibers
n=332
n=308
n=342
n=334
D
p<0.0001
Axial ratio
Flat
1:1
1:2
1:5

Figure 2-9. Organization of produced fibronectin (FN) fibers in response to nanotopography (vertical patterns) at 48h culture. (A) Immunostaining images of fibroblasts and produced FN fibers. F-actin (red), FN (green) and nucleus (blue). (B) Orientation of FN fiber bundles. (C) Length of FN fiber bundles. (D) Axial ratio of the fibroblasts on various nanopattern densities.

4. Discussion

In this study, the topographical guidance of fibroblasts and organization of ECM in dermal wound healing were demonstrated while ruling out the effect of growth factors. The major aim of this study is to differentiate the two primary cues for the cell recruitment: concentration gradient of growth factors through the chemotaxis (*in vivo*) and topographical guidance through contact guidance (this study).

Undoubtedly, the current experimental design is deviated from the real wound healing process where the chemical and topographical cues come into play in a combined fashion. Nonetheless, the method presented here would be useful to decouple the topographical cue for potential scarless wound healing and investigate the role of various geometrical factors such as orientation and density of nanopatterns. Our work strongly confirmed the sensitivity of fibroblasts to topographical stimuli, which presents a strong evidence of utilization of topographical factor in dermal tissue engineering. In the current *in vitro* wound healing study, the proliferation rate and cell division axis showed no significant difference on different nanopatterns, thus the filling rate of cell-free area was largely governed by cell migration. In this study, two factors were chosen for the investigation of cell migration: orientation and density of nanotopography.

First, the orientation of nanogrooves was shown to significantly affect the cell migration. For the last few decades, the origin of cell migration involving fibroblasts has long been of controversy as to whether the migration is from the underlying or the nearby region [54]. Here, the orientation of synthetic matrix can give a clue for the anisotropic cell infiltration. Previous studies have pointed out that the polarization and migration of fibroblasts were more sensitive to topography rather than chemical gradients [55, 56]. By considering the relative portion of vertical and parallel fiber orientation, the effect of tension line seems larger than the weaving matrix toward the depth direction.

Second, the density of pattern may affect the fibroblast migration. According to the previous fibroblast migration studies, the fibroblasts were polarized and migrated following the topographical anisotropy [57, 58, 59, 60]. However, when comparing the effect of pattern density, there are some discrepancies on pattern scale: few micrometer scale and few hundreds of nanometer scale patterns. According to a previous study by Kim et al., the fibroblasts prefer a dense spacing ratio on microgroove patterns, showing biphasic cell migration speed [44]. Although the fibroblasts on nanoscale patterns presented here also showed a similar biphasic cell migration trend, the spreading area and focal adhesion on few hundreds of nanometer patterns would be substantially different from those for microscale topography. It is thought that the

cellular behavior may be affected by (i) the relative size ratio between cells and topography and (ii) the penetration into grooves (cells generally penetrate into valleys wider than 1~2 μm, although the critical size is different depending on the cell types). Furthermore, similar biphasic cell migration trend in both micron and submicron scale indicates that the relative spacing ratio is more important than the absolute spacing itself. Interestingly, the ECM fibers *in vivo* were organized in a bundled form with inter-bundle spacing ratio of 1:2, which agrees well with the maximum migration speed at 1:2 pattern [61].

A few remarks follow regarding the discrepancy between the covering rate of cell-free area and the migration speed. According to our experimental observations, the fastest covering rate (1:2 vertical grooves) was merely 2-fold higher than the slowest (1:5 parallel grooves), whereas the fastest migration speed 45-fold higher than the slowest on its respective pattern. This suggests that the wound healing would be predominantly governed by proliferation in the parallel patterns (proliferation-dominant) with a fraction of cells dividing in the off-axis direction or drifting away prior to adhesion onto the surface. For the vertical patterns, on the other hand, the wound healing would be dictated by cell migration along the groove direction (migration-dominant).

Finally, the organization of produced ECM fibers also is an important

factor, which has not been fully understood due to lack of suitable experimental designs. *In vivo*, fibroblasts drawn by growth factors synthesize collagen fibers in their migration path, resulting in aligned fibers from the wound edge towards the center of the wound [55]. It was observed from our study that the nanotopography itself could affect the orientation of ECM fibers as well as the length of fiber bundles. Such observation gives an implication that the secreted ECM fiber can be regulated via a suitable design of synthetic topography. It has been noted that the ECM fibers in the wound site would be gradually reorganizing even for a year. In the reorganization stage as a final wound healing step, the initial matrix organization reciprocally interact with the fibroblasts, being continuously remodeled by fibroblasts and guiding fibroblast migration [62, 63]. Thus, the initial organization significantly affects the resulting matrix since the ECM and fibroblasts interact with each other. This suggest that the utilization of synthetic topography can present guidance for the effective matrix remodeling.

2-5. Summary

Inspired from the *ex vivo* study of well-aligned collagen fibers in neonatal rat dermis, the effects of nanotopographic cue in guiding the fibroblasts migration, modulating cell division and organizing the ECM fibers were investigated. The orientation of cell polarization turned out to promote or retard the migration of fibroblasts in response to the topographical orientation. Although the effect is relatively small compared to the orientation, the density of nanopatterns also affected the migration speed and cell division axis. Furthermore, the organization of produced fibronectin fiber bundles was governed through the morphology and migration of fibroblasts cultured on nanopatterns. The results not only explain the *in vivo* cellular migration in wound healing, but also give guidance to designing an optimal wound dressing scaffold. It is hoped that the results presented here could give directions to *in vitro* wound healing study involving nanotopography.

Chapter 3. Effect of topographical size and orientation in collective and individual cancer cell migration

3-1. Introduction

Cancer cell migration to the nearby tissues is considered as a preliminary process for the metastasis [64]. In the physiological condition, cancer cells response to various cues such as stiffness of surrounding matrix, composition and texture of extracellular matrix (ECM), and chemotactic gradient generated by interstitial flow [65, 66, 67]. According to the previous studies cancer invasion is sensitively guided by the topography such as epithelial/endothelial surfaces, basement membranes, fibrillar interstitial tissues and space tracks in tissues [68, 69]. In this step, cell-cell and cell-ECM interactions as well as intracellular reorganization are occurred simultaneously, and thus resulting in various cancer cell behaviors such as overgrowth, invasion, and migration [70, 71].

Generally, this invasion process can be further classified into two cases, (i) *de novo* invasion which is occurred along with the degradation of ECM b cancer cells and subsequent migration through the neo-channels, and (ii) the migration through the already existing microtracks [68]. One notable thing is that the phenotypes of cancer cells may affect to the tumor migration dynamics. A

recent study have demonstrated that the mesenchymal type cancer cells can generate their route for migration by the degradation of nearby ECM, but the epithelial type cancer cells cannot invade into the gels by themselves due to the limited ability of ECM degradation [72]. Interestingly, when the epithelial type cells were co-cultured with fibroblast, the epithelial cancer cells could invade gels through the microtacks generated by the fibroblasts. This finding indicates that the invasion characteristics can be different depending on the cell type even under same microenvironment.

To address this cell type-dependent cancer cell migration, we study the effect of topographical size and orientation on the cell phenotype-dependent migration characteristics using mesenchymal and epithelial cancer cells. To this end, two physical factors will be considered; the topographical feature size (flat, nano groove, and micro groove) and the orientation (groove, concentric, and radial). By using multiscale topography in collaboration with stencil-induced cell patterning technique, macroscopic behaviors such as migration as well as the changes in microscopic levels such as intracellular organization and protein expression will be demonstrated.

3-2. Materials and methods

3-2-1. Fabrication of multiscale patterns

Multiscale patterns including flat, nano groove, micro groove, micro concentric and micro radial were fabricated by capillary force lithography (CFL), replicating pre-patterned silicon masters with polyurethane acrylate (PUA, Minuta Tech, Korea), and then re-replicate mold with UV-curable NOA 89 material (Norland Optical Adhesive, USA). Various silicon masters having multiscale features were fabricated by a series of MEMS machining steps such as thin film deposition, photolithography, and dry etching. For a replication of flexible mold, a small amount of PUA prepolymer (~10 μl) was drop-dispensed onto the silicon master and polyethylene terephthalate (PET) film (thickness of 50 μm, used for backing) was brought into contact. After mildly pressing with a roller several times, the liquid pre-polymer was cured by UV exposure (λ=250-400 nm) for a few tens of seconds. After UV curing, the solidified PUA attached onto PET backing was peeled off from the master, and fully cured with UV light for additional 5 hours. Then the same replication process was performed onto a cleaned cover slip using the replicated PUA pattern as a mold (NOA prepolymer is used as a processing material). The flat and patterned surfaces were fabricated on the same cover slip in order to maintain the same experimental conditions.

3-2-2. *Formation of geometrically confined cell island*

A polydimethylsiloxane (PDMS) stencil was fabricated by mixing base and curing agent with weight ratio of 10:1. After thorough mixing, the mixture was degassed, and poured on the Petri dish with a thickness of ~500 μm. After curing at 70˚C for 2 hours, a hole (diameter of 5 mm) was made by using a biopsy punch (Miltex, Germany), and cut prior to use. The stencil was attached onto the multiscale patterns after the collagen type I coating (1 μg/ml concentration, for12h) and subsequent drying.

3-2-3. Cell culture and preparation for cell migration

Human breast cancer cells (MDA-MB-231), Madin-Darby canine kidney epithelial cells (MDCK), and human glioblastoma cells (U87) were purchased from American Tissue Culture Collection (ATCC) and cultured in Dulbecco's modified Eagle's medium (DMEM, Gibco BRL, Carlsbad, CA, USA) supplemented with 10% (v/v) FBS (Gibco BRL) and 1% (v/v) penicillin/streptomycin (Gibco BRL). Human epidermoid carcinoma cells (A-431) were purchased from the Korean Cell Line Bank (KCLB) and cultured in Roswell Park Memorial Institute medium-1640 (RPMI-1640, Gibco BRL) supplemented

with 10% (v/v) FBS (Gibco BRL) and 1% (v/v) penicillin/streptomycin (Gibco BRL).The culture medium was changed every other day. The patterned substrates were sterilized in UV chamber for 1 h and then coated with 1 μg/ml collagen type I (Gibco BRL) for 12 h. Three hundred thousand cells were seeded on a pattern, and cultured until cells get confluent. Then, PDMS slabs were removed manually with a sharp tweezer and cells were imaged under an inverted microscope (IX71, Olympus, Tokyo, Japan) in the time course of 24, 48, 72, and 96 h.

3-2-4. Immunocytochemistry

Cells at 48 h were fixed with 4% (w/v) paraformaldehyde (PFA, Sigma) for 10 min. Specimens were subjected to immunofluorescent staining with anti-vinculin (Abcam, Cambridge, UK) and anti-e-cadherin (Abcam). After washing three times with PBS, the specimens were incubated with FITC-conjugated (Jackson Immuno Research Laboratories, West Grove, PA) and rhodamine-conjugated secondary antibodies (Jackson Immuno Research Laboratories) for visualizing anti-vinculin, anti-e-cadherin signals, respectively. The specimens were mounted using mounting solution containing DAPI (Vecta Laboratories, Burlingame, CA). For visualizing the actin filament, specimens were subjected to Alexa Fluor 488 phalloidin (Molecular Probes/Invitrogen, Carlsbad, CA, USA) and mounted using mounting solution containing DAPI (Vecta Laboratories, Burlingame, CA).

3-2-5. Imaging

The fluorescence images were obtained by using a FluoView FV1000 confocal laser scanning unit mounted on the IX81 inverted microscope (Olympus, Japan). Confocal images were processed with IMARIS software (Bitplane). The bright field images of cell island for 96h observation were taken by using IX71 inverted microscope (Olympus, Japan) with x4 lens in a manner of serial scanning. For the large area images, scanned images were stitched using Photoshop.

3-2-6. Western Blot Analysis

The samples were lysed using a Dounce homogenizer (Kontes,Vineland, NJ, 50 strokes, 4°C) in ice-cold lysis buffer (15 mM Tris HCl (pH 8.0), 0.25 M sucrose, 15 mM NaCl, 1.5 mM $MgCl_2$, 2.5 mM EDTA, 1 mM EGTA, 1 mM dithiothreitol, 2 mM NaPPi, 1 μg/mL pepstatin A, 2.5 μg/mL aprotinin, 5 μg/mL leupeptin, 0.5 mM phenylmethylsulfonyl fluoride, 0.125 mM Na_3VO_4, 25 mM NaF and 10 μM lactacystin). Protein concentration was determined using a bicinchoninic acid (BCA) protein assay (Pierce Biotechnology, Rockford, IL). Equal protein concentrations from each sample were mixed with a sample buffer, loaded and separated by sodium dodecyl sulfate-polyacrylamide gel electrophoresis (SDS-

PAGE) on a 10% (v/v) resolving gel. The proteins that were separated by SDS-PAGE were transferred to an Immobilon-P membrane (Millipore) and subsequently probed with antibody against e-cadherin (Abcam), rho-associated protein kinase 2 (ROCK2, BD Transduction Laboratories, San Diego, CA, USA), vinculin (Abcam) for 1 h at room temperature. The membranes were incubated with horseradish peroxidase-conjugated secondary antibody (Abcam) for 1 h at room temperature. The blots were developed using an enhanced chemiluminescence detection system (Amersham Bioscience, Piscataway, NJ). Luminescence was recorded on X-ray film (Fuji super RX, Fujifilm Medical Systems, Tokyo, Japan) and bands were imaged and quantified with an Imaging Densitometer (Bio-Rad, Hercules, CA).

3-2-7. Scanning Electron Microscope analysis

For the SEM observation, the multiscale patterns were sputter-coated with Pt to the thickness of 3 nm prior to measurements. SEM images were obtained using a HITACHI S-4800 microscope (Hitachi, Japan).

3-3. Results

3-3-1. Design of multiscale topography

In the native tissues, nano- and microscale guidance cues exists as forms of lumens of vascular and lymphatic vessels, basement membranes, fibrillar interstitial tissues and space tracks. Since the collagen type I is the most abundant ECM in human tissues, the multiscale patterns coated with collagen type I can present biomimetic physical environment in terms of topography. To generate cell island with comparable size which is about to invade in a physiological condition [73], PDMS stencil with 5 mm hole was used. As shown in the Fig. 3-1A, after the removal of PDMS stencil, the patterned cell island shows clear circle with defined diameter.

In this study, the effect of feature size was studied by using flat, nano groove (width: 550 nm, spacing: 550 nm, and height: 600 nm), and micro groove (width: 5 μm, spacing: 5 μm, and height: 5 μm) patterns (Fig. 3-1B), and the effect of topographic orientation with micro groove, micro concentric (width: 5 μm, inter-circle spacing: 5 μm, and height: 5 μm), and micro radial (width: 5 μm, 3 grooves in 1˚, thus 1080 grooves in 360˚, height: 5 μm). Due to the limited resolution of photolithography, the radial pattern does not have topographic features at the center in a diameter of ~2 mm.

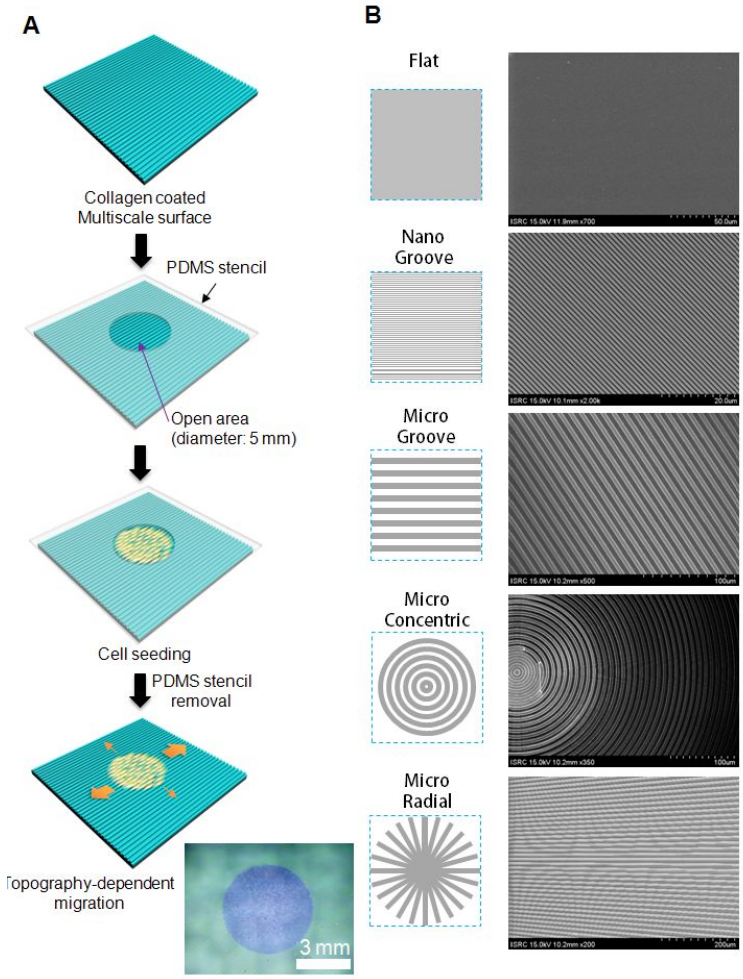

Figure 3-1. (A) Schematic illustration of stencil-induced cell patterning technique used for the generation of two dimensional cell colony. The collagen type I coated multiscale topography presents biomimetic two dimensional microenvironment for cell migration. (B) Representative SEM images of multiscale patterns. The effect of feature size can be analyzed by comparing cell behaviors on flat, nano groove, and micro groove patterns, whereas that of orientation by comparing cell behaviors on micro groove, micro concentric, and micro radial patterns.

3-3-2. Topography-dependent collective and individual migration

When letting two collectively migrating cells (A 431 and MDCK) and two individually migrating cells (U87 and MDA MB-231) migrate freely on the various topographies, the spreading pattern of cell islands shows several differences depending on the cell types and topographies.

First, collectively migrating cells (A 431 and MDCK) spread slowly compared to the individually migrating cells (U87 and MDA MB-231) (Fig. 3-2, 3-4, and 3-5) in the most of the topographies (except concentric pattern). This slow migration speed is due to the maintained cell-cell contacts between the cells, while the migration of individually migrating cells does not affected by the cells nearby (Fig. 3-3). The advancing speed towards major axis was approximately four times faster than that of collectively migrating cells. However, both collectively and individually migrating cells showed directional preference, demonstrating faster spreading following the topographical orientation with preferential polarization towards groove orientation.

Second, the spreading across the topographic orientation was more sensitive in case of individually migrating cells. As shown in Fig. 3-4 and 3-5, on nano groove and micro groove cases, individually migrating cells showed significantly low spreading across the topographic orientation. Such migration across the topography was more difficult in case of microscale due to the longer ridge-to-ridge spacing and larger topographic height.

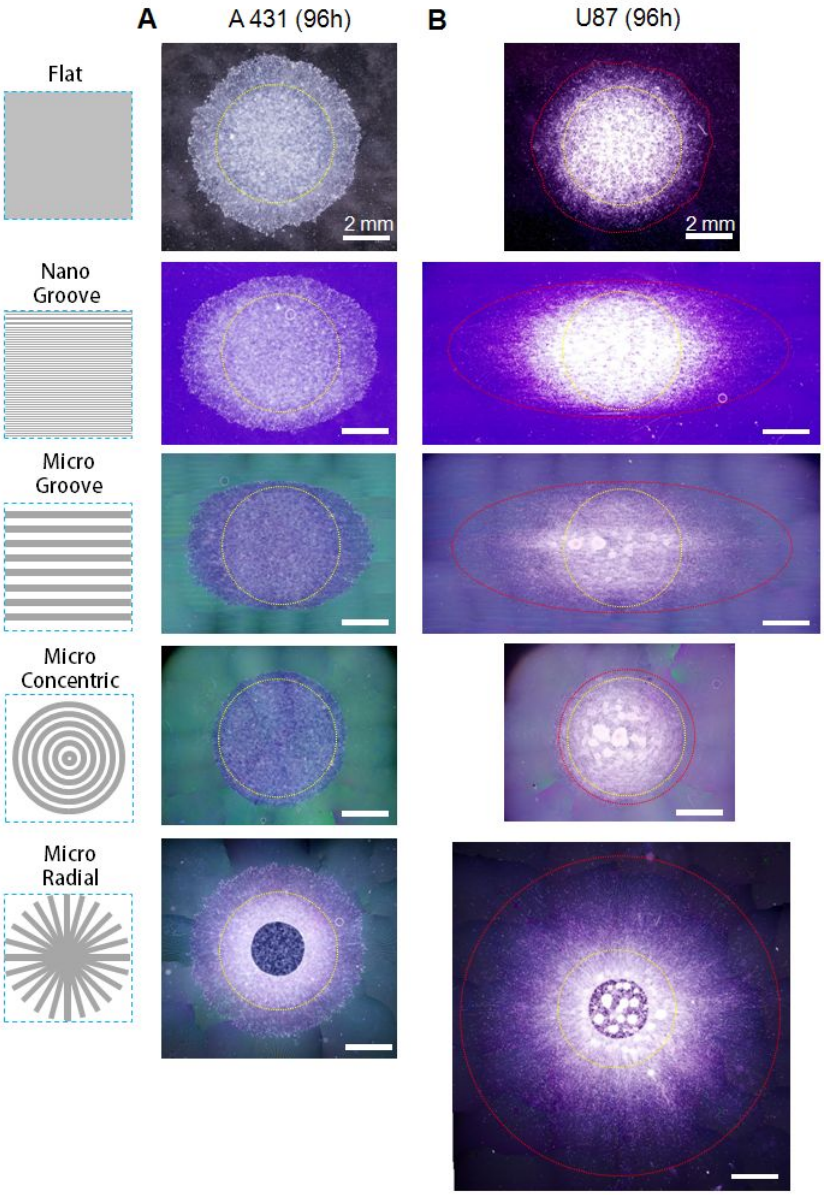

Figure 3-2. Representative microscopic images of cell spreading at 96 h. Yellow dotted line: 0 h, red dotted line: 96 h. (A) A 431, a human epidermoid carcinoma cell which migrate in a collective manner. (B) U87, a human glioblastoma cell line which migrate individually.

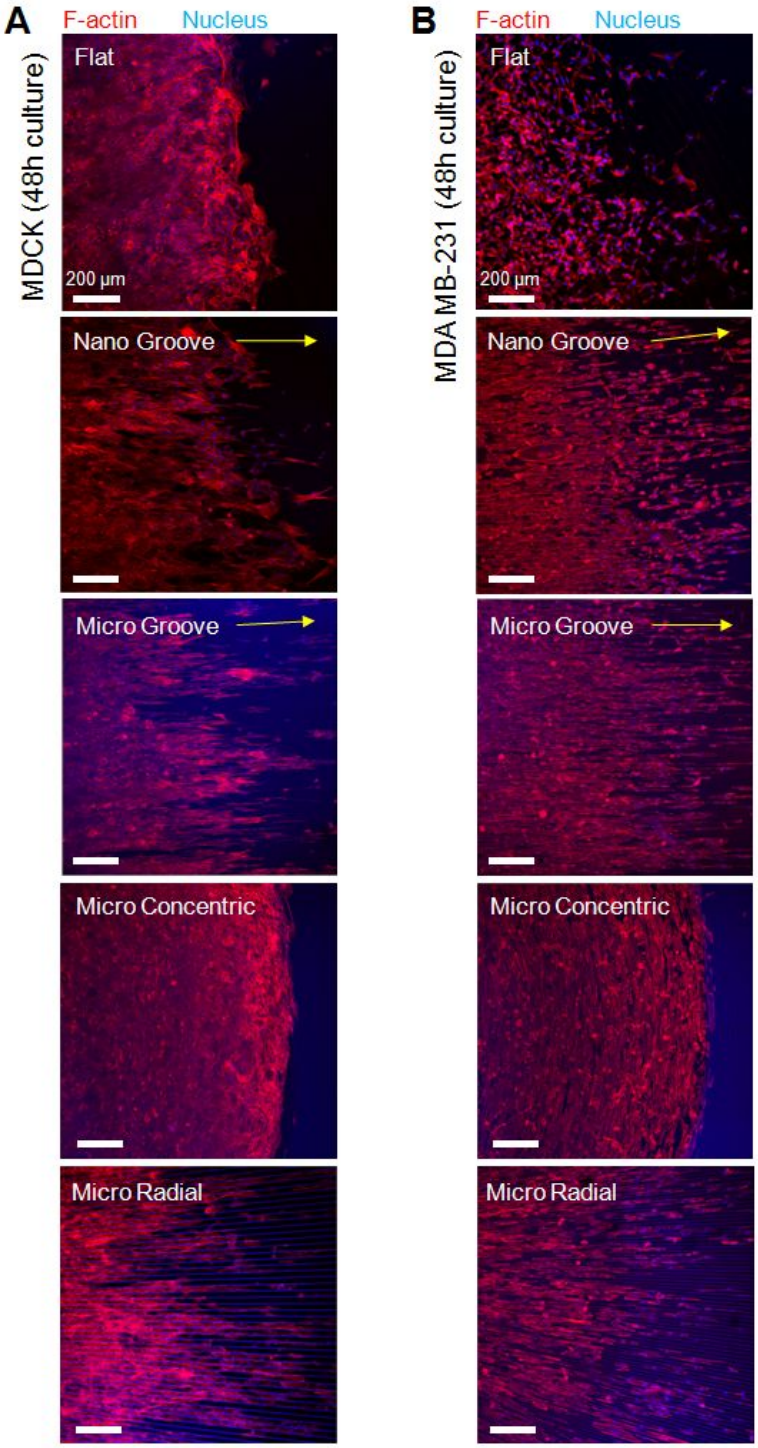
A
F-actin
Nucleus
MDCK (48h culture)
Flat
200 μm
Nano Groove
Micro Groove
Micro Concentric
Micro Radial
B
F-actin
Nucleus
MDA MB-231 (48h culture)
Flat
200 μm
Nano Groove
Micro Groove
Micro Concentric
Micro Radial

Figure 3-3. Immunofluorescence images of migrating cells at 48h. Red: F-actin, blue: nucleus. (A) Madin-Darby canine kidney epithelial cell line (MDCK), a model cell used for collective cell migration. (B) MDA MB-231, a human breast cancer cell line, a individually migrating cell.

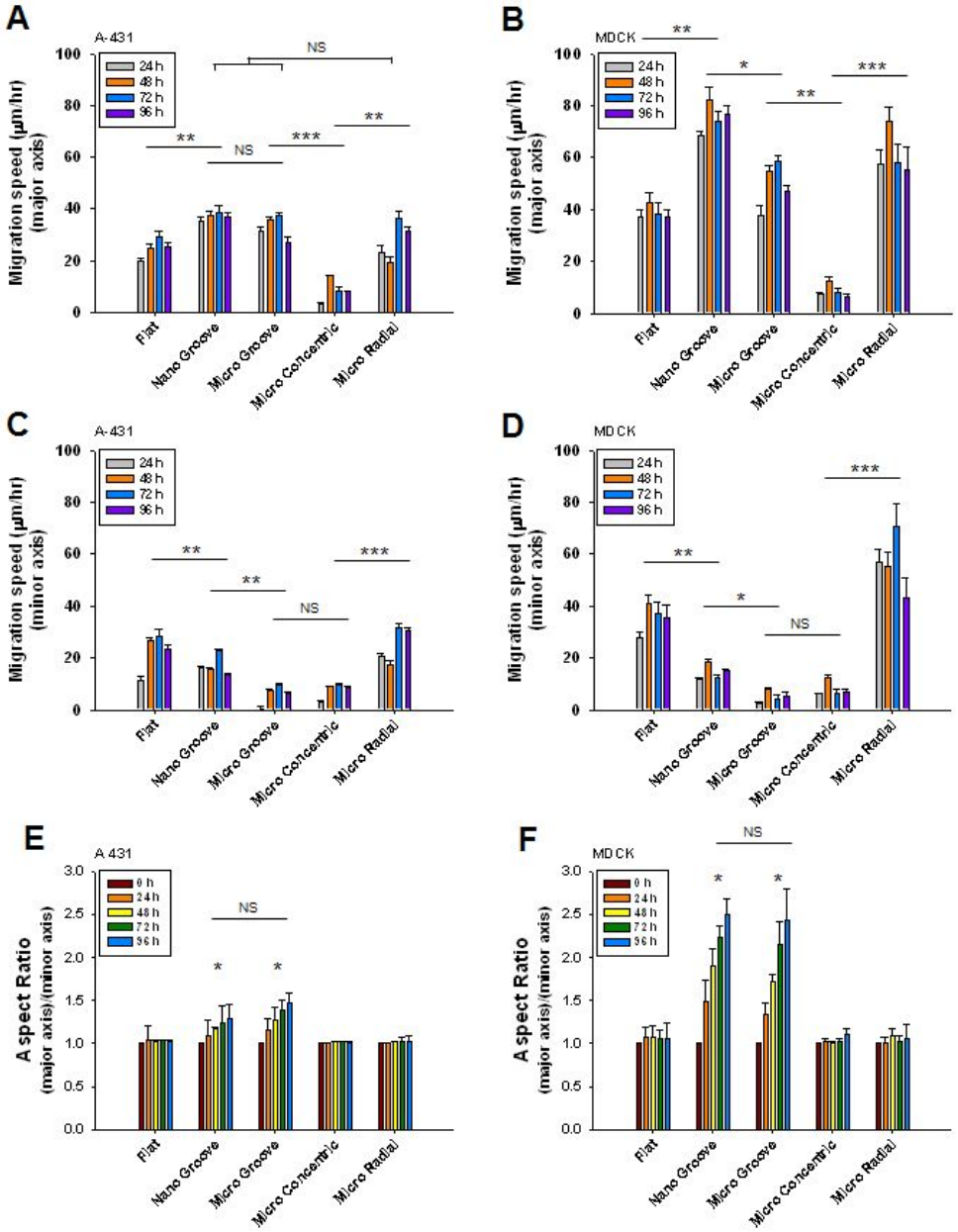

Figure 3-4. Quantified collective migration speed of advancing front (major axis) and lateral side (minor axis), and aspect ratio of major and minor axis. (A, C, and E) A 431. (B, D, and F) MDCK.

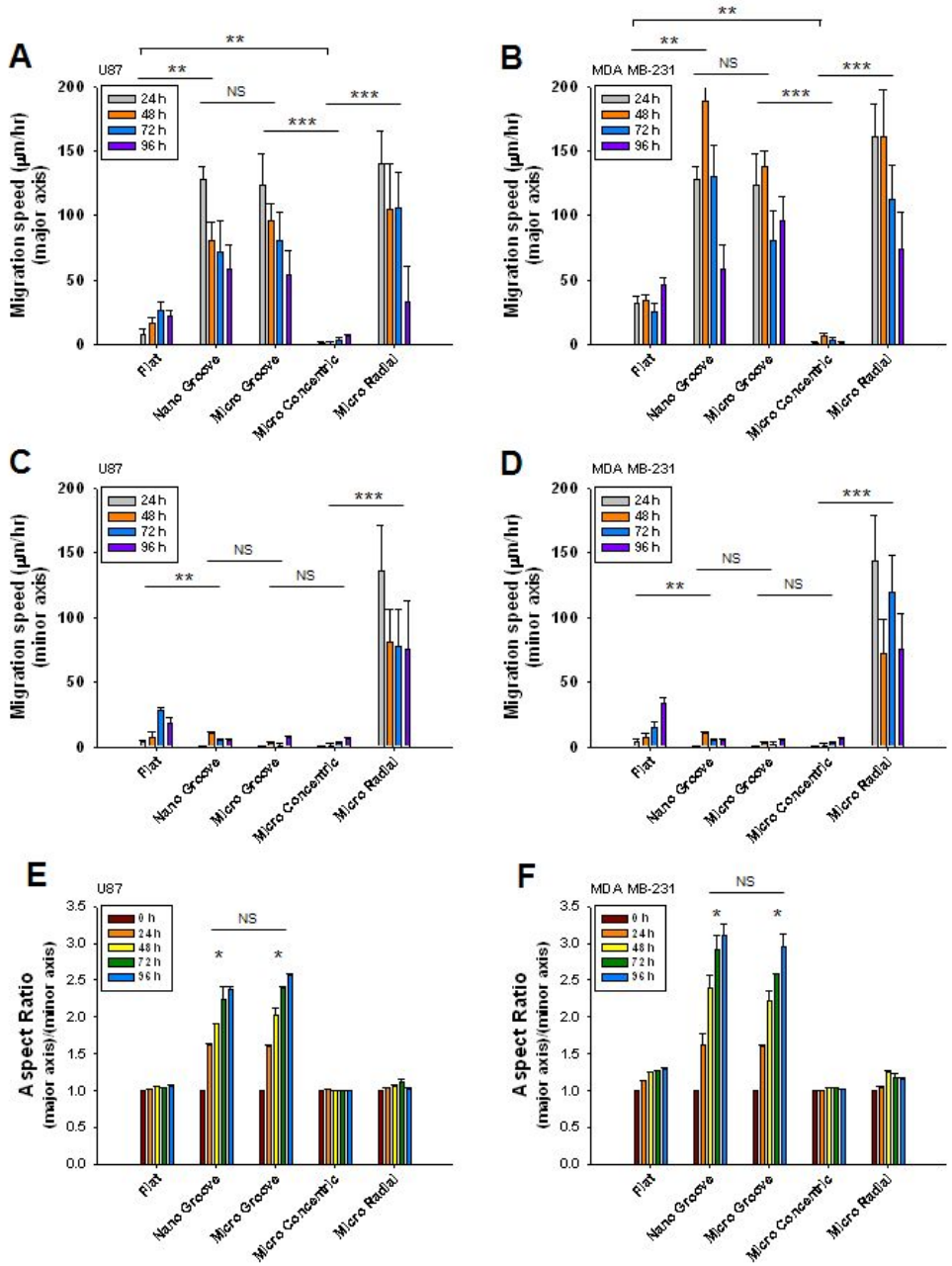

Figure 3-5. Quantified individual migration speed of advancing front (major axis) and lateral side (minor axis), and the aspect ratio of major and minor axis. (A, C, and E) U87. (B, D, and F) MDA MB-231.

Third, when comparing the nano groove and micro groove, the spreading speed following the topography (i.e. major axis) showed no significant difference except the MDCK case (faster migration in the case of nano groove compared to micro groove), implying the dependency on the cell types.

Fourth, the effect of topographical orientation was clear when comparing flat (no preferential orientation), micro groove (uni-directional), concentric and radial (omni-directional) cases. Especially, cells on concentric topography showed limited migration, while the radial case showed comparable migration speed with nano groove and micro groove cases.

3-3-3. Intracellular organization

The observation of intracellular organization can give guidance in the understanding of cell migration. In general (not the case of amoeboid migration), cell migration is governed by organization and amount of f-actin and vinculin which transmit traction force and form focal adhesion onto the substrate, respectively. As shown in Fig. 3-6, the f-actin and vinculin showed preferential alignment towards the topography. The random orientation in the case of flat and alignment orthogonal to the spreading orientation in the concentric case well describe the slow migration speed.

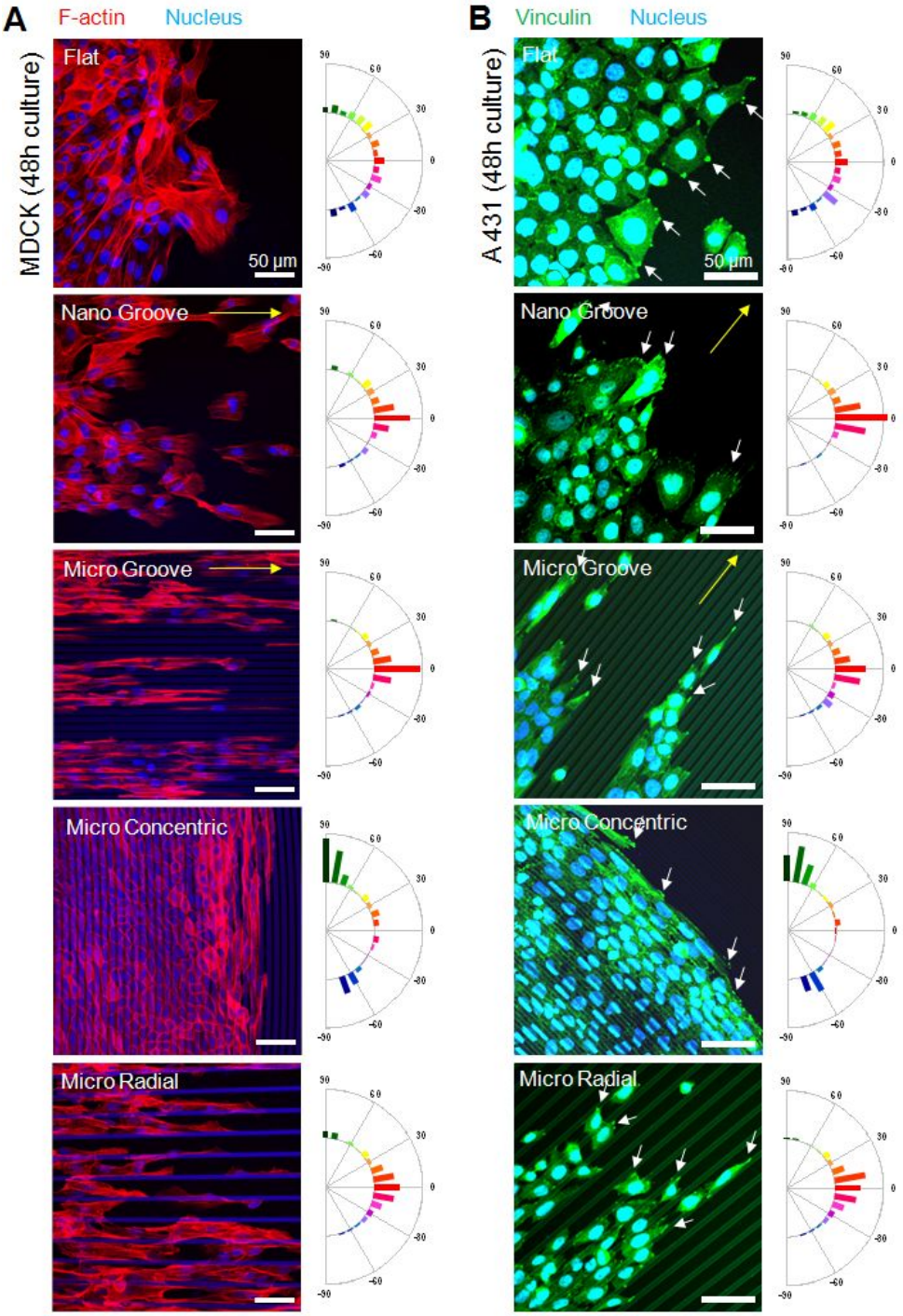
A
F-actin
Nucleus
MDCK (48h culture)
Flat
50 μm
Nano Groove
Micro Groove
Micro Concentric
Micro Radial
B
Vinculin
Nucleus
A 431 (48h culture)
Flat
50 μm
Nano Groove
Micro Groove
Micro Concentric
Micro Radial

Figure 3-6. Alignment of F-actin and vinculin with respect to the underlying multiscale topography in collective migrating cells. Red: F-actin, green: vinculin, and blue: nucleus. (A) MDCK, (B) A 431. Yellow arrow: topographical orientation, white arrow: focal adhesions.

3-3-4. Westernblot assay

The topography not only affect to the apparent migration pattern and intracellular organization, but also to the amount of proteins associated to migration. Here, the level of E-cadherin, ROCK2, and vinculin were visualized by using westernblot assay. E-cadherin is expressed commonly in collectively migrating cells, participating in cell-cell tight junction formation [74, 75]. The Rho-associated protein kinase (ROCK) is an enzyme manly involved in regulating cell shape and motility of cells by modulating polymerization/depolymerization of cytoskeleton [76, 77]. The level of vinculin demonstrates the cell-substrate interaction [78, 79], while the E-cadherin shows the cell-cell interaction.

First, when comparing the topographical size, the level of E-cadherin, ROCK2, and vinculin was higher in micro groove compared to nano groove case in all cell types (Fig. 3-7 and 3-8), presumably due to the relatively quasi-three-dimensional characteristic of micro groove. In micro groove, cells can migrate on both ridges and grooves forming focal adhesion at the bottom of grooves and side walls.

Second, the upregulation or downregulation of E-cadherin was dependent on both topography size and cell types (A 431 and MDCK in Fig. 4-8A and C, respectively). Since the downregulation of E-cadherin is considered as a mediator of epithelial-to-mesenchymal transition (EMT) which is an essential process of

intravasation of tumor cells), the relative expression of E-cadherin in response to topography size can give guidance in the process of EMT [80, 81]. Furthremore, when comparing the effect of topography size (A 431 and MDCK), the trend of vinculin is similar to E-cadherin.

Third, when comparing the effect of topographical orientation, while the individually migrating cells (U87 and MDA MB-231) showed upregulation of ROCK2 and vinculin in radial case, which corresponse to the rapid migration speed in radial case (Fig. 3-8F and H). Interestingly, collectively migrating cells (A 431 and MDCK) showed different trend of E-cadherin, ROCK2 and vinculin, demonstrating low level of such proteins in the case of radial topography compared to micro groove and micro concentric cases.

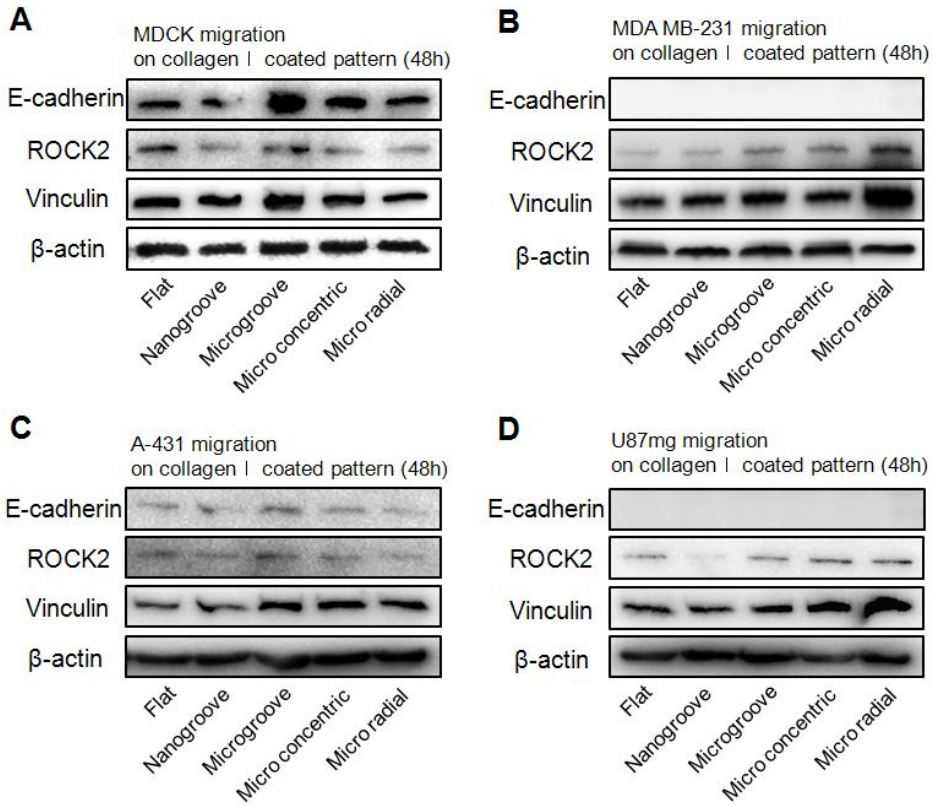

Figure 3-7. Westernblot analysis of E-cadherin, ROCK2, and Vinculin. (A) MDCK, (B) MDA MB-231, (C) A 431, and (D) U87.

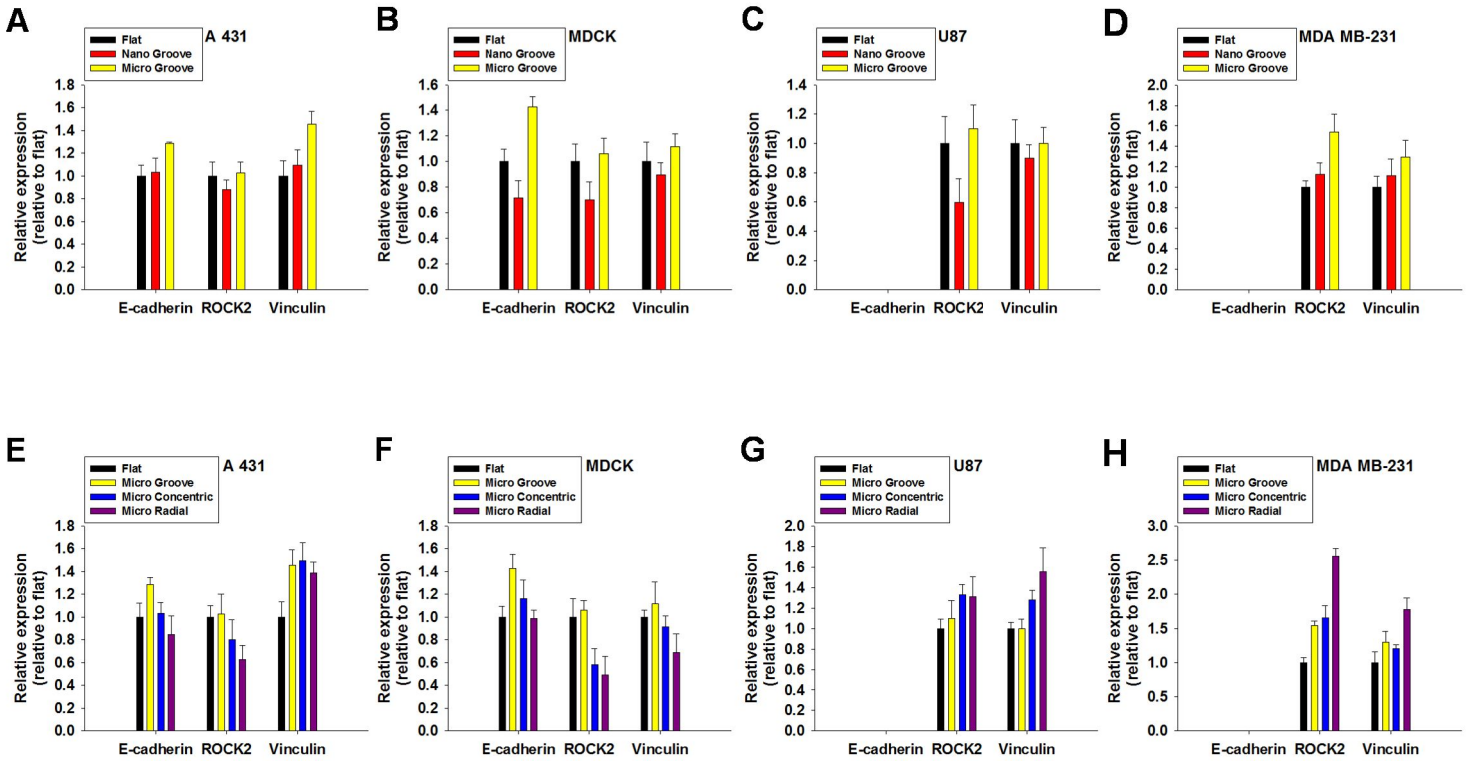
A
A 431
Flat
Nano Groove
Micro Groove
Relative expression (relative to flat)
E-cadherin
ROCK2
Vinculin
B
MDCK
C
U87
D
MDA MB-231
E
Micro Concentric
Micro Radial
F
G
H

Figure 3-8. Quantification of westernblot band in terms of topographical size and orientation. (A, C, E, and G) Effect of topographical size. (B, D, F, and H) Effect of topographical orientation.

3-4. Discussion

In this study, the effects of topographical feature size and orientation on the collective and individual cell migration were demonstrated. Although there are several differences depending on the cell types, the collectively and individually migrating cells showed both similarities and differences in terms of macroscopic migration and microscopic changes such as intracellular organization and upregulation of protein levels in response to physical topography.

To compare the effect of topographical size, we cultured collectively and individually migrating cancer cells on the flat, nanogroove, and microgroove patterns. In terms of feature size, the focal adhesion and cell adhesion shows primary differences. For example, on the nanogroove patterns, focal adhesion complexes are highly developed and aligned towards the topographical orientation, but on the flat and microgrooves focal adhesion complexes are less developed compared to nanogrooves due to the large difference of critical dimensions between unit focal adhesion and size of topography. However, the alignment of focal adhesion is also observed in the microgroove case. In addition, cells on the microgroove patterns penetrate into the interstitial space of grooves thus make quasi three-dimensional adhesion. Since such penetration increases contact area, and ultimately enhance the probability of focal contacts.

In terms of topographical orientation, underlying topography can inhibit

or promote migration *via* 'contact guidance' mechanism. For example, the groove structure promotes uni-directional migration, and radial pattern induces omni-directional migration. However, the concentric pattern limits migration due to the orthogonal alignment of focal adhesion and f-action with respect to the spreading orientation.

Although other factors including heterotypic cell-cell interaction, hypoxia condition, growth factors were not considered, the effect of basement membrane (nanoscale), microtracks and conduits (microscale) on the migration was demonstrated. Since cells usually migrate following the readily existing multiscale topography in the case of collective migration [83], the macroscopic behaviors are predominantly guided by the orientation of topography. Furthermore, the change of protein level expression implies that the cellular activity can be changed upon the topography-guided migration steps compared to the colony stage. Especially, in the case of collective migration, the expression level of E-cadherin and vinculin was changed depending on the topography. In the case of MDCK, cells showed dissemination at the advancing front in response to the nano groove, micro groove and radial pattern (from the immunofluorescence images in Fig. 3-6), but such behaviors were less observed in A 431 cell, indicating the cell type-dependent EMT process.

3-5. Summary

In this study, the topography-guided migration characteristics of collective and individual cell migration were observed using four types of cells. Although both collective and individual cell migration showed sensitivity to topographical feature size and orientation, the individually migrating cells responded more sensitively to the topography. Furthermore, the topographical orientation induced larger difference in macroscopic cell migration speed and microscopic organization of f-actin and vinculin compared to the topographical feature size. These results indicate that the cancer cell migration *in vivo* following the basement membrane, microtracks, and lymphatic vasculature might be significantly affected by the feature size and orientation. It is believed that this topography-dependent and cell phenotype-dependent macroscopic and microscopic difference may give guidance in the study of *in vivo* dynamic cancer invasion.

Chapter 4. The effect of spring constant and slanted angle of nanopillars on the alignment of cells

4-1. Introduction

Cells sensitively response to various cues such as chemical concentration, rigidity, density of anchoring points and electrical field [31]. Especially, the surface topography is one of the important factors that can control cell functions by developing intracellular mechanical tension depending on the size, orientation and stiffness [84, 85]. Among the surface topography, the grooved structures are adapted in many studies due to the physiological relevance of nano/microscale fibrous structures in many tissues *in vivo* [86]. On such grooved structures cells demonstrated controlled spreading [44, 87], migration [88, 89], proliferation [51], cell division [49], tissue function [20], and tissue formation [90], and differentiation of stem cells [19]. On the other hand, the pillar structures were less studied since they are rarely found in the *in vivo* microenvironment. However, its strong potential has gained much interest since it presents a broad range of tunability in mechanical stiffness *via* simple geometric control of diameter, height and elastic modulus of materials [91, 92].

Recently demonstrated pillars are usually focused on micropost arrays

made of elastomeric materials, usually with diameter of few micrometers. These pioneering studies have demonstrated (i) the measurement of cellular traction forces in single cell and multicellular level, and (ii) the regulation of differentiation of mesenchymal stem cells [91, 92]. Furthermore, the usefulness of mechanical stiffness in regulation of cell functions drew much attention since recently a report has revealed the underlying mechanism that such mechanical regulation is governed in molecular delivery of YAP in between cytoplasm and nucleus [93]. Although these studies have demonstrated interesting aspect of post structures in engineering and science, it seems that further room for more sophisticated regulation with nanoscale cue is available. For example, by reducing diameter of nanopillars one order of magnitude, cells can contact 100 times larger number of nanopillars, thus more sophisticated engineering of cell behavior is possible. In terms of traction force visualization, nanopillars can present higher spatial resolution compared to micropillars [91]. In addition, the cell behavior can be changed depending on the feature size [31].

In this study, we present engineering of cellular behavior especially in alignment with polymeric nanopillar arrays. In the first section, we study the relation between the alignment behaviors and the local deformation by tuning spring constants of dense nanopost arrays. To this end, nanopost arrays (diameter of 400 nm) having various stiffness (i.e. spring constant) were fabricated with various height (2000 and 600 nm) and mechanical properties (19.8 and 320 MPa).

Furthermore, in the second section, to understand underlying mechanism of mechanosensing with respect to the leaning angle, slanted nanopillars with various angles (90, 75, 60, 45 and 30˚) with same diameter (400 nm) were prepared. On these controlled nanohairy topography, mechanically sensitive NIH-3T3 fibroblasts were cultured and their behaviors were analyzed.

4-2. Materials and methods

4-2-1. Fabrication of slanted PUA nanopillars

Polyurethane acrylate (PUA) nanopillars were prepared by capillary force lithography (CFL), replicating pre-patterned silicon masters with UV-curable PUA materials [34, 35]. PUA prepolymers (MINS 310RM for soft PUA and MINS 311RM for hard PUA) were purchased from Minuta Tech. (South Korea). Here, the only difference between 301RM and 311RM is the relative composition of hard modulator incorporated in PUA pre-polymer. Various silicon masters having nano-holes were fabricated by a series of MEMS machining steps such as thin film deposition, photolithography, and dry etching. Detailed fabrication steps can be found elsewhere [94, 95]. Then, a small amount of PUA prepolymer (~10 μl) was drop-dispensed onto the silicon master and polyethylene terephthalate (PET)

film (thickness of 50 μm, used for backing) was brought into contact. After mildly pressing with a roller several times, the liquid pre-polymer was cured by UV exposure (λ=250-400 nm) for a few tens of seconds. After UV curing, the solidified PUA attached onto PET backing was peeled from the master, and fully cured with UV light for additional 5 hours. To prevent potential swelling and fixation for imaging, the patterned nanopillar array backed by PET film was integrated onto the cover slip (diameter of 25 mm) using UV curable glue (NOA 71, Norland Optical Adhesive, USA).

4-2-2. Cell culture

NIH-3T3 cells (American Tissue Culture Collection) were cultured in Dulbecco's modified Eagle's medium (DMEM) (Invitrogen) supplemented with 10% fetal bovine serum, 1% Glutamine, and 1% penicillin/streptomycin at 37 °C and 5% CO_2. Prior to cell seeding, the patterned substrates were sterilized in UV chamber for 1 h and then coated with 5 μg/ml fibronectin for 12 h. Cell seeding density was maintained in $10^4/cm^2$ throughout the experiment.

4-2-3. Imaging and analysis

Cells were imaged using inverted Olympus microscope (IX71, Olympus Inc.,

Japan). The alignment and morphogical index were analized by using Image J program (National Institute of Health, Bethesda, USA).

4-2-4. Scanning Electron Microscopy (SEM) imaging

For SEM imaging, cells were washed with PBS and fixed with 5 % glutaraldehyde for 30 min in 4°C. After removal of the fixative, cells were incubated with 0.1 M sodium cacodylate and 0.1 M sucrose for 30 min. After washing with PBS and distilled water for 5 min, cells were dehydrated by serial addition of 35 %, 70 %, 85 %, 95 % and 100 % of ethanol solutions for 10 min each. Then cells were immersed in hexamethyldisilazane (HMDS) for 5 min. After drying the samples, the substrates were sputter-coated with Pt to the thickness of 3 nm prior to measurements. SEM images were obtained using a HITACHI S-4800 microscope (Hitachi, Japan).

4-2-5. Signaling inhibitor treatment

The Y 27632 (Sigma-Aldrich, USA) was treated at time point of 0h and 24h after seeding with concentration of 10 μM. The NSC 23766 (Tocris Bioscience, UK) was treated at the time point of 0h and 24h after seeding with concentration of 100 μM. Alignment was measured from the microscopic images obtained at 24h timpe

point after the treatment.

4-2-6. Quantitative reverse transcriptase polymerase chain reaction (qRT-PCR)

Cells were lysed in TRIzol reagent (Invitrogen). Total RNA was extracted with chloroform (Sigma) and precipitated with 80% (v/v) isopropanol (Sigma). After the supernatant was removed, the RNA pellet was washed with 75% (v/v) ethanol, air-dried and dissolved in 0.1% (v/v) diethyl pyrocarbonate-treated water (Sigma). The total RNA concentration was determined using a NanoDrop spectrometer (ND-2000, NanoDrop Technologies, Wilmington, DE). Reverse transcription was performed using 1 μg of pure total RNA and Superscripts II reverse transcriptase (Invitrogen), and the synthesized canal was amplified by RT-PCR. qRT-PCR was performed using the StepOnePlus real-time PCR system (Applied Biosystems, Foster City, CA) with qPCR 2X PreMix with SYBR green (Enzynomics, Daejeon, Republic of Korea). After 5 min of pre-incubation, 35 amplification cycles were performed and each cycle consists of three steps; 30 s at 94 °C, 45 s at 60 °C, and 45 s at 72 °C. For each target, we used mouse glyceraldehyde 3-phosphate dehydrogenase (GAPDH), Bax, Bcl-2, Focal Adhesion Kinase (FAK), Ras homolog gene family, Rac 1, integrin β1, c-Jun N-terminal kinase 1 (JNK1), Wnt 3a, and Wnt 5a. The expression level of the target genes was determined using the comparative Ct method, whereby the target was normalized to the endogenous

reference (GAPDH) [96]. Relative gene expressions of 3T3 cells cultured on the pillars were evaluated. All of the data were analyzed using the $2^{-\Delta\Delta Ct}$ method.

Target gene	Sense primer	Antisense primer
Bax	TGTTTGCTGATGGCAACTTC	GATCAGCTCGGGCACTTTAG
Bcl-2	GGGAGGATTGTGGCCTTCTT	ATCCCAGCCTCCGTTATCCT
FAK	GCGATCCTATTGGGAGATGA	TTTTGGCCTTGACAGAATCC
Rac	ACTCATTCCAGACCCACGAC	GTCCAGGGCAGACACAATCT
Integrin β1	GGTGTCGTGTTTGTGAATGC	TGACGCTAGACATGGACCAG
JNK 1	CGGAACACCTTGTCCTGAAT	GAGTCAGCTGGGAAAAGCAC
Wnt 3a	GGGACCCCAGTACTCCTCTC	GGGCATGATCTCCACGTAGT
Wnt 5a	CTGGCTCCTGTAGCCTCAAG	GCCGCGCTATCATACTTCTC

Table 4-1. Primer sequences used for qRT-PCR analysis.

4-3. Results

4-3-1. Effect of spring constant

4-3-1-1. Cells aligned along the arrangement of nanopillars

To study the sensitivity of cells on mechanically variable nanopillar structures, three type of nanopillars (diameter of 400 nm identically) were prepared by modulating height of pillars (height of 2000 nm and 600 nm, corresponds to aspect ratio of 5 and 1.5, respectively) and elastic modulus of polymeric materials (soft PUA and hard PUA, having elastic modulus of 19.8 and 320 MPa, respectively) (Figure 4-1A and B). It is noted that the soft and hard PUA have identical composition except for the small difference in the concentration of hard modulator. According to the calculation of mechanical spring constant, the three nanopillars have spring constant of 9.33, 345.58 and 5585.05 nN/μm. Spring constant (k_{bend}) of pillars having circular cross-section can be calculated using following equation [91, 97]:

$$k_{bend} = \frac{3\pi E D^4}{64 H^3}$$

Here, E is elastic moduli of material, D diameter, H height, respectively. For the calculation, D=400 nm, H= 2000 and 600 nm, E= 19.8 and 320 MPa were used. Nanopillars having spring constant of 9.33 and 345.58 are composed of

same elastic modulus materials and with different heights, while those having spring constant of 345.58 and 5585.05 have same height and different elastic modulus.

When cells were cultured for 24 h, cells showed preferred bi-axial alignment along to 0 and 90° as shown in Fig. 4-1B. Interestingly, the degree of alignment decreases as the spring constant increases from 9.33 to 5585.05. We hypothesized that such alignment might be due to the rectangular arrangement of nanopillars, thus seeded cells on hexagonally ordered nanopillar array. As shown, cells on hexagonal array demonstrated preferential tri-axial alignment to 0, 60, and 120° (Fig. 4-2), implying that the arrangement of nanopillars truly affects the cellular alignment.

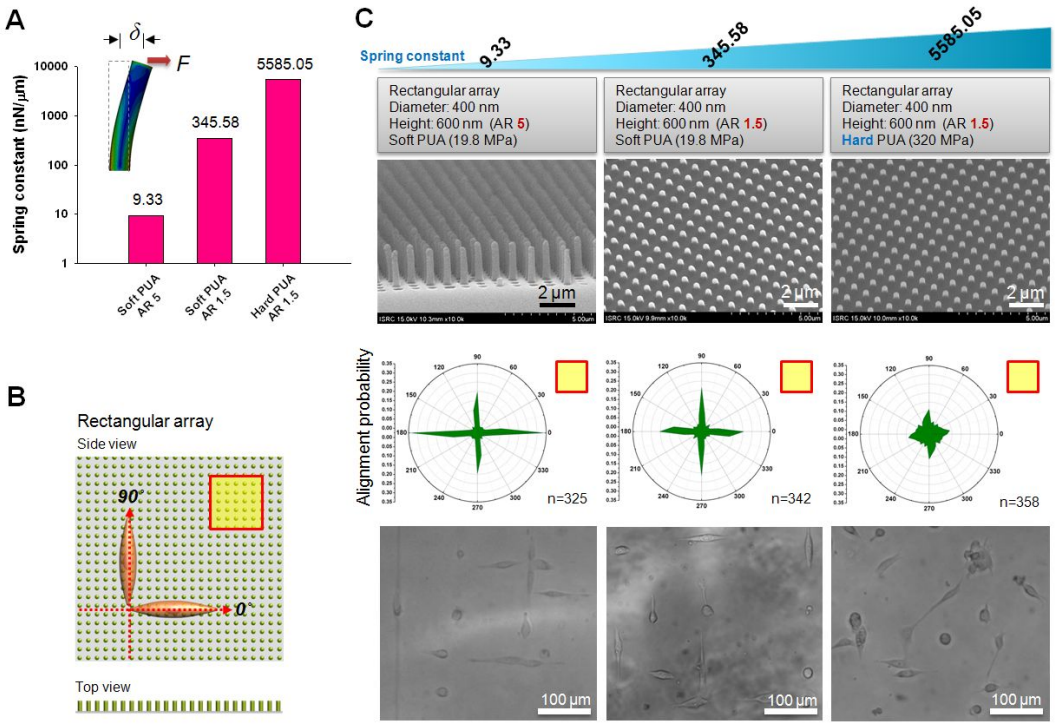

Figure 4-1. Cellular alignment with respect to the spring constant. (A) Spring constant of nanopillars used in this study. For the control of spring constant, height of nanopillars (2000 and 600 nm) and elastic modulus of materials (19.8 for soft PUA, and 320 MPa for hard PUA) were controlled. AR: aspect ratio. (B) Schematic illustration of rectangular nanopillar array. (C) Scanning electron microscope images of used nanopillar arrays and cellular alignment (NIH-3T3 fibroblast) in response to the spring constants.

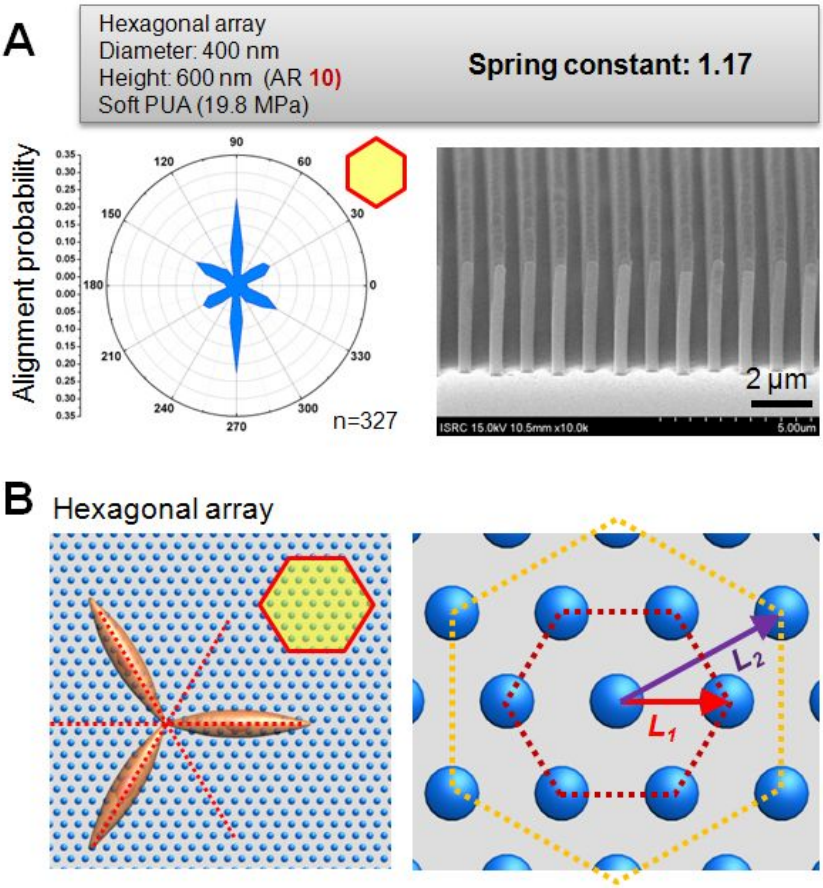

Figure 4-2. Alignment of cells in response to the hexagonal nanopillar array. (A) Cellular alignment and representative SEM image. (B) Schematic illustration of hexagonal array.

4-3-1-2. Cellular alignment is regulated by mechanical tension exerted by nanopillars

To explain how the arrangement of pillars may affect to the cellular alignment, the angular effect on rectangular array was characterized. As shown in the schematic illustration (Fig. 4-3A), the cells are preferentially aligned along the L_1 orientation (corresponse to 0 and 90°), not to the L_2 orientation. Since the NIH-3T3 fibroblast is mechanically sensitive cell, mechanical tension exerted by the nanopillars might be a crucial regulator of alignment. When cells aligned L_1 direction compared to L_2 direction, cells can pull more pillars towards them (shorter pillar-to-pillar distance), and thus can develop more intracellular tension. According to the calculation, cells can contact the most population of nanopillars when aligned to 0 and 90°, while the least population when aligned to 45°. As shown in Fig. 4-3B, such trend of number of nanopillars corresponds to alignment of cells.

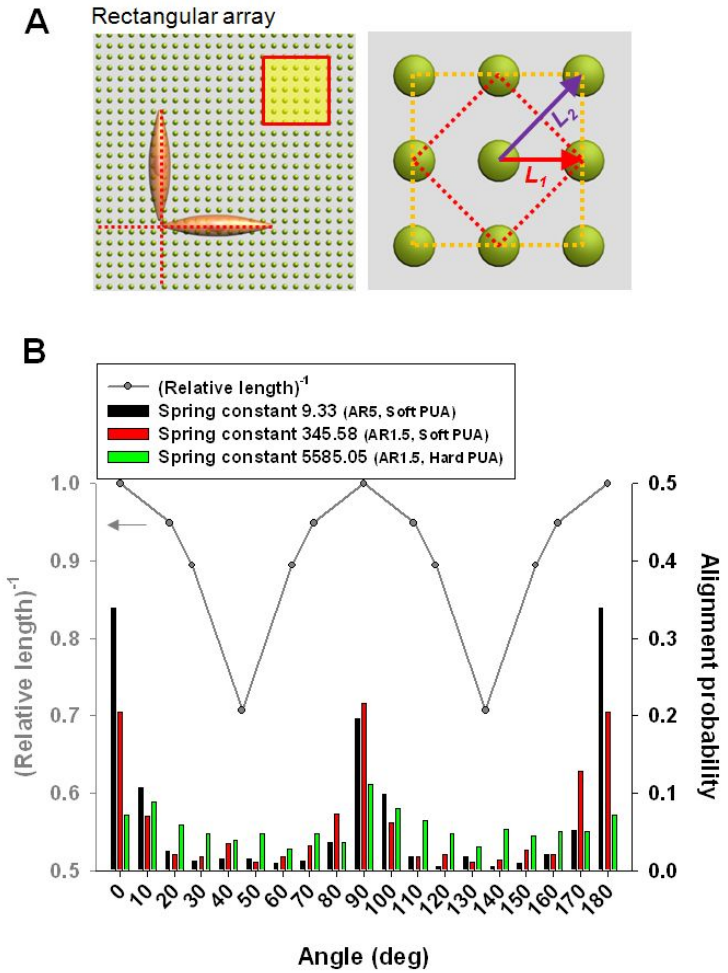

Figure 4-3. Comparison of density of nanopillars with respect to orientation and its effect on cellular alignment. (A) Schematic illustration of rectangular nanopillar array. (B) Inverse of relative inter-pillar length *versus* cellular alignment. The relative inter-pillar length was determined by letting L_1 as unity.

4-3-1-3. Bending of nanopillars is crucial for the recognition of underlying mechanical anisotropy

To study the effect of spring constant on cellular alignment, the detailed cellular morphologies as well as the bending of nanopillars were observed using SEM. As shown in Fig. 4-4A, cells adhered on low spring constant nanopillars (9.33) showed significant pulling of nanopillars towards them using their philopodia and lamelipodia. On the other hand, cells on stiff nanohairs (5585.05) barely bend the underlying pillars towards them. According to the quantification of pillar bending (demonstrated as displacement ratio which is the relative displacement with respect to the height of pillars), the normalized displacement of pillar top is decreased as the spring constant increases. When comparing the previously described alignment trend, it is clear that the deformation of pillars is essential to give sufficient information on the mechanical anisotropy of underlying substrate. As described in Fig. 4-4B, cells on stiff environment may not feel the mechanical anisotropy since the difference of tension cannot be sensed due to the limited deformation. However, if the underlying substrate is sufficiently deformable, cells can sense the mechanical anisotropy with the pulling force, and thus developing their intracellular tension.

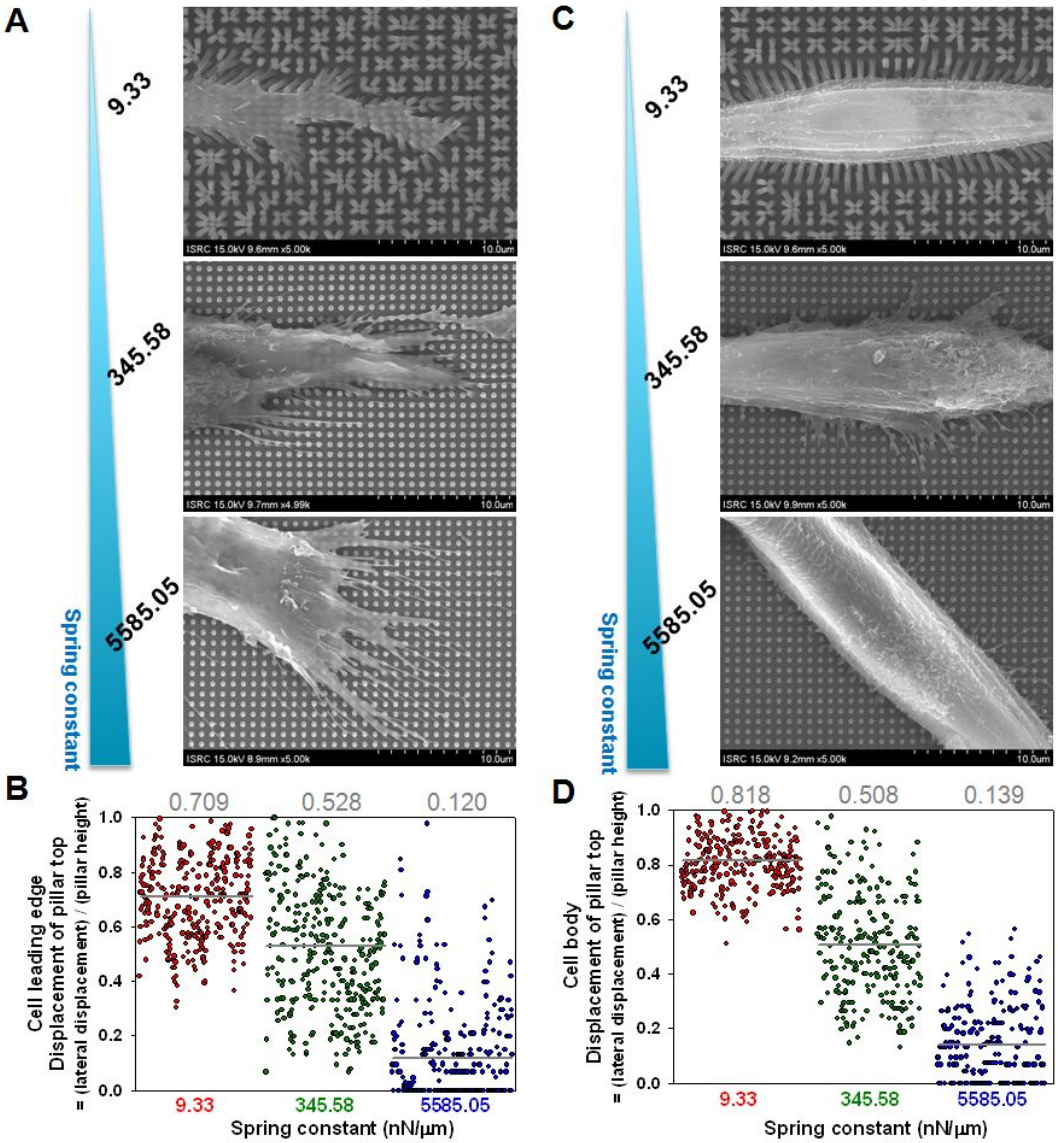
A
9.33
345.58
5585.05
Spring constant
C
9.33
345.58
5585.05
Spring constant
B
0.709
0.528
0.120
Cell leading edge
Displacement of pillar top
= (lateral displacement) / (pillar height)
9.33
345.58
5585.05
Spring constant (nN/μm)
D
0.818
0.508
0.139
Cell body
Displacement of pillar top
= (lateral displacement) / (pillar height)
9.33
345.58
5585.05
Spring constant (nN/μm)

Figure 4-4. Traction-induced deflection of underlying nanopillars with filophodia in the leading edge and in lateral side of cell body. (A, C) Representative SEM images of bent nanopillars in leading edge (A) and lateral side of cell body (C). (B, D) Quantified deflection of nanopillars with respect to the spring constants. The displacement of nanopillars was normalized with the ratio of lateral displacement of nanopillars to pillar height. The average values were displayed at the top of graphs.

To verify which signaling pathway mediates such alignment, we conducted signaling inhibition study by the treatment of Y 27632 (a Rho kinase inhibitor) and NSC 23766 (a Rac inhibitor). When the Y 23766 (concentration of 10 μM) was introduced, the alignment showed no significant different regardless of the treatment time point. However, when NSC 23766 (concentration of 100 μM) was treated at 0h, cells did not spread although they displayed adhesion on the nanopillars. However, cells showed spreading even under Y 27632 treatments on the flat substrate. Furthermore, cells did not show any significant difference when treated with Y 27632 and NSC 23766 at 24 h. This indicates the mechanosensing may occur in the initial stage of adhesion through the Rac signaling pathway. Since Rac signaling mediates sprouting and dynamics of filopodia at the lateral side of cells [98], it can be said that the bending by the cell body might be more important rather than that of leading and trailing edge.

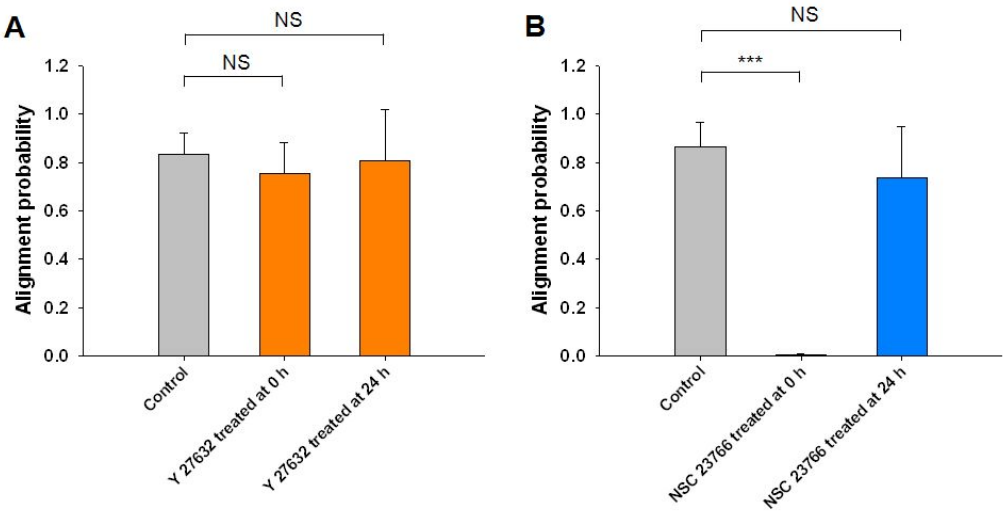

Figure 4-5. Treatment of Y 27632 (a ROCK inhibitor) and NSC 23766 (a Rac inhibitor) at time point of 0 h and 24 h after seeding. Alignment was quantified from the obtained microscopic images at 24 h after treatment. (A) Y 27632 treatment (10 μM) at 0 h and 24 h. (B) NSC 23766 treatment (100 μM) at 0 h and 24 h.

4-3-1-4. Apparent cellular geometries were also governed by spring constant

As shown in Fig. 4-6, apparent cellular morphologies are also regulated by spring constant. According to the quantification, cells showed higher projected area, perimeter, length of major axis and axial ratio in the softest spring constant. However, no significant difference was observed in between the intermediate (345.58) and hard (5585.05) spring constants. It seems such difference is probably resulted from (i) no difference of the pillar height in between the intermediate and hard spring constant pillars (compared to the large difference of height in soft and intermediate nanopillars) or (ii) due to the relatively small difference of spring constant (compared to the two orders of magnitude difference in between soft and intermediate spring constants of nanopillars).

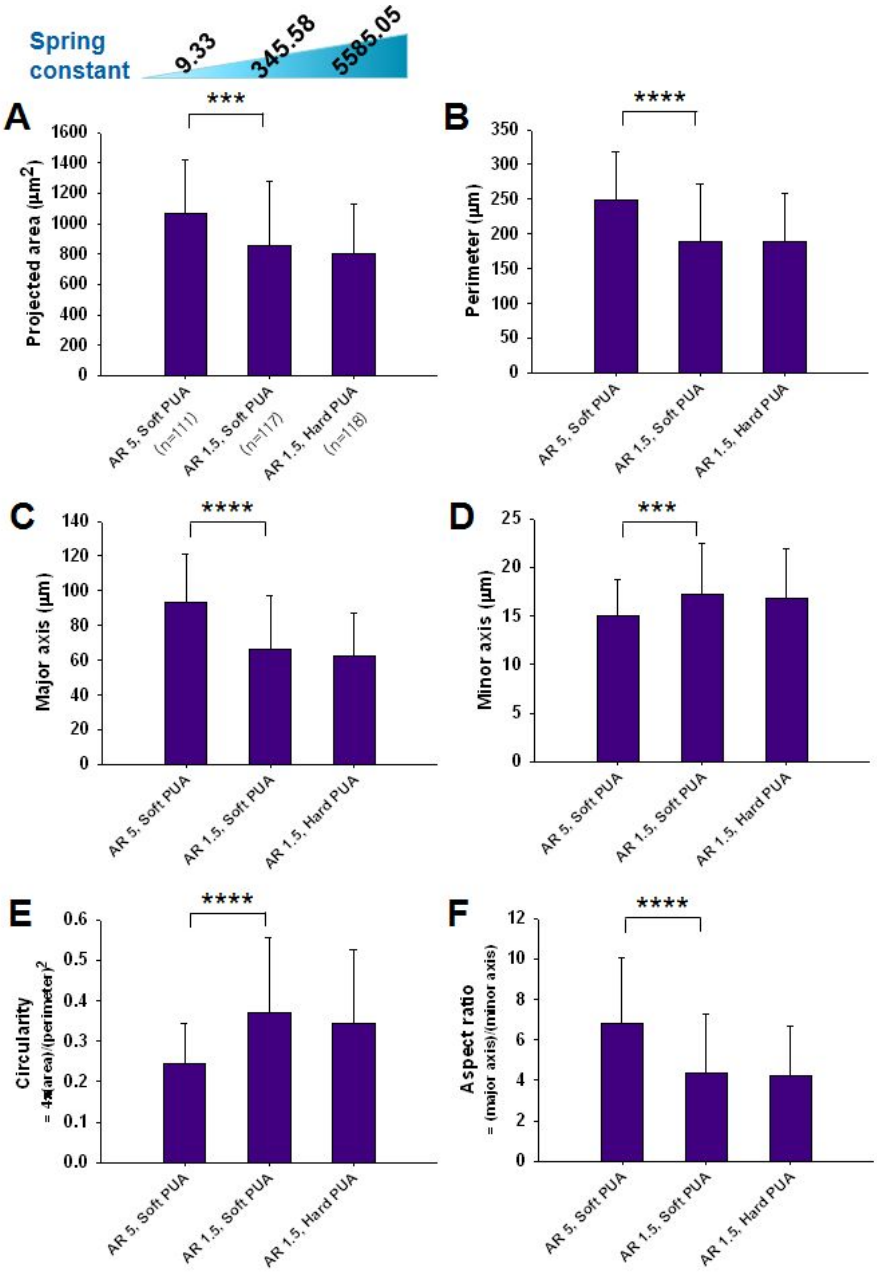

Figure 4-6. Apparent cellular morphologies with respect to the spring constants. (A) projected area, (B) perimeter, (C) major axis, (D) minor axis, (E) circularity and (F) aspect ratio.

4-3-2. Effect of slanted angle

4-3-2-1. Two distinct effects on cell alignment

When NIH-3T3 fibroblast cells were cultured on slanted nanopillars (30, 45, 60, 75 and 90˚), cells demonstrated two distinct alignment pattern. As shown in Fig. 4-7A and B, on the relatively vertical pillars (such as 90˚ and 75˚) cells usually aligned bi-directionally (x and y axis), following the results described above. On the other hand, cells on relatively leaned nanopillars clearly demonstrated uni-directional alignment, which is similar alignment observed on nanogroove topography. Here, the former can be termed 'array effect' since such bi-directionality was originated from the organization of array, the latter can be termed 'angle effect' since such effect was only observed when the pillars were slanted (Fig. 4-7C). As shown in the Fig. 4-7B, the portion of alignment orientation perpendicular to slanted angle (y axis) is decreasing as the pillars inclined from 90˚ to 30˚, and barely observed in 30˚ nanopillars. This means that the relative contribution of 'array effect' decrease as the amount of inclination increases. To verify the relative contribution of these two effects, array effect and angle effect was defined as:

$$\text{Array effect} = (\text{total aligned cells to } 0^\circ \pm 10^\circ \text{ and } 90^\circ \pm 10^\circ) \times \frac{(\text{alignment probability towards } 0^\circ \pm 10^\circ)}{(\text{average probability of } 0^\circ \pm 10^\circ \text{ and } 90^\circ \pm 10^\circ)}$$

$$\text{Angle effect} = \frac{(\text{alignment probability towards } 90^\circ \pm 10^\circ)}{(\text{average probability of } 0^\circ \pm 10^\circ \text{ and } 90^\circ \pm 10^\circ)}$$

Here, 0˚ represents the orientation perpendicular to the inclination (x axis), while 90˚ orientation parallel to the inclination (y axis). As shown in Fig. 4-7D, array and angle effects showed antagonistic trend, demonstrating maximum angle effect at 30˚ and maximum array effect at 90˚.

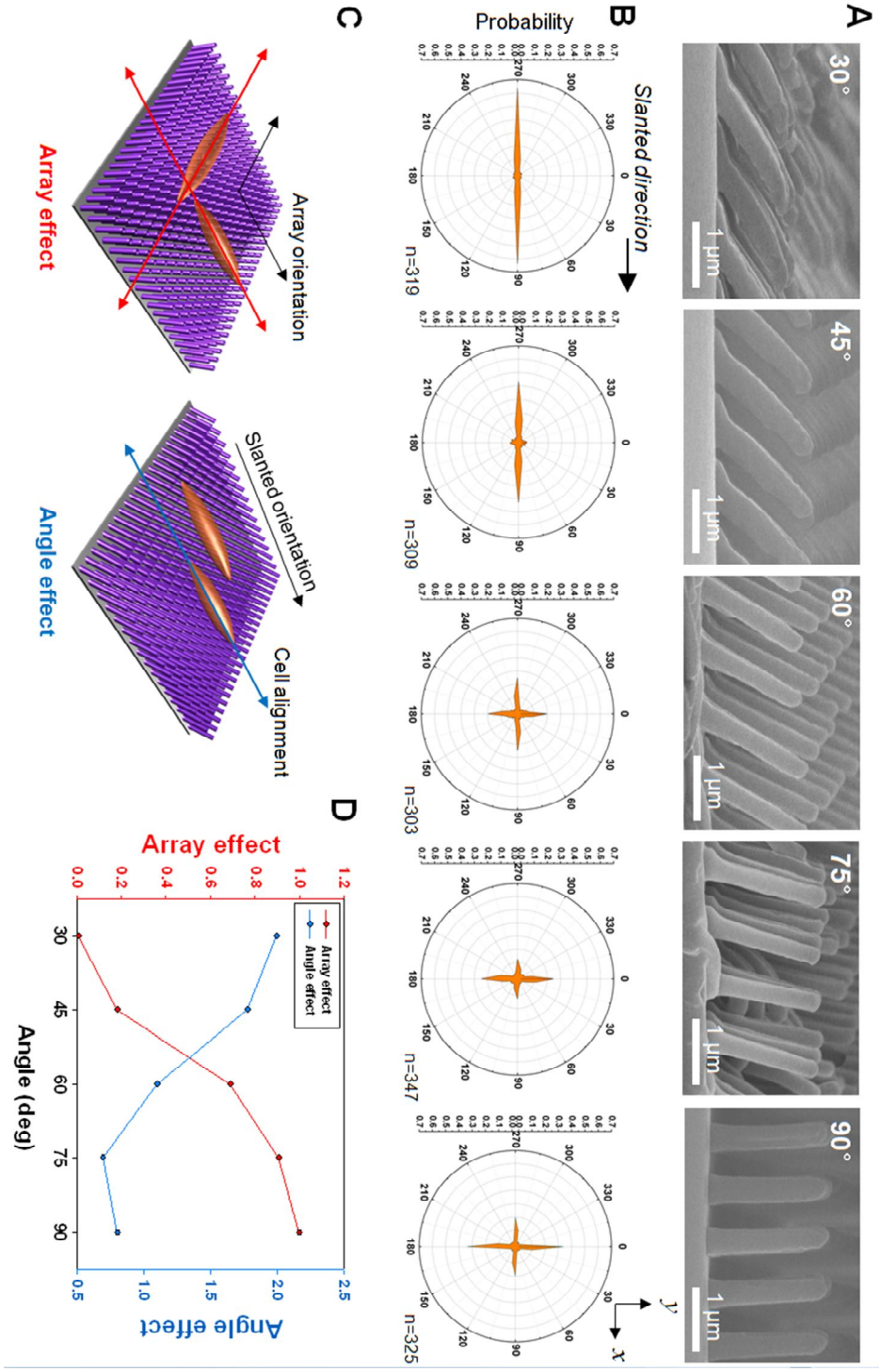
A
30°
45°
60°
75°
90°
1 μm
B
Slanted direction
Probability
n=319
n=309
n=303
n=347
n=325
C
Array orientation
Slanted orientation
Cell alignment
Array effect
Angle effect
D
Array effect
Angle effect
Angle (deg)

Figure 4-7. Effect of slanted angle on the alignment of cells. (A) Representative SEM images of slanted nanopillars. (B) Cellular alignment with respect to the slanted angle. As shown, cells showed bi-directional to uni-directional transition as the angle decreases from 90˚ to 30˚. (C) Schematic illustration of two effects; array and angle effects. Cells aligned bi-directionally in response to the array effect, predominantly observed in relatively vertical pillars (such as 90˚). On the other hand, cells aligned uni-directionally following the slanted orientation, which can be termed angle effect, predominantly observed in relatively slanted pillars (such as 30˚).

4-3-2-2. SEM observation

SEM analysis showed that cells pull nanopillars nearby towards them. Usually, lamellipodia at the leading edge is relatively narrow compared to flat substrate due to the lateral compliance of underlying hairy environment. Furthermore, cells pull nanopillars not only with leading and trailing edge, but also with lateral side of cell body. The underlying mechanism sensing the local environment will be described in the later section. Apart from the common features, the pattern of pulling is different depending on the slanted angle. The most important feature is the pulling of nanopillars at the leading edge. As shown in Fig. 4-8B, cells on 30˚ nanopillars does not pull the nanopillars with their leading edge (n>20). However, in the other cases, cells predominantly pull the nanopillars at the leading edge towards them. This implies that the pulling at the leading edge might not be an important factor in recognizing local anisotropy at 30˚ pillar case.

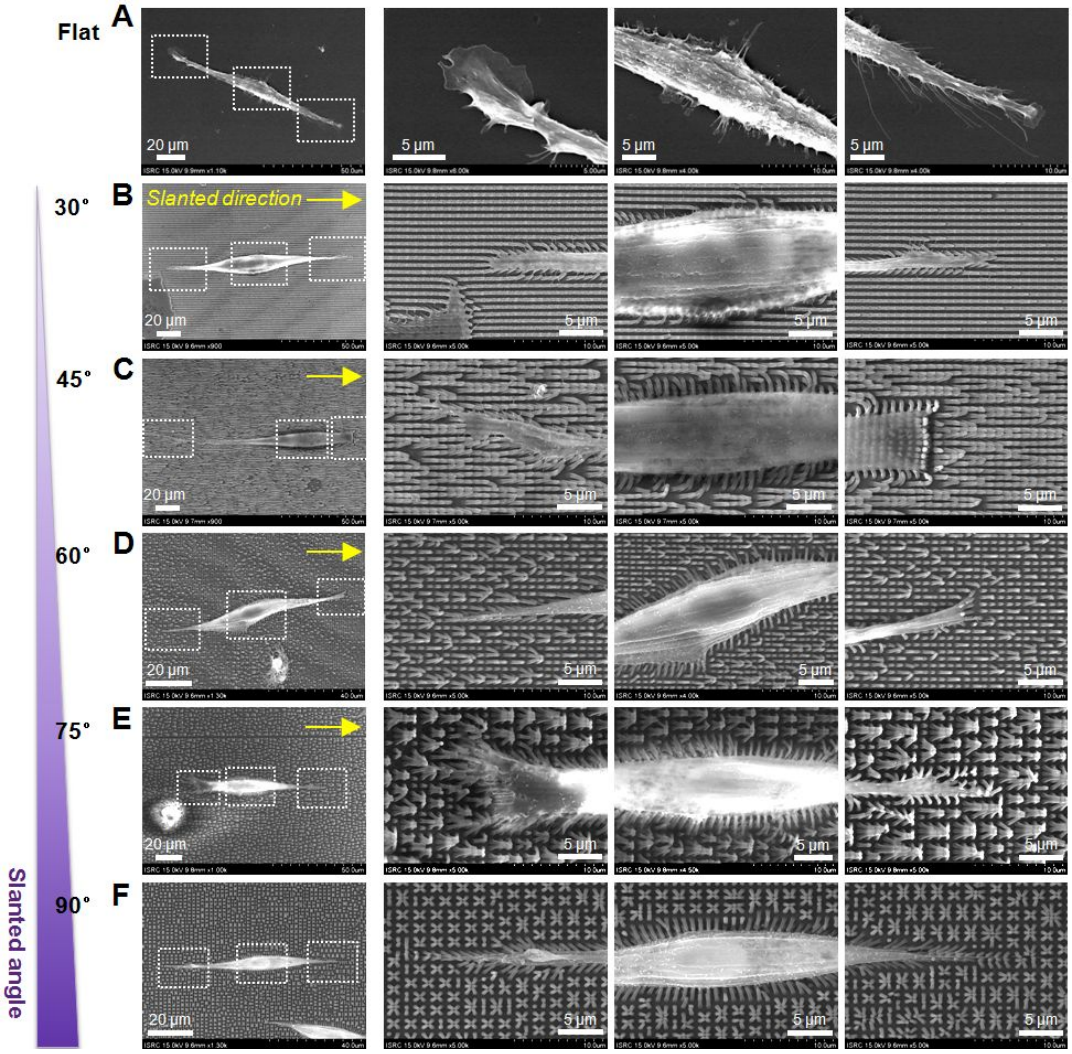

Figure 4-8. Representative SEM images of cells cultured on the slanted nanopillars. (A) Flat, (B) 30˚, (C) 45˚, (D) 60˚, (E) 75˚ and (F) 90˚. The first column shows overall morphologies of cells, and second, third and forth columns show magnified views of white dotted boxes in first column.

4-3-2-3. Finite element method simulation

To verify whether the slanted angle can induce mechanical anisotropy, we conducted finite element method (FEM) simulation using ABAQUS. For the analysis, diameter of 400 nm, length of 2000 nm, elastic modulus of 19.8 MPa, poisson ratio of 0.4 were used. When simulated spring constant with respect to the displacement of pillar top, slanted nanopillars demonstrated different spring constant, more stiffness when pulled towards slanted orientation (Fig. 4-9A). Furthermore, the forward-backward difference is increased as the slanted angle increases. Therefore, the slanted nanopillars could induce mechanical anisotropy depending on the pulling orientation. One notable thing is that even vertical nanopillars (90˚), the spring constant increase as the displacement of pillar top increases.

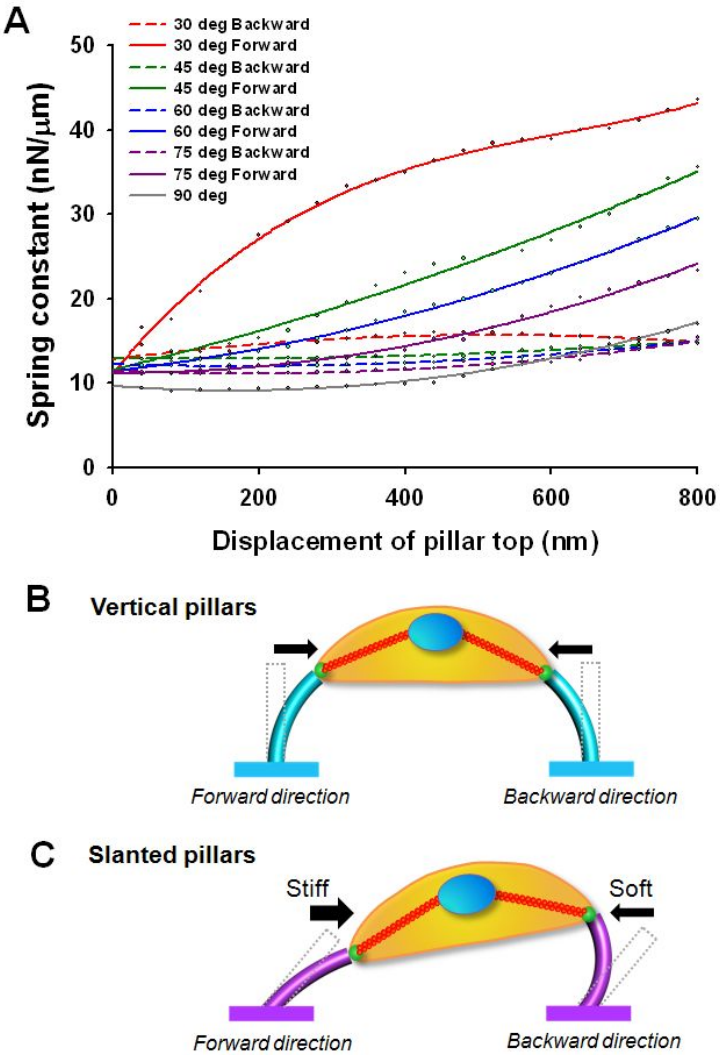

Figure 4-9. Finite Element Method (FEM) simulation of spring constant in vertical and slanted nanopillars using ABAQUS. (A) Simulated spring constant showed different stiffness when pulled forward and backward orientation of slanted angle. (B and C) Schematic illustration of mechanical sensing on vertical (B) and slanted (C) nanopillars.

4-3-3-4. Underlying mechanism of local mechanosensing on slanted nanopillars

We hypothesized that the regulating mechanism might be different since the cellular alignment showed two effects, array and angle effects. In terms of mechanotransduction, it is known that the polarization and migration of cells were mediated majorly by three representative signaling pathways; Rho, Rac and Cdc 42. When cells were treated with Y27632 (a Rho signaling pathway blocker, concentration of 10 μM) at 0h, cells showed no significant change in cell alignment, even in the presence of morphological change at the end of long axis (leading or trailing edge). Furthermore, treatment of Y27632 at 24h after seeding also did not affect to the cell alignment.

When cells were treated with NSC23766 (a Rac signaling inhibitor, concentration of 100 μM) at 0h, cells showed no spreading in the 90˚ nanopillars. Interestingly, the ratio of cells spread increases as the slanted angle increases (from 90˚ to 30˚), indicating that the Rac signaling inhibition is effective majorly in the high 'array effect' cases. On the other hand, when NSC23766 was treated at 24h (concentration of 100 μM), readily aligned cells showed no significant change of alignment, implying that the Rac signaling inhibition is effective in the early stage of adhesion.

To verify whether the slanted angle truly mediates cell signaling, genes responsible for the adhesion and polarity were quantified using qRT-PCR (Fig. 4-

11). Interestingly, Here, focal adhesion kinase (FAK) and Integrin β_1 were chosen as representative genes related to cellular adhesion, while the Wnt family and Rac as genes related to polarity. Interestingly, most of the genes showed biphasic trend showing maximum or minimum at 60˚ slanted nanopillars, while FAK showing minimum at 60˚ slanted nanopillars. This result implies that there might be a transition of underlying mechanism at 60˚.

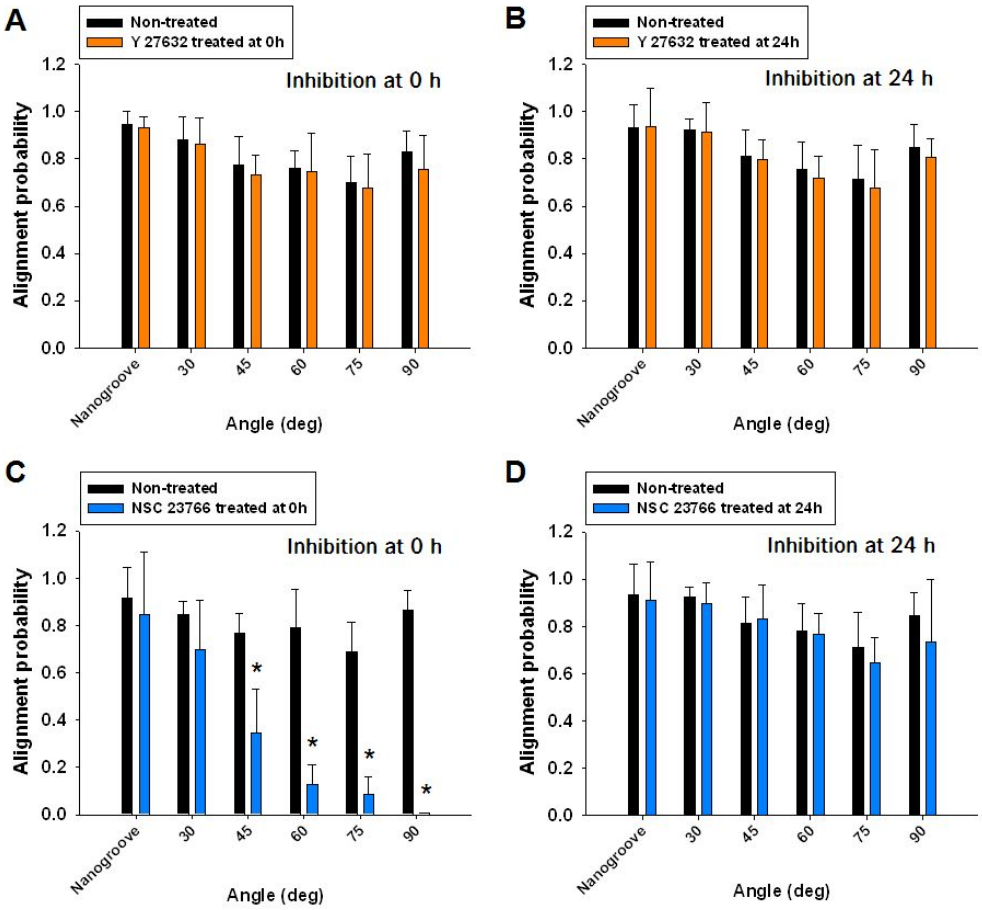

Figure 4-10. Treatment of Y 27632 (a ROCK inhibitor) and NSC 23766 (a Rac inhibitor) at time point 0h and 24h after seeding. Alignment was quantified 24h after the treatment. (A) Y 27632 treated at 0h, (B) Y 27632 treated at 24h, (C) NSC 23766 treated at 0h, and (D) NSC 23766 treated at 24h.

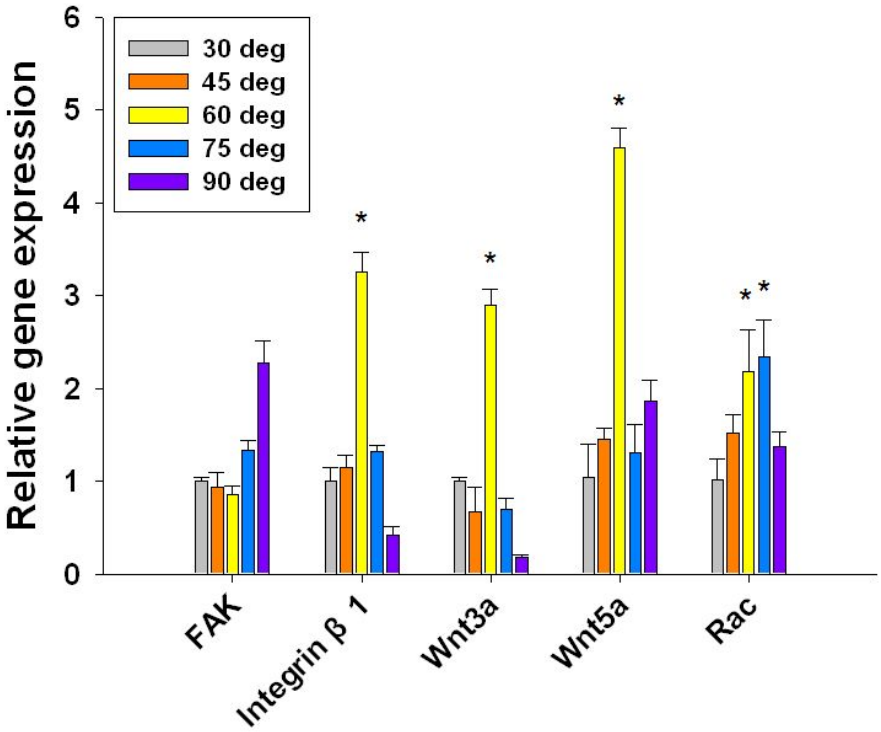

Figure 4-11. Relative gene expression related to adhesion and polarity (*p<0.05).

4-3-3-5. Apparent cellular geometries in responds to slanted angle of nanopillars

The apparent cellular morphologies were also affected by the slanted angle of nanopillars. As shown in Fig. 4-12, the projected area was maximized in 45˚ and 60˚, while the perimeter, major axis, and aspect ratio were maximized at 30˚ case. This long and slender morphology observed in 30˚ was originated from the highly elongated leading and trailing edge of cells. Interestingly, trend of the morphological index in the case of 90˚ showed exception from the trend, probably due to the absence of angle effect.

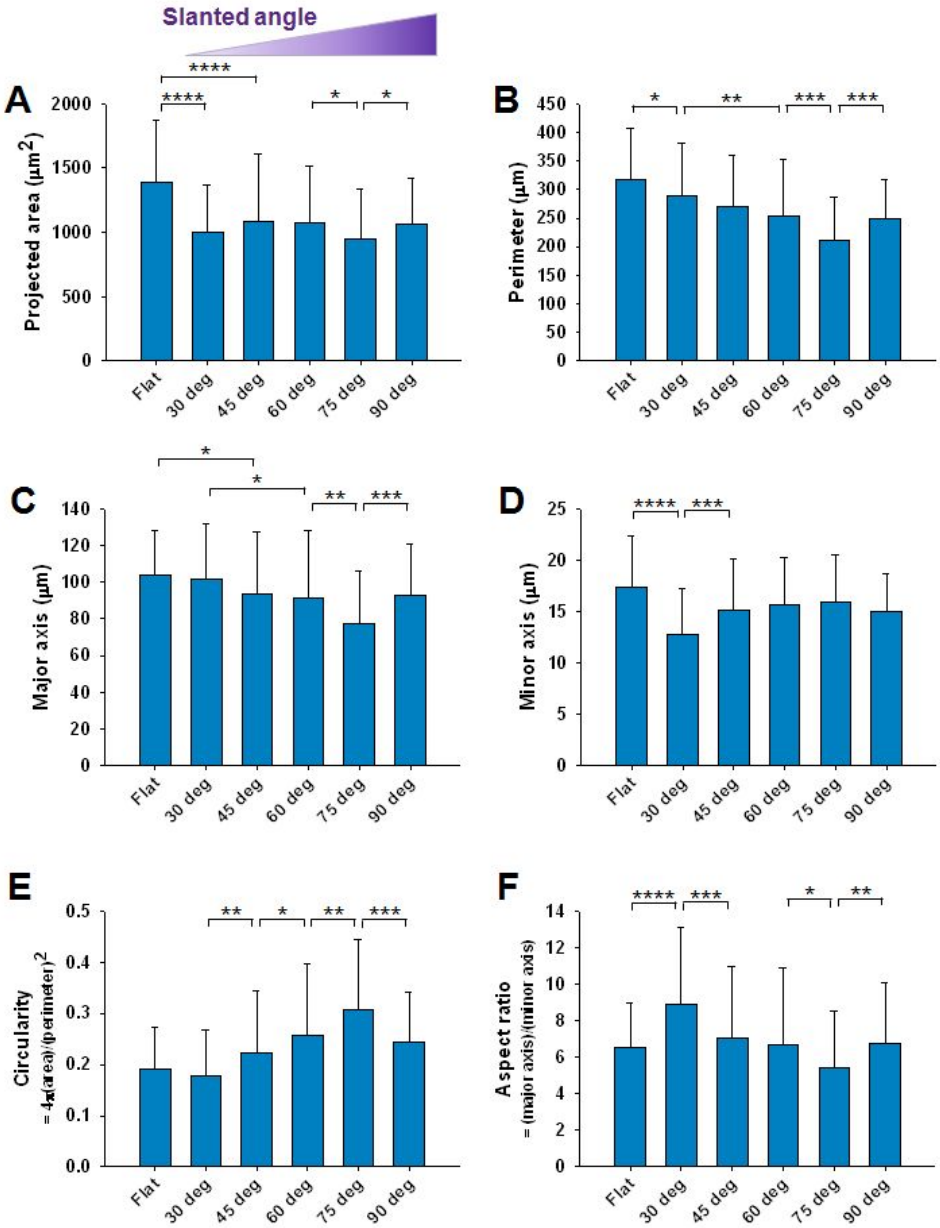

Figure 4-12. Apparent cellular morphologies with respect to the slanted angle. (A) projected area, (B) perimeter, (C) major axis, (D) minor axis, (E) circularity and (F) aspect ratio.

4-4. Discussion

In this study, we demonstrated that the cellular alignment is determined by (i) the arrangement of nanopillars and (ii) the stiffness (spring constant), and (iii) the slanted angle. Although some study reported cellular alignment on hexagonally arrayed micropillars, observed alignment was only toward single orientation, not the hexagonal alignment observed in this study [99]. Although further study is needed, such difference of cellular behaviors observed in between micro and nanoscale pillars is presumably due to the relative difference of feature scale. For example, the micropillars reported earlier have diameter of 2 μm, length of 2 μm, which is corresponds to spring constant of 588.75 (elastic modulus of 1.8 MPa) [91]. Interestingly, such spring constant is similar to that of intermediate nanopillars (diameter: 400 nm, height: 600 nm and elastic modulus: 19.8 MPa). This implies that the relatively smaller feature size might be needed to induce cellular alignment (if is assumed that cell have major axis length of ~90 μm, the ratio of critical dimension in the case of micropillar is ~45 compared to nanopillars ~225 (feature size: micropillars= 2 μm, nanopillars= 400 nm).

In terms of topographical sensing mechanism, pillar structures and grooved structures are different. For example, on the nano- and microgrooved surfaces it is known that cells recognize surface features by sprouting their filopodia and lamellipodia along the orientation of grooves [100], thus it is seems

that the pulling force is not a mediator of cells on grooved substrate. However, as shown in this study, cells on pillar or hairy topography recognize mechanical anisotropy with pulling, and subsequent bending of underlying hairy structures. This difference of sensing mechanism presents interesting points of study, since regulation of cellular behaviors might be possible by relative contribution of two sensing mechanisms.

Furthermore, the change of cell geometries with respect to the stiffness of underlying substrate is different in cases of nanopillars and nanogrooves. For example, in the previous report, cells cultured on nanogrooved surfaces which having diverse mechanical stiffness have demonstrated increased cellular projected area and axial ratio as the stiffness of underlying substrate increases. However, as demonstrated in this study, cells showed reduced projected area and axial ratio as the spring constant increases, which is conflict to the morphological trends on the nanogrooved surfaces. These trends further imply that the underlying mechanism for sensing is regulated by different mechanisms.

As described, the cellular alignment on the relatively vertical nanopillars might be mediated by Rac signaling pathway. According to the previous report, Rac signaling pathway is a mediator of directionally persistent migration since the inhibition of Rac signaling inhibit formation of lamellipodia at the lateral side, thus no signals from the lateral side can be obtained [98]. On the other hand, Rho signaling pathway is a mediator of migration, playing a role in pulling the

substrate at the leading edge. The inhibition study of Rho and Rac signaling pathways indicates that recognition of array is mediated by Rac through the lateral side pulling, but not by the Rho through the pulling at the leading edge.

When cells were cultured on the nanogroove patterns (width of 400 nm, spacing 400 nm), inhibition of Rho and Rac made no difference not only in the initial spreading and alignment but also in the later stage inhibition (data not shown). This implies that underlying mechanism on nanogrooves might be different from that of nanopillars. According to the previous study, cells on the nanogrooves recognize local anisotropy by sprouting their filopodia which is mediated by Cdc42 at the leading edge [100, 101].

4-5. Summary

In this study, we have demonstrated that cellular alignment on the nanopillar arrays follows the arrangement of nanopillar array, and this phenomenon is regulated by the bending of nanopillars. The results on the effect of slanted angle demonstrate that cells on the relatively vertical nanopillars sense local mechanical anisotropy with Rac signaling pathway, but the effect of Rac signaling decreases as the amount of inclination increases. This finding is might be potentially useful since relative contribution of two signaling pathways can be controlled through the sophisticated engineering. It is envisioned that these findings can contribute to cell and tissue engineering synergistically with the advance of nano- and microtecchnologies.

Chapter 5. Summary

The tissues and organs in human body have multiscale structures in a well-organized and tissue-specific form, and such organization endows tissue-specific functions. Inspired from the multiscale structures *in vivo*, we fabricated multiscale geometries in a two dimensional form, and utilized them as bio-mimetic tissue culture platforms. By using the multiscale patterns, we studied the effect of multiscale surface patterns on dermal wound healing, cancer cell migration and mechanically-controlled cell alignment. For tissue- and cell-specific environment, we engineered various mechanical and physical cues such as feature size, spacing, orientation, elastic modulus, and slanted angle of geometries.

In this thesis, we demonstrated engineering of various cellular behaviors such as migration, cell division, alignment by using multiscale surface patterns. To bridge engineering of cell behaviors and multiscale surface patterns, as a mediator of such cellular behaviors, we engineered focal adhesions. Since the focal adhesions are developed and reorganized in response to the geometry of topography and stiffness of substrate, the size and orientation of focal adhesions can be sensitively controlled with the engineering of multiscale surface patterns. Furthermore, since the focal adhesions are positioned in the outermost part of the

cell body and sense the external stimulus in a first priority, they act as primary sensors and regulators of the cell functions. Therefore, the engineering of focal adhesion enables the engineering of various cellular behaviors.

First, we studied the effect of tension line which is a result of aligned collagen fibers in dermis of skin tissue. In this study, with an *in vitro* wound healing model, we investigated the effect of nanotopographical orientation and density of collagen fibers in dermal wound healing. According to the experiments, NIH-3T3 fibroblast cells showed guided migration and cell division in response to the topographical density. Although such migration and division was also affected by the topographical densities, the relative contribution was larger in the case of orientation cue. The analysis of focal adhesion revealed that such directional cell behaviors were originated from the polarized focal adhesions. Furthermore, the organization of produced fibronectin fibers was also affected by the topographical orientation and density of surface patterns. These results indicated that the aligned orientation and density of ECM fibers in dermis may affect to the initial and later stage of wound healing process such as granulation tissue formation and scar formation, respectively. Furthermore, these results showed a coincidence that *in vivo* wound healing speed and scar formation is affected by the tension line. It is envisioned that the bio-mimetic synthetic topography can be used for the wound dressing patch.

Second, the effect of multiscale structures can be important in

pathological progression. As a representative example, the cancer cell migration is usually guided by multiscale structures *in vivo* such as basement membrane, fibrillar interstitial tissues, space tracks, and lymphatic vessels. As well as topographical cues, cell types which can be classified into collectively and individually migrating cells also affect to the cancer cell invasion. When cultured collectively and individual migrating cells in a circular island form with a diameter of 5 mm and let the cells migrate, both collectively and individually migrating cells showed guided spreading. However, the migrating speed following the topographical orientation was faster in the case of individually migrating cells due to the limited cell-cell contact, while the spreading across the topography was faster in the case of collectively migrating cells. According to the immunofluorescence staining of F-actin and vinculin, preferential alignment of F-actin and vinculin towards the topographical orientation was correlated with the guided migration of cancer cells. Furthermore, expression of protein level was also affected by the feature size and orientation. These results collectively indicated that underlying multiscale structures may induce not only apparent behaviors such as migration, but also intracellular changes such as organization of F-actin and vinculin, and expression of protein levels.

Third, unlike the groove-based topographies, nanopillar-based topographies have potential since the mechanical properties can be tuned by the engineering of geometries such as diameter and height. To study the effect of

mechanical anisotropy, we engineered two factors of nanopillar arrays; (i) spring constant and (ii) slanted angle. When cultured NIH-3T3 fibroblast cells on nanopillar arrays with various spring constants, cells showed bi-directional alignment on rectangular arrays and tri-directional alignment on hexagonal arrays, respectively, indicating that the organization of nanopillar arrays may affect to the cell alignment. However, the degree of alignment was decreased as the spring constant increases, and this showed correlation with reduced bending of nanopillars in response to the increasing spring constants. When cells were cultured on slanted nanopillars with various angles such as 30, 45, 60, 75 and 90˚, cells showed bi-directional alignment on the relatively vertical nanopillars (such as 90˚ and 75˚) while showing uni-directional alignment on the relatively slanted nanopillars (such as 30˚ and 45˚). According to the finite element method simulation using ABAQUS, such gradual transition from bi-directional to uni-directional alignment in response to slanted angle was in good correlation with anisotropy of mechanical stiffness.

The results described in this thesis collectively indicate that the physical and mechanical cues can control various cellular behaviors from apparent behaviors to intracellular changes. We believe that multiscale surface patterns can be used various applications such as wound dressing patch, high-throughput screening platform, and platform for basic research.

References

[1] Lo, C. M., H. B. Wang, M. Dembo and Y. L. Wang. Cell movement is guided by the rigidity of the substrate. *Biophys J* 2000;79: 144-152.

[2] Carter, S. B. Principles of cell motility: the direction of cell movement and cancer invasion. *Nature* 1965;208: 1183-1187.

[3] Zhao, M., B. Song, J. Pu, T. Wada, B. Reid, G. P. Tai, et al. Electrical signals control wound healing through phosphatidylinositol-3-OH kinase-gamma and PTEN. *Nature* 2006;442: 457-460.

[4] Petrie, R. J., A. D. Doyle and K. M. Yamada. Random versus directionally persistent cell migration. *Nat Rev Mol Cell Bio* 2009;10: 538-549.

[5] Zigmond, S. H. and J. G. Hirsch. Leukocyte Locomotion and Chemotaxis - New Methods for Evaluation and Demonstration of a Cell-Derived Chemotactic Factor. *J Exp Med* 1973;137: 387-410.

[6] Lashuel, H. A., D. Hartley, B. M. Petre, T. Walz and P. T. Lansbury. Neurodegenerative disease - Amyloid pores from pathogenic mutations. *Nature* 2002;418: 291-291.

[7] Nemir, S. and J. L. West. Synthetic Materials in the Study of Cell Response to Substrate Rigidity. *Ann Biomed Eng* 2010;38: 2-20.

[8] Kim, D. H., P. K. Wong, J. Park, A. Levchenko and Y. Sun. Microengineered Platforms for Cell Mechanobiology. *Annu Rev Biomed Eng* 2009;11: 203-233.

[9] Lee, S. H., D. H. Kang, H. N. Kim and K. Y. Suh. Use of directly molded poly(methyl methacrylate) channels for microfluidic applications. *Lab Chip* 2010;10: 3300-3306.

[10] Janmey, P. A. and C. A. McCulloch. Cell mechanics: Integrating cell responses to mechanical stimuli. *Annu Rev Biomed Eng* 2007;9: 1-34.

[11] Dolatshahi-Pirouz, A., M. Nikkhah, K. Kolind, M. R. Dokmeci and A. Khademhosseini. Micro- and Nanoengineering Approaches to Control Stem Cell-Biomaterial Interactions. *J Funct Biomater* 2011;2: 88-106.

[12] Khademhosseini, A., R. Langer, J. Borenstein and J. P. Vacanti. Microscale technologies for tissue engineering and biology. *P Natl Acad Sci USA* 2006;103: 2480-2487.

[13] Tabesh, H., G. Amoabediny, N. S. Nik, M. Heydari, M. Yosefifard, S. O. R. Siadat, et al. The role of biodegradable engineered scaffolds seeded with Schwann cells for spinal cord regeneration. *Neurochem Int* 2009;54: 73-83.

[14] Kotov, N. A., J. O. Winter, I. P. Clements, E. Jan, B. P. Timko, S. Campidelli, et al. Nanomaterials for Neural Interfaces. *Adv Mater* 2009;21: 3970-4004.

[15] Moore, S. W. and M. P. Sheetz. Biophysics of Substrate Interaction: Influence on Neural Motility, Differentiation, and Repair. *Dev Neurobiol* 2011;71: 1090-1101.

[16] Harrison, R. G. The reaction of embryonic cells to solid structures. *J Exp Zool* 1914;17: 521-544.

[17] Guilak, F., D. M. Cohen, B. T. Estes, J. M. Gimble, W. Liedtke and C. S. Chen. Control of Stem Cell Fate by Physical Interactions with the Extracellular Matrix. *Cell Stem Cell* 2009;5: 17-26.

[18] McNamara, L. E., R. J. McMurray, M. J. Biggs, F. Kantawong, R. O. Oreffo and M. J. Dalby. Nanotopographical control of stem cell differentiation. *J Tissue Eng* 2010;2010: 120623.

[19] Dalby, M. J., N. Gadegaard, R. Tare, A. Andar, M. O. Riehle, P. Herzyk, et al. The control of human mesenchymal cell differentiation using nanoscale symmetry and disorder. *Nat Mater* 2007;6: 997-1003.

[20] Kim, D. H., E. A. Lipke, P. Kim, R. Cheong, S. Thompson, M. Delannoy, et al. Nanoscale cues regulate the structure and function of macroscopic cardiac tissue constructs. *P Natl Acad Sci USA* 2010;107: 565-570.

[21] Yang, Y. and K. W. Leong. Nanoscale surfacing for regenerative medicine. *Wires Nanomed Nanobi* 2010;2: 478-495.

[22] Ehrlich, H. P. and T. M. Krummel. Regulation of wound healing from a connective tissue perspective. *Wound Repair Regen* 1996;4: 203-210.

[23] Teixeira, A. I., G. A. Abrams, P. J. Bertics, C. J. Murphy and P. F. Nealey. Epithelial contact guidance on well-defined micro- and nanostructured

substrates. *J Cell Sci* 2003;116: 1881-1892.

[24] Shah, M., D. M. Foreman and M. W. J. Ferguson. Neutralization of TGF-beta(1) and TGF-beta(2) or exogenous addition of TGF-beta(3) to cutaneous rat wounds reduces scarring. *J Cell Sci* 1995;108: 985-1002.

[25] Whitby, D. J. and M. W. J. Ferguson. Immunohistochemical localization of growth-factors in fetal wound-healing. *Dev Biol* 1991;147: 207-215.

[26] Noh, H. K., S. W. Lee, J. M. Kim, J. E. Oh, K. H. Kim, C. P. Chung, et al. Electrospinning of chitin nanofibers: Degradation behavior and cellular response to normal human keratinocytes and fibroblasts. *Biomaterials* 2006;27: 3934-3944.

[27] Rho, K. S., L. Jeong, G. Lee, B. M. Seo, Y. J. Park, S. D. Hong, et al. Electrospinning of collagen nanofibers: Effects on the behavior of normal human keratinocytes and early-stage wound healing. *Biomaterials* 2006;27: 1452-1461.

[28] Rnjak-Kovacina, J., S. G. Wise, Z. Li, P. K. M. Maitz, C. J. Young, Y. W. Wang, et al. Tailoring the porosity and pore size of electrospun synthetic human elastin scaffolds for dermal tissue engineering. *Biomaterials* 2011;32: 6729-6736.

[29] Kurpinski, K. T., J. T. Stephenson, R. R. R. Janairo, H. M. Lee and S. Li. The effect of fiber alignment and heparin coating on cell infiltration into nanofibrous PLLA scaffolds. *Biomaterials* 2010;31: 3536-3542.

[30] Pierard, G. E. and C. M. Lapiere. Microanatomy of the dermis in relation to relaxed skin tension lines and Langer's lines. *Am J Dermatopathol* 1987;9: 219-224.

[31] Kim, H. N., A. Jiao, N. S. Hwang, M. S. Kim, D. H. Kang, D. H. Kim, et al. Nanotopography-guided tissue engineering and regenerative medicine. *Adv Drug Deliver Rev* 2012;65: 536-558.

[32] Lee-Parritz, A. Surgical techniques for Cesarean delivery: What are the best practices? *Clin Obstet Gynecol* 2004;47: 286-298.

[33] Atkinson, J. A. M., K. T. McKenna, A. G. Barnett, D. J. McGrath and M. Rudd. A randomized, controlled trial to determine the efficacy of paper tape

in preventing hypertrophic scar formation in surgical incisions that traverse Langer's skin tension lines. *Plast Reconstr Surg* 2005;116: 1648-1656.

[34] Suh, K. Y., M. C. Park and P. Kim. Capillary force lithography: A versatile tool for structured biomaterials interface towards cell and tissue engineering. *Adv Funct Mater* 2009;19: 2699-2712.

[35] Choi, S. J., H. N. Kim, W. G. Bae and K. Y. Suh. Modulus- and surface energy-tunable ultraviolet-curable polyurethane acrylate: properties and applications. *J Mater Chem* 2011;21: 14325-14335.

[36] Canty, E. G. and K. E. Kadler. Procollagen trafficking, processing and fibrillogenesis. *J Cell Sci* 2005;118: 1341-1353.

[37] Cheng, T. L., Y. T. Wu, H. Y. Lin, F. C. Hsu, S. K. Liu, B. I. Chang, et al. Functions of rhomboid family protease RHBDL2 and thrombomodulin in wound healing. *J Invest Dermatol* 2011;131: 2486-2494.

[38] Gao, F., C. X. Yang, W. Mo, Y. W. Liu and Y. Q. He. Hyaluronan oligosaccharides are potential stimulators to angiogenesis via RHAMM mediated signal pathway in wound healing. *Clin Invest Med* 2008;31: E106-E116.

[39] Ranzato, E., M. Patrone, M. Pedrazzi and B. Burlando. Hmgb1 promotes wound healing of 3T3 mouse fibroblasts via RAGE-dependent ERK1/2 activation. *Cell Biochem Biophys* 2010;57: 9-17.

[40] Nikolic, D. L., A. N. Boettiger, D. Bar-Sagi, J. D. Carbeck and S. Y. Shvartsman. Role of boundary conditions in an experimental model of epithelial wound healing. *Am J Physiol-Cell Ph* 2006;291: C68-C75.

[41] Fong, E., S. Tzlil and D. A. Tirrell. Boundary crossing in epithelial wound healing. *P Natl Acad Sci USA* 2010;107: 19302-19307.

[42] Song, K. H., K. W. Kwon, S. Song, K. Y. Suh and J. Doh. Dynamics of T cells on endothelial layers aligned by nanostructured surfaces. *Biomaterials* 2012;33: 2007-2015.

[43] Owen, G. R., D. O. Meredith, I. ap Gwynn and R. G. Richards. Focal adhesion quantification - a new assay of material biocompatibility? Review. *Eur Cell Mater* 2005;9: 85-96.

[44] Kim, D. H., K. Han, K. Gupta, K. W. Kwon, K. Y. Suh and A. Levchenko. Mechanosensitivity of fibroblast cell shape and movement to anisotropic substratum topography gradients. *Biomaterials* 2009;30: 5433-5444.

[45] Ridley, A. J. Rho GTPases and cell migration. *J Cell Sci* 2001;114: 2713-2722.

[46] Sammak, P. J., L. E. Hinman, P. O. T. Tran, M. D. Sjaastad and T. E. Machen. How do injured cells communicate with the surviving cell monolayer? *J Cell Sci* 1997;110: 465-475.

[47] Hui, E. E. and S. N. Bhatia. Micromechanical control of cell-cell interactions. *P Natl Acad Sci USA* 2007;104: 5722-5726.

[48] Liliensiek, S. J., S. Campbell, P. F. Nealey and C. J. Murphy. The scale of substratum topographic features modulates proliferation of corneal epithelial cells and corneal fibroblasts. *J Biomed Mater Res A* 2006;79A: 185-192.

[49] Thery, M., A. Jimenez-Dalmaroni, V. Racine, M. Bornens and F. Julicher. Experimental and theoretical study of mitotic spindle orientation. *Nature* 2007;447: 493-496.

[50] Thery, M. and M. Bornens. Cell shape and cell division. *Curr Opin Cell Biol* 2006;18: 648-657.

[51] Yim, E. K. F., R. M. Reano, S. W. Pang, A. F. Yee, C. S. Chen and K. W. Leong. Nanopattern-induced changes in morphology and motility of smooth muscle cells. *Biomaterials* 2005;26: 5405-5413.

[52] Fisher, G. J., J. Varani and J. J. Voorhees. Looking older - Fibroblast collapse and therapeutic implications. *Arch Dermatol* 2008;144: 666-672.

[53] Fawzi-Grancher, S., N. De Isla, G. Faure, J. F. Stoltz and S. Muller. Optimisation of biochemical condition and substrates in vitro for tissue engineering of ligament. *Ann Biomed Eng* 2006;34: 1767-1777.

[54] Dale, P. D., J. A. Sherratt and P. K. Maini. Role of fibroblast migration in collagen fiber formation during fetal and adult dermal wound healing. *B Math Biol* 1997;59: 1077-1100.

[55] Cumming, B. D., D. L. S. McElwain and Z. Upton. A mathematical model of wound healing and subsequent scarring. *J R Soc Interface* 2010;7: 19-34.

[56] Charest, J. L., M. T. Eliason, A. J. Garcia and W. P. King. Combined microscale mechanical topography and chemical patterns on polymer cell culture substrates. *Biomaterials* 2006;27: 2487-2494.

[57] Patel, S., K. Kurpinski, R. Quigley, H. F. Gao, B. S. Hsiao, M. M. Poo, et al. Bioactive nanofibers: Synergistic effects of nanotopography and chemical signaling on cell guidance. *Nano Lett* 2007;7: 2122-2128.

[58] Kumar, G., C. C. Ho and C. C. Co. Guiding cell migration using one-way micropattern arrays. *Adv Mater* 2007;19: 1084-1090.

[59] Jeon, H., H. Hidai, D. J. Hwang, K. E. Healy and C. P. Grigoropoulos. The effect of micronscale anisotropic cross patterns on fibroblast migration. *Biomaterials* 2010;31: 4286-4295.

[60] Hamilton, D. W., C. J. Oates, A. Hasanzadeh and S. Mittler. Migration of periodontal ligament fibroblasts on nanometric topographical patterns: Influence of filopodia and focal adhesions on contact guidance. *Plos One* 2010;5: e15129.

[61] Verhaegen, P. D. H. M., J. Van Marle, A. Kuehne, H. J. Schouten, E. A. Gaffney, P. K. Maini, et al. Collagen bundle morphometry in skin and scar tissue: a novel distance mapping method provides superior measurements compared to Fourier analysis. *J Microsc-Oxford* 2012;245: 82-89.

[62] McDougall, S., J. Dallon, J. Sherratt and P. Maini. Fibroblast migration and collagen deposition during dermal wound healing: mathematical modelling and clinical implications. *Philos T R Soc A* 2006;364: 1385-1405.

[63] Dallon, J. C., J. A. Sherratt and P. K. Maini. Mathematical modelling of extracellular matrix dynamics using discrete cells: Fiber orientation and tissue regeneration. *J Theor Biol* 1999;199: 449-471.

[64] Yamaguchi, H., J. Wyckoff and J. Condeelis. Cell migration in tumors. *Curr Opin Cell Biol* 2005;17: 559-564.

[65] Sahai, E. Mechanisms of cancer cell invasion. *Curr Opin Genet Dev* 2005;15: 87-96.

[66] Radisky, E. S. and D. C. Radisky. Matrix Metalloproteinase-Induced Epithelial-Mesenchymal Transition in Breast Cancer. *J Mammary Gland Biol*

2010;15: 201-212.
[67] Friedl, P. and K. Wolf. Tumour-cell invasion and migration: Diversity and escape mechanisms. *Nat Rev Cancer* 2003;3: 362-374.
[68] Friedl, P. and S. Alexander. Cancer Invasion and the Microenvironment: Plasticity and Reciprocity. *Cell* 2011;147: 992-1009.
[69] Friedl, P. and D. Gilmour. Collective cell migration in morphogenesis, regeneration and cancer. *Nat Rev Mol Cell Bio* 2009;10: 445-457.
[70] Hood, J. D. and D. A. Cheresh. Role of integrins in cell invasion and migration. *Nat Rev Cancer* 2002;2: 91-100.
[71] Wolf, K., I. Mazo, H. Leung, K. Engelke, U. H. von Andrian, E. I. Deryugina, et al. Compensation mechanism in tumor cell migration: mesenchymal-amoeboid transition after blocking of pericellular proteolysis. *J Cell Biol* 2003;160: 267-277.
[72] Gaggioli, C., S. Hooper, C. Hidalgo-Carcedo, R. Grosse, J. F. Marshall, K. Harrington, et al. Fibroblast-led collective invasion of carcinoma cells with differing roles for RhoGTPases in leading and following cells. *Nat Cell Biol* 2007;9: 1392-1400.
[73] Liotta, L. A. and W. G. Stetler-Stevenson. Tumor invasion and metastasis: an imbalance of positive and negative regulation. *Cancer Res* 1991;51: 5054s-5059s.
[74] Contreras, R. G., L. Shoshani, C. Flores-Maldonado, A. Lazaro, A. O. Monroy, M. L. Roldan, et al. E-cadherin and tight junctions between epithelial cells of different animal species. *Pflug Arch Eur J Phy* 2002;444: 467-475.
[75] Hwang, S., N. P. Zimmerman, K. A. Agle, J. R. Turner, S. N. Kumar and M. B. Dwinell. E-cadherin Is Critical for Collective Sheet Migration and Is Regulated by the Chemokine CXCL12 Protein During Restitution. *J Biol Chem* 2012;287: 22227-22240.
[76] Worthylake, R. A. and K. Burridge. RhoA and ROCK promote migration by limiting membrane protrusions. *J Biol Chem* 2003;278: 13578-13584.
[77] Zohrabian, V. M., B. Forzani, Z. Chau, R. Murali and M. Jhanwar-Uniyal.

Rho/ROCK and MAPK signaling pathways are involved in glioblastoma cell migration and proliferation. *Anticancer Res* 2009;29: 119-123.

[78] Goldmann, W. H., V. Auernheimer, I. Thievessen and B. Fabry. Vinculin, cell mechanics and tumour cell invasion. *Cell Biol Int* 2013;37: 397-405.

[79] Subauste, M. C., O. Pertz, E. D. Adamson, C. E. Turner, S. Junger and K. M. Hahn. Vinculin modulation of paxillin-FAK interactions regulates ERK to control survival and motility. *J Cell Biol* 2004;165: 371-381.

[80] Kalluri, R. and R. A. Weinberg. The basics of epithelial-mesenchymal transition. *J Clin Invest* 2009;119: 1420-1428.

[81] Radisky, D. C. Epithelial-mesenchymal transition. *J Cell Sci* 2005;118: 4325-4326.

[82] Pierrat, P., G. Creusat, G. Laverny, F. Pons, G. Zuber and L. Lebeau. A Cationic Phospholipid-Detergent Conjugate as a New Efficient Carrier for siRNA Delivery. *Chem-Eur J* 2012;18: 3835-3839.

[83] Ilina, O., G. J. Bakker, A. Vasaturo, R. M. Hofmann and P. Friedl. Two-photon laser-generated microtracks in 3D collagen lattices: principles of MMP-dependent and -independent collective cancer cell invasion. *Phys Biol* 2011;8.

[84] Kim, H. N., A. Jiao, N. S. Hwang, M. S. Kim, D. H. Kang, D. H. Kim, et al. Nanotopography-guided tissue engineering and regenerative medicine. *Adv Drug Deliv Rev* 2013;65: 536-558.

[85] Kim, H. N., D. H. Kang, M. S. Kim, A. Jiao, D. H. Kim and K. Y. Suh. Patterning Methods for Polymers in Cell and Tissue Engineering. *Ann Biomed Eng* 2012;40: 1339-1355.

[86] Kim, J., H. N. Kim, K. T. Lim, Y. Kim, S. Pandey, P. Garg, et al. Synergistic effects of nanotopography and co-culture with endothelial cells on osteogenesis of mesenchymal stem cells. *Biomaterials* 2013;34: 7257-7268.

[87] Prager-Khoutorsky, M., A. Lichtenstein, R. Krishnan, K. Rajendran, A. Mayo, Z. Kam, et al. Fibroblast polarization is a matrix-rigidity-dependent process controlled by focal adhesion mechanosensing. *Nat Cell Biol* 2011;13: 1457-1465.

[88] Kim, D. H., C. H. Seo, K. Han, K. W. Kwon, A. Levchenko and K. Y. Suh. Guided Cell Migration on Microtextured Substrates with Variable Local Density and Anisotropy. *Adv Funct Mater* 2009;19: 1579-1586.

[89] Jiang, X. Y., D. A. Bruzewicz, A. P. Wong, M. Piel and G. M. Whitesides. Directing cell migration with asymmetric micropatterns. *P Natl Acad Sci USA* 2005;102: 975-978.

[90] Bettinger, C. J., Z. T. Zhang, S. Gerecht, J. T. Borenstein and R. Langer. Enhancement of in vitro capillary tube formation by substrate nanotopography. *Adv Mater* 2008;20: 99-103.

[91] Fu, J. P., Y. K. Wang, M. T. Yang, R. A. Desai, X. A. Yu, Z. J. Liu, et al. Mechanical regulation of cell function with geometrically modulated elastomeric substrates. *Nat Methods* 2010;7: 733-736.

[92] Vedula, S. R. K., M. C. Leong, T. L. Lai, P. Hersen, A. J. Kabla, C. T. Lim, et al. Emerging modes of collective cell migration induced by geometrical constraints. *P Natl Acad Sci USA* 2012;109: 12974-12979.

[93] Dupont, S., L. Morsut, M. Aragona, E. Enzo, S. Giulitti, M. Cordenonsi, et al. Role of YAP/TAZ in mechanotransduction. *Nature* 2011;474: 179-183.

[94] Jeong, H. E., J. K. Lee, H. N. Kim, S. H. Moon and K. Y. Suh. A nontransferring dry adhesive with hierarchical polymer nanohairs. *P Natl Acad Sci USA* 2009;106: 5639-5644.

[95] Jeong, H. E., J. K. Lee, M. K. Kwak, S. H. Moon and K. Y. Suh. Effect of leaning angle of gecko-inspired slanted polymer nanohairs on dry adhesion. *Appl Phys Lett* 2010;96.

[96] La, W. G., J. Y. Shin, S. H. Bhang, M. Jin, H. H. Yoon, S. S. Noh, et al. Culture on a 3,4-Dihydroxy-L-Phenylalanine-Coated Surface Promotes the Osteogenic Differentiation of Human Mesenchymal Stem Cells. *Tissue Eng Pt A* 2013;19: 1255-1263.

[97] Schoen, I., W. Hu, E. Klotzsch and V. Vogel. Probing Cellular Traction Forces by Micropillar Arrays: Contribution of Substrate Warping to Pillar Deflection. *Nano Lett* 2010;10: 1823-1830.

[98] Pankov, R., Y. Endo, S. Even-Ram, M. Araki, K. Clark, E. Cukierman, et al.

A Rac switch regulates random versus directionally persistent cell migration. *J Cell Biol* 2005;170: 793-802.

[99] Ghibaudo, M., A. Saez, L. Trichet, A. Xayaphoummine, J. Browaeys, P. Silberzan, et al. Traction forces and rigidity sensing regulate cell functions. *Soft Matter* 2008;4: 1836-1843.

[100] Jang, K. J., M. S. Kim, D. Feltrin, N. L. Jeon, K. Y. Suh and O. Pertz. Two Distinct Filopodia Populations at the Growth Cone Allow to Sense Nanotopographical Extracellular Matrix Cues to Guide Neurite Outgrowth. *Plos One* 2010;5.

[101] Krugmann, S., I. Jordens, K. Gevaert, M. Driessens, J. Vandekerckhove and A. Hall. Cdc42 induces filopodia by promoting the formation of an IRSp53 : Mena complex. *Curr Biol* 2001;11: 1645-1655.

국문초록

본 학위 논문에서는 인체내부에서 발견되는 멀티스케일 구조를 모사하여 표면 패턴을 제작하고, 조직 특이성을 가지는 멀티스케일 패턴 위에서 세포의 거동을 조절하는 것을 목적으로 하였다. 이를 위하여 멀티스케일 구조의 간격, 방향, 크기, 스프링 상수 및 기울어진 각도 등의 물리적/기계적 요소를 제어하였다. 멀티스케일 패턴의 제작을 위하여 모세관력 리소그래피 (capillary force lithography, CFL) 기술을 이용하여 섬유와 섬모를 기본형태로 한 다양한 형태의 구조들을 제작하였다. 제작된 표면 구조위에 파이브로넥틴, 1 종 콜라겐 등의 세포외기질 코팅을 함으로써 인체 내부에 존재하는 섬유상의 세포외기질을 모사한 구조를 제작할 수 있다.

먼저, 멀티스케일 구조의 간격과 방향이 상처재생에 미치는 영향을 알아보았다. 피부에는 비등방성의 기계적 특성을 보이는 피부결이 존재하는데 이러한 피부결은 한쪽 방향으로 정렬된 콜라겐 섬유가 그 원인임이 알려졌다. 상처의 재생 속도와 흉터 형성이 피부결의 방향에 영향을 받는다는 점에 착안하여 공학적으로 제작된 나노 패턴의 방향과 간격이 피부의 상처재생에 어떤 영향을 미치는지 실험하였다. 다양한 간격 (너비: 550 nm, 간격: 550, 1100, 2750 nm) 를 가지는 나노그루브 (nano groove) 패턴 위에 NIH-3T3 섬유아세포 (fibroblast) 를 배양하였을

때, 세포들은 그루브 패턴의 방향에 따라 40 배 가까운 이동속도 차이를 보였으며, 패턴의 간격에 따라서는 중간 간격 (1100 nm, 1:2 간격비)에서 최고의 이동속도를 보였다. 또한 나노패턴의 간격은 세포의 증식 속도에는 영향을 주지 않았지만, 세포가 나노그루브 방향으로 분열하도록 유도함으로써 방향성 있는 상처재생에 도움을 주었다. 그 외에도 세포가 패턴을 따라 정렬되도록 함으로써 분비한 세포외기질 섬유가 패턴 방향으로 정렬되도록 유도하였다. 이와 같은 결과는 나노구조가 세포의 이동, 분열, 그리고 재생 후 세포외기질 정렬에도 영향을 줄 수 있음을 암시하였다.

다음으로는 멀티스케일 구조의 크기와 방향이 집단적 및 개별적 암세포 이동에 미치는 영향에 대해 알아보았다. 기존의 연구에 따르면 암세포는 나노섬유상의 기저막, 섬유아세포가 생성한 마이크로트랙 및 림프관 등의 도관 등 물리적 구조를 타고 침윤한다고 알려져 있다. 하지만 암세포는 크기 집단적으로 이동하는 종류와 개별적으로 이동하는 종류가 있기 때문에 이러한 세포의 종류가 멀티스케일 구조에서의 이동에 어떠한 영향을 미치는지 알아보고자 하였다. 우선 집단적 및 개별적 이동하는 암세포들은 모두 표면 구조의 방향으로 더 빠르게 이동하였으나, 멀티스케일 구조 위에서 집단적 이동 세포는 개별적 이동 세포보다 더 느리게 이동하였고, 구조의 크기와 방향에 덜 민감하게 반응하였다. 더불어 멀티스케일 패턴의 방향은 세포의 이동에

관여하는 f-actin 과 vinculin 의 정렬도에 영향을 주었으며, E-cadherin, ROCK2 및 vinculin 단백질 양에도 영향을 주었다. 하지만 패턴의 크기와 방향에 따른 단백질 양의 변화 패턴은 집단적 및 개별적 세포 이동에 따라 다른 것으로 보아 세포 종류에 따라 암세포 침윤이 특성이 달라짐을 알 수 있었다.

마지막으로 멀티스케일 구조의 스프링 상수와 기울어진 각도가 세포의 정렬에 미치는 영향을 알아보았다. 지름 400 nm, 간격 400 nm 인 나노 섬모들의 높이 (2000 nm 와 600 nm)와 재료 (320 MPa 와 19.8MPa)를 조절하여 스프링 상수를 조절하였다. 세포는 나노섬모들의 배열 형태에 따라 두 방향 (사각형 배열) 혹은 세 방향 (육각형 배열)으로 정렬 되었으나 그 정렬 정도는 섬모의 스프링 상수가 증가함에 따라 감소하였다. 주사전자현미경으로 관찰하였을 때 세포의 정렬되는 정도는 세포가 필라를 적게 당길수록 감소하는 것으로 보아 섬모 구조에서는 섬모의 휘어짐이 정렬에 중요한 역할을 함을 알 수 있다. 또한 세포를 기울어진 나노섬모 위에 배양하였을 때 세포는 상대적으로 수직인 섬모에서는 x 와 y 축의 두 방향으로 배열되지만, 점점 섬모가 기울어짐에 따라 기울어진 방향으로 정렬되는 한방향 정렬 특성을 보였다. 이러한 정렬은 '배열 효과' 와 '각도 효과' 로 구분할 수 있으며, 수직인 섬모에서는 배열 효과가 우세한 반면 기울어진 섬모에서는 각도 효과가 우세하였다. ABAQUS 를 이용한 유한요소해석에 따르면

기울어진 섬모를 정방향과 역방향으로 당겼을 때 발생하는 스프링 상수의 차이가 비등방성 기계적 특성을 유도하여 세포를 정렬하게 유도함을 알 수 있었다.

위와 같은 결과들에서 볼 수 있듯이 세포는 표면구조에 민감하게 반응하며, 이러한 물리적/기계적 요소를 사용하여 부착, 이동, 분열 및 정렬 등의 다양한 세포의 거동을 제어할 수 있었다. 멀티스케일 표면 패턴은 세포의 기능을 정밀하게 조절할 수 있다는 장점을 이용하여 상처재생 패치, 약물 스크리닝 플랫폼 및 기초연구용 플랫폼 등 다양한 분야에 적용될 수 있을 것이다.

주요어: 멀티스케일 표면 구조, 세포외기질, 자연모사, 상처 재생, 암 침윤, 비등방성, 세포 이동

학번: 2010-30186